Preparation and characterization of Tellurium based oxides for material studies

THESIS

Submitted to

GOA UNIVERSITY

For the award of the degree of

DOCTOR OF PHILOSOPHY

In

CHEMISTRY

By

Ms. SUDARSHANA DHANARATH MARDOLKAR

Under the guidance of

PROF. A. V. SALKER

Professor in Chemistry, Department of Chemistry,

Goa University

Taleigao Plateau, Goa

DECEMBER 2018

DECLARATION

I hereby declare that the work embodied in the thesis entitled "**Preparation and Characterization of Tellurium based oxides for Material studies.**" is the result of investigations carried out by me under the guidance of **Prof. A. V. Salker** at Department of Chemistry, Goa University and that it has not previously formed the basis for the award of any degree or diploma or other similar titles.

In keeping with the general practice of reporting scientific observations, due acknowledgement has been made wherever the work described is based on the findings of other investigators.

Ms. Sudarshana Dhanarath Mardolkar
Research Student
Department of Chemistry
Goa University
Goa-403206, India.

December 2018

CERTIFICATE

This is to certify that the thesis entitled, "**PREPARATION AND CHARACTERIZATION OF TELLURIUM BASED OXIDES FOR MATERIAL STUDIES**" submitted by Ms. **Sudarshana Dhanarath Mardolkar**, is a record of research work carried out by the candidate during the period of study under my supervision and that it has not previously formed the basis for the award of any degree or diploma or other similar titles.

Prof. A. V. Salker
Research Guide
Department of Chemistry
Goa University
Goa -403206, India

December 2018

CONTENTS

CHAPTER 1

1. INTRODUCTION 1

CHAPTER 2

2. LITERATURE REVIEW 8

2.1 Oxyanions and oxyacids of tellurium 10

2.2 Uses of tellurium 11

2.3 Al_2TeO_6 13

2.3.1 In-general 13

2.3.2 Synthesis reports 14

2.3.3.1 Solid State technique 14

2.4 Fe_2TeO_6 15

2.4.1 In-general 15

2.4.2 Structure and Properties 16

2.4.3 Magnetic structure of Fe_2TeO_6 17

2.4.4 Synthetic methodology 18

2.4.4.1 Solid state method 18

2.4.4.2 PLD technique 19

2.5 Ni_3TeO_6 19

2.5.1 In-general 19

2.5.2 Synthesis 20

2.5.2.1 Solid State method 20

2.5.2.2 Chemical Transport method 21

2.5.2.3 Flux growth method 22

2.5.2.4 Sol – Gel method 22

2.5.3 Structure and Properties 23

2.6 Cu_3TeO_6 25

2.6.1 In-general Cu_3TeO_6 25

2.6.2 Structural properties 25

2.6.3 Synthesis 26

2.6.3.1 Solid state ball milling method 26

2.6.3.2 Chemical transport method 27

2.7 Solid state properties 27

2.7.1 Electrical properties 27

2.7.2 Magnetic properties 28

2.7.3 Optical properties 29

2.7.4 Catalytic and Antibacterial studies 29

CHAPTER 3

3. EXPERIMENTAL 31

3.1 Co-precipitation Method 32

3.1.1 $Cu_{3-x}M_xTeO_6$ (M = Co, Ni, Zn and Mn) 32

3.1.2 $Cu_3Te_{1-x}M_xO_6$ (M = W, Mo) 33

3.1.3 $Cu_{2.9}M_{0.1}TeO_6$ (M = Fe, Eu and Ag) 34

3.1.4 $Ni_{3-x}M_xTeO_6$ (M = Co, Cu and Zn) 34

3.1.5 $Ni_3Te_{1-x}M_xO_6$ (M = W, Mo) 35

3.1.6 Fe_2TeO_6 and $Fe_{1.9}Eu_{0.1}TeO_6$ 35

3.1.7 Al_2TeO_6 36

3.2 Sol-Gel Method 36

3.2.1 $Cu_{3-x}M_xTeO_6$ (M = Co, Ni, Zn and Mn) 36

3.3 Experimental characterization techniques under study 37

3.3.1 Thermal Analysis (TG-DTA/DSC) 37

3.3.2 Powder X-Ray Diffraction (XRD) 38

3.3.3 Infra-Red Spectroscopy (IR) 39

3.3.4 UV-Visible Diffused Reflectance Spectroscopy (UV-DRS) 40

3.3.4 X-Ray Photoelectron Spectroscopy (XPS) 41

3.3.5 Scanning Electron Microscopy-Energy Dispersive Spectroscopy (SEM-EDS) 42

3.3.6 Transmission Electron Microscopy (TEM) 42

3.3.7 DC (Direct Current) Electrical Resistivity 43

3.3.8 Vibrating Sample Magnetometer (VSM) 44

3.3.9 Thermoelectric Power (TEP) 44

3.3.10 Inductively coupled plasma atomic emission spectroscopy (ICP-AES) 45

3.3.11 Dielectric Study 46

3.3.12 Photoluminescence Study (PL) 47

3.4 Photo-catalytic activity **48**

3.5 Partial propylene oxidation **49**

3.6 Antibacterial Study **49**

CHAPTER 4

4. CHARACTERIZATION AND SPECTROSCOPIC STUDIES **50**

4.1 Thermal Analysis (TG-DTA/DSC) **51**

4.1.2 $Cu_{2.7}Ni_{0.3}TeO_6$ 52

4.1.3 $Cu_{2.9}Zn_{0.1}TeO_6$ 53

4.1.4 Ni_3TeO_6 53

4.1.5 Fe_2TeO_6 and Al_2TeO_6 54

4.1.6 Doped and pristine Cu_3TeO_6 55

4.2 X-ray diffraction technique (XRD) **56**

4.2.1 Pristine and cobalt doped Cu_3TeO_6 56

4.2.2 Pristine and nickel doped Cu_3TeO_6 57

4.2.3 Zinc doped Cu_3TeO_6 and manganese doped Cu_3TeO_6 58

4.2.4 Tungsten doped Cu_3TeO_6 and molybdenum doped Cu_3TeO_6 59

4.2.5 Pristine and doped $Cu_{2.9}M_{0.1}TeO_6$ (M=Ag, Fe, Eu) 59

4.2.6 Pristine and doped Ni_3TeO_6 60

4.2.7 Pristine and doped Fe_2TeO_6 and pristine Al_2TeO_{66} 61

4.2.8 Pristine and doped Cu_3TeO_6 61

4.3 Infrared spectroscopy **62**

4.3.1. Pristine and cobalt doped Cu_3TeO_6 62

4.3.2. Pristine and nickel doped Cu_3TeO_6 63

4.3.3. Zinc and Manganese doped Cu_3TeO_6 64

4.3.4. Pristine and cobalt doped Cu_3TeO_6 64

4.4 UV-Visible Diffused Reflectance Spectroscopy **66**

4.4.1 Pristine Cu_3TeO_6 and cobalt doped Cu_3TeO_6 66

4.4.2 Nickel doped Cu_3TeO_6 68

4.4.3 Zinc doped Cu_3TeO_6 69

4.4.4 Manganese doped Cu_3TeO_6 70

4.4.5 $Cu_{2.8}M_{0.2}TeO_6$ (M = W and Mo) 71

4.4.6 Ni_3TeO_6 72

4.5 ICP-AES **72**

4.6 Scanning Electron Microscopy (SEM) **73**

4.6.1 Pristine Cu_3TeO_6 73

4.6.2 Cobalt-doped Cu_3TeO_6 74

4.6.3 Nickel doped Cu_3TeO_6 75

4.6.4 Silver doped Cu_3TeO_6 76

4.6.5 Molybdenum and tungsten doped Cu_3TeO_6 77

4.6.6 Pristine Ni_3TeO_6 79

4.6.7 Pristine Fe_2TeO_6 and Eu doped Fe_2TeO_6 80

4.6.8 Pristine Al_2TeO_6 81

4.6.9 Tungsten doped Ni_3TeO_6 82

4.6.10 Molybdenum doped Ni_3TeO_6 83

4.6.11 Manganese doped Cu_3TeO_6 84

4.6.12 Zinc doped Cu_3TeO_6 85

4.7 Transmission Electron Microscopy (TEM) 85

4.7.1 Pristine Cu_3TeO_6 85

4.7.2 Cobalt-doped Cu_3TeO_6 86

4.7.3 Nickel doped Cu_3TeO_6 87

4.7.4 Pristine Ni_3TeO_6 88

4.8 X-ray Photoelectron Spectroscopy (XPS) 89

4.8.1 Pristine Cu_3TeO_6 89

4.8.2 Cobalt-doped Cu_3TeO_6 90

4.8.3 Nickel doped Cu_3TeO_6 92

4.8.4 Manganese doped Cu_3TeO_6 93

4.8.5 Zinc doped Cu_3TeO_6 94

4.8.6 Tungsten doped Cu_3TeO_6 95

4.8.7 Molybdenum doped Cu_3TeO 96

4.8.8 Silver doped Cu_3TeO_6 97

4.8.9 Pristine Ni_3TeO_6 98

4.8.10 Pristine Fe_2TeO_6 99

4.8.11 Pristine Al_2TeO_6 100

CHAPTER 5

5 MATERIAL STUDIES AND OTHER INVESTIGATIONS 102

5.1 Electrical resistivity (ρ) 103

5.1.1 $Cu_{3-x}Co_xTeO_6$ (x=0.1 – 0.5) 103

5.1.2 $Cu_{3-x}Ni_xTeO_6$ (x=0.1 – 0.5) 105

5.1.3 $Cu_{3-x}Zn_xTeO_6$ (x=0.2 and 0.5) 106

5.1.4 $Cu_{3-x}Ag_xTeO_6$ (x=0.1) 107

5.1.5 $Cu_3Mo_xTe_{1-x}O_6$ (x=0.1, 0.2) 108

5.1.6 Ni_3TeO_6 *by co – precipitation method* 109

5.1.7 $Ni_3Te_{1-x}M_xO_6$ (x= 0.0, 0.2 and M = W, Mo) 110

5.1.8 $Ni_{3-x}Zn_xTeO_6$ (x = 0.0, 0.2, 0.3 and 0.5) 111

5.1.9 $Ni_{3-x}Co_xTeO_6$ (x = 0.3) 111

5.1.10 Fe_2TeO_6 and Al_2TeO_6 112

5.1.11 $Cu_{3-x}Zn_xTeO_6$ (x = 0.1 – 0.4) 113

5.1.8 $Cu_{3-x}Ni_xTeO_6$ (x = 0.1 – 0.5) 113

5.2 Vibrating sample magnetometer (VSM) 114

5.2.1 Cu_3TeO_6 (x=0.1 – 0.5) 114

5.2.2. $Cu_{3-x}Co_xTeO_6$ (x=0.1 – 0.5) 115

5.2.3. $Cu_{3-x}Ni_xTeO_6$ (x=0.0, 0.1, 0.3, 0.5, 3.0) 116

5.2.4. Fe_2TeO_6 and $Fe_{1.9}Eu_{0.1}TeO_6$ 117

5.2.5. $Cu_{2.9}Fe_{0.1}TeO_6$ 118

5.2.6. $Cu_{3-x}Mn_xTeO_6$ 119

5.2.7. Al_2TeO_6 120

5.3 Thermoelectric power (TEP) 121

5.4 Dielectric studies 124

5.5 Photoluminescence Studies 135

5.6 Other miscellaneous studies 139

5.6.1 Photocatalytic degradation of an organic dye 139

5.6.2 Partial propylene oxidation 140

5.6.3 Antibacterial Activity 141

CHAPTER 6

6. SUMMARY AND CONCLUSIONS 144

6.1 Summary 145

6.2 Conclusions 153

ABBREVIATIONS

AC	Alternating current
BE	Binding Energy
CVD	Chemical vapour deposition
DC	Direct current
DRS	Diffused reflectance spectroscopy
DSC	Differential scanning calorimetry
DTA	Differential thermal analysis
eV	Electron volt
GC	Gas Chromatography
ICP-AES	Inductively coupled plasma – Atomic emission spectroscopy
IR	Infrared
PL	Photoluminescence Spectroscopy
PLD	Pulsed laser deposition
RE	Rare earth
RT	Room Temperature
SEM	Scanning electron microscopy
TEM	Transmission electron microscopy
TG	Thermo gravimetry
T_N	Neel Temperature
TM	Transition metal
UV	Ultra violet
VSM	Vibrating sample magnetometer
XRD	X-ray Diffraction
XPS	X-ray Photoelectron Spectroscopy

ACKNOWLEDGEMENTS

First and foremost, I thank my Almighty my **Sadguru** for constantly blessing me with strength, peace and good fortune and for showing me the way throughout and bringing me to all good people in my life.

I have been very fortunate to be guided by my guide **Prof. A.V. Salker**, Professor Department of chemistry, Goa University, for his decisive advice and valuable guidance, motivation and encouragement throughout my Ph. D. tenure. Words will fall short to portray the kind of understanding and trust he has shown upon me, beyond his professional virtues.

I extend my thanks to **Prof. B. R. Srinivasan,** Head, Department of chemistry, Goa University, former Head **Prof. S. G. Tilve**, **Prof. Gourish Naik**, Dean, faculty of natural sciences, Goa University, former Dean **Prof. J. B. Fernandes** and **Dr. V. M. S. Verenker**, my subject expert, for their solicitous suggestions and continuous evaluation.

I thank **Prof. V. Sahni**, Vice-chancellor Goa University, Registrar **Prof. Y. V. Reddy, Prof. S. Shetye**, former Vice-Chancellor and **Prof. V. P. Kamat** former registrar for allowing us to work in the university and for providing us with the necessary facilities.

I also thank **Prof. V. S. Nadkarni**, **Dr. R. N. Shirsat, Dr .S. N. Dhuri** and **Dr. Pranay Morajkar** for their kind help as and when needed.

I am indebted to **Miss Divya Vaigankar,** Department of Microbiology, Goa University for her kind help in carrying out antimicrobial studies. I would also like to thank **Prof. Uma Subramanian** and **Mr Jaykantham** for providing PL analysis on some samples. I would also like to thank **Mr. Pranav** and **Miss Arundhati**, Department of Physics, Goa University for helping me with the electrical studies.

I express my deep gratitude to **Mr. Girish Prabhu and Mr. Arif Sirdar**, Dona Paula NIO-Goa, **Mr. Jain,** Birla Furukawa, Verna Industrial Estate, for carrying out analysis on my samples, **Mr. Madhusudan Lanjewar**, USIC, Goa University, SAIF-IIT Bombay, SAIF-IIT Madras, ACMS IIT Kanpur, NCL Pune, Alagappa University for providing instrumental facilities for characterisation of my compounds.

I would like to thank UGC BSR fellowship for providing financial assistance during my Ph. D.

My deepest gratitude to **Dr. Shambhu S. Parab** for his valuable suggestions, devotion in sharing knowledge, and also in helping carry out oxidation studies on some of my compounds. I would like to thank **Mr. Chandan C. Naik** from the depth of my heart for being there always and for helping me throughout. My sincere thanks go to **Dr. Madhavi Z. Naik** for her kind and ever helping nature, encouragement and guidance. I am very grateful to my friend **Dr. Celia Braganza**, for always being there with positive energy around, **Mr. Rahul D. Kerker, Dr. Mira Parmekar** and **Dr. Mithil Faldessai** for their kind and approachable nature during my Ph. D in turn constituting a very healthy environment.

I also thank my seniors Dr. Satu Gawas, Dr. Durga Kamat, Dr. Savita Khandolkar, Dr. Sagar Patil, Mr. Daniel Coutinho, Dr. Prajesh Volvoikar, Dr Kiran Dhavasker, Dr. Dattaprasad Narulkar, Dr. Shrikant, Dr. Rohan, Rita and my friends, Prajyoti, Pratik, Apurva, Kedar, Sudesh, Pooja, Sarvesh, Pratibha, Mayuri, ishnu, Madhavi, Johnross, Abhijeet, and my juniors Ketan, Shashank, Amarja, Akshay, Luan, Neha, Lima for their support.

I would also like to thank the teaching and non teaching staff of department of chemistry-Goa University.

All credits of my achievements goes to my parents **Mr. Dhanarath N. Mardolkar and Mrs. Sanjeeta D. Mardolkar**, for their unconditional and immense love and countless sacrifices which has made this work possible.

I would like to thank my best friend and husband **Abhimanyu Singh**, for his immense love and support throughout, in whatever I wish to do and for encouraging me to aim higher in life. I would like to thank my brother **Saeesh**, for being there always.

Last but not the least I thank my parents in laws **Mr. L. B. Singh** and **Mrs Anjani Singh**, my cousins and all family members and friends for all the support and understanding.

Chapter 1

Introduction

Introduction

Materials inhabit the peak position in today's techno world as it bounds human life to depend highly on numerous technologies for the betterment and welfare of mankind. Materials in diverse forms serve the bases for a variety of systems surrounding us. Material chemistry has played an important role in carving the growth and lifestyle of man over the ages. Hence, there is a need to expand the boundaries for research and innovations in material chemistry in order to achieve greater heights in future goals. The scorching demands for miniature devices as well grow day by day which in turn are associated with the type of material employed.

Materials with energy and cost efficiency has gained enormous demand which has led towards the rise for multifunctional devices, wherein, materials like magneto-electric, multiferroics serve as a strong candidate contributing toward novel applications for modulating their magnetic properties via electrical field [1,2]. Combination of ferroelectricity and magnetism in a single-phase compound would obviously be of tremendous interest not only for practical applications but also for fundamental science [2–5]. Yet, only a few single-phase multiferroics manifest a strong magnetoelectric coupling [1,6–9]. Since multiferroics are presently the centre of attention in material science, they get frequently updated [3,10–12].

The field of material chemistry is constantly engaged in developing a sustainable system with adequate electrical-energy storage and generation along with tailoring of magnetic and electronic properties which is one of the most studied current research topics as well as a challenge in condensed matter science [13,14].

Materials in the form of conductive transition metal oxides have gained much attention and interest in technological fields owing to their exceptional electronic, optical, magnetic and catalytic properties [15].

Novel materials are being investigated with novel thermoelectric performances with improved efficiency of thermoelectric devices and operation costs in order to widen the range of their applications [16]. Materials in the form of sensors play an important role in to-days world, for example, chemical sensors are significantly useful in detecting and monitoring poisonous chemicals and researchers around the world are trying to develop such chemical sensors with superior skills [17].

Metal oxide semiconductors are considered to be the most common sensors bearing advantages like cost efficiency and soaring sensitivity. Generally, transition metal oxide semiconductors such as ZnO, SnO_2, WO_3, CuO, Fe_2O_3, In_2O_3, CdO, TeO_2 and MoO_3 are preferred as sensor materials over non transition ones, as transition metal oxides provide variable oxidation state reach surface for the sensor material to work productively, which is rather not possible by non-transition metal oxide possessing only one oxidation state (eg. Al_2O_3) since much more energy is required to form other oxidation states. [17–19]. Chemical sensors are considered vital in areas like gas alarms, sensors for water and soil pollutants, human health, temperature sensor, speed sensor, magnetic field sensor, and emissions control [20,21]. Materials with variety of morphologies are used for gas sensing applications as they possess high electron mobility, no toxicity, high-specific surface area, good chemical, and thermal stability under operating conditions [17,22,23].

Variable structures of ceramics, the arrangement of ions and their different phases add up to the fields of material chemistry which are dependent up on the nature of its constituent cations including distortions and ordering. For example, contribution of ceramics with perovskite structure to the multiferroic research [3]**.**

Tellurium based materials find applications in lasers and non – linear optics devices due to their great structural interest [24]. Also, it is well known to contribute in the development of innovative new materials. In general, A_3TeO_6 (A=Mn, Co, Ni, Cu) with a perovskite-like structure have attracted interests as potential ferroelectrics [25,26]. Applications of Te recently have come in the view in different fields including metallurgy, glass industry, electronics, and applied chemical industries along with its much gained curiosity in various research fields [27].

Tellurite (TeO_3^{2-}) glasses are utilised as a material for photonic switches since Te compounds show remarkable thermal, optical and electronic properties. This leads to applications of tellurium in form of polychalcogenides in the field of solid state materials, *e.g.* for rechargeable batteries [28,29].

Tellurates are generally more stable than tellurites [28]. The novel first row transition metal tellurate show rich crystalline chemistry [3,13,26,30]. They posses ferro-electricity, ferromagnetic and simple anti-ferromagnetic spin orders, complex incommensurate spin structure and magnetic-field-driven polarization [13,31]. Rich structural chemistry of Tellurites, i.e., oxides containing Te^{4+} cations often tend to show variable properties required for various applications. TeO_2, with a melting point of 733 °C, exhibits not only an excellent solubility in many solvents but a superior reactivity with other oxides [14].

Mn_3TeO_6 has been reported recently to exhibit a complex incommensurate spin structure, consisting of two different magnetic orbits. The interesting structural features of Co_3TeO_6 have strongly influenced its magnetic ordering [13]. Ni_3TeO_6 exhibits a non-hysteretic colossal magneto-electric effect [1,32].

Scientists today focus principally on the method of synthesizing a material in desired composition and properties with specific application, which is a tricky challenge to

accomplish. We all know how a particular method of synthesis delivers a material with special physico-chemical features. Synthesis thus, is a crucial step towards obtaining a particular compound which has power to control the composition, morphology, structure as well as properties of a preferred material. Hence, a number of methods for synthesis have been implemented previously in literature like solid state method [33–43] melt quench technique [44] flux growth for single crystals [45,46], hydrothermal, chemical vapour transport [25,26,30,47–49].

Doping or substitution of any material with another element is known to bring about change in its properties thus changing its applicability. It allows one to tune or advance the skills of a material and in turn provide immense output to the techno world. In the present research, various dopants are chosen to alter the behaviour of pristine composition due to their ability to hold some interesting physical properties. In the present work, special attention has been given to produce a significant method of synthesis, keeping the safety of the environment in mind. So, a simple technique of co-precipitation has been utilized for the first time along with sol gel method to a lower waste extent. Prepared compounds are characterized by various techniques and are explored for various properties and studies.

Catalytic properties of tellurium containing compounds are mainly restricted to organo tellurium compounds [50] and elemental tellurium [27,51] and very scarcely to oxide of tellurium [52] [53]. Hence, it is very much required to introduce these materials to the field of catalysis. Tellurium is biologically significant, [27,28] as well as present good antimicrobial activity [54,55].

The world of technology is constantly aiming in bringing about newer and sophisticated innovations for the advancement of mankind in numerous forms and this has fascinated us to carry out research in material field. The present research includes preparation of certain selected transition metal tellurates which are chosen based on their ability to show various properties.

Highlights of the Thesis

- Tellurates of the transition metals and a few non transition metals have been successfully obtained in pristine as well as in doped / substituted forms by a very simple, environmental friendly wet chemical co-precipitation method for the first time and a few by sol gel method using citric acid as a complexing agent.
- All the prepared compositions have been precisely characterized by various instrumental techniques like X-ray diffraction (XRD), Thermal analyses (TG-DTA/DSC), Infrared spectroscopy (IR), Ultra Violet-Visible Diffused reflectance spectroscopy (UV-DRS) and X-ray photoelectron spectroscopy (XPS). Inductively coupled plasma atomic emission spectroscopy (ICP-AES) has been utilized on some compounds of tellurium. Morphological characterization have been carried out using techniques like Scanning electron microscopy (SEM) and transmission electron microscopy (TEM).
- Material studies like DC electrical resistivity by two probe method, thermoelectric power (TEP), dielectric studies, magnetic studies by vibrating sample magnetometer (VSM) have been employed to prepared compounds for better understanding their applicability. Certain selected compounds were studied for photoluminescence property.
- Other miscellaneous studies like photo-degradation of an organic dye, partial propylene oxidation and antibacterial studies have been carried out employing these selected materials to recognize their extra-curricular performance.

The present thesis is organized as follows:

Chapter 1. Introduction: Brief introduction on various metal tellurates, along with aim and significance regarding the topic is highlighted.

Chapter 2. Literature review: Literature survey on the preparative methods and their research is reported.

Chapter 3. Experimental section: Details regarding the preparative procedures for metal tellurates are discussed.

Chapter 4. Characterisation and Spectroscopic studies: Various instrumental techniques and characterization implemented on compounds are presented along with structural and spectroscopic studies.

Chapter 5. Material Studies and Other Studies: Material properties like electrical, magnetic etc are discussed in detail. Also other studies like photo-degradation, partial propylene oxidation and antibacterial studies on pathogens are reported.

Chapter 6. Summary and Conclusion: The results obtained from all the properties are summarized based on the conclusions derived.

Chapter 2

Literature Review

Compounds based on chalcogens exhibit exceptional properties in electrical, magnetic, thermal, optical and others which are commonly employed in recent technologies and in different multifunctional systems. Various parameters [56] like compositions, structural arrangements, synthetic routes etc decides the behaviours of the prepared compounds. From this point of angle, the widespread study of compounds based on tellurium exhibiting such physical and chemical properties as semiconductor, magneto electric and piezo electric focused the attention of the investigators the world over.

Current investigations in the synthesis of both transition metals and non-metals show a variety of physical and chemical properties. Therefore, a systematic approach is laid down for the research in the preparations of new tellurium based compounds with distinct physical, chemical and electronic properties [57,58].

The oxides containing tellurium exhibit a complex structural chemistry such as layer-type structure [59–61], perovskite-type structure [62–65], garnet-type structure [66] and fluorite-type structures [67], or other forms, owing to their diverse co-ordinations of Te (IV) and Te (VI) in the compositions.

Based on the structure, these oxides can show different properties, including ferroelectricity as in the cases of ($(NH_4)_2Te_2WO_8$) [61,68,69] magnetic (A_2CoTeO_6 (A=Ca, Sr) [63], $A_2CuB`O_6$ (A=Ba, Sr; B`=W, Te)[65], ion conducting ($Li_{3+x}Nd_3$-$Te_{2-x}Sb_xO_{12}$) [66] and thermoelectric (Cd_3TeO_6) [70,71]

Most tellurium-based oxide materials showed potential application in low temperature co-fired ceramics (LTCC) technology as they can be prepared and sintered at low temperatures [72,73].

In this connection, we perform a systematic research and development of the scientific base for the targeted synthesis of new tellurium compounds with unique physical and chemical properties.

Tellurium is a chemical element of Group 16 like oxygen, and is able to display various oxidation states including -2, +2, +4 and +6 [74]. Tellurium (Te) exists in three main forms in the environment: elemental (Te^0), inorganic [telluride (Te^{2-}), tellurite (TeO_3^{2-}), tellurate (TeO_4^{2-})] and organic [dimethyl telluride (CH_3TeCH_3), dimethyl ditelluride ($CH_3TeTeCH_3$)] [75]. Tellurium, like sulfur and selenium readily forms oxides which can be hydrolyzed to produce oxy-acids. The more metallic nature of tellurium and its amphoteric behaviour are reflected in the chemistry of the oxides and oxy-acids.

Considerable data are available on the most stable oxide, tellurium dioxide. However, much less is known of the other oxides, TeO, TeO_3, and Te_2O_5. The pentoxide was discovered only recently as one of the products of the thermal decomposition of orthotelluric acid, H_6TeO_6 [76]. Generally, tellurium ions involved in an oxide exist in +4, +6 or their mixed valence.

2.1 Oxyanions and oxyacids of tellurium

Compound containing an oxy-anion of tellurium where Te has an oxidation number of +6 is called tellurate. Historically, name tellurate was only applied to oxy-anions of Te with oxidation number +6, formally derived from telluric acid, H_6TeO_6. Name tellurite referred to oxyanion of Te with oxidation number +4, formally derived from tellurous acid, H_2TeO_3. However, tellurate and tellurite are often referred to as tellurate (VI) and tellurate (IV) respectively in line with IUPAC.

Anion Te^{-2} and its derivatives are termed as tellurides. Many metal tellurides are known including some telluride minerals. Of the oxy-acids, H_2TeO_3, H_6TeO_6 and H_2TeO_5, orthotelluric acid is of particular interest in view of the marked difference in its structural and ionization properties from those of the corresponding sulfur and selenium acids and of its tendency to polymerize to form meta-telluric acid, (H_2TeO_4) [77].

During the last several years, scientists have focused on preparation and characterization of multi-component tellurates in single crystal, polycrystalline or thin film form, examples being Cd_3TeO_6 [70,78], $Cd_{3-x-y}Cu_xA_yTeO_6$ (A = Li and Na) and Ca_2MTeO_6 (M = Mn, Co and Mg) [79] These compounds display some special structures and resultant properties due to the existence of tellurium ions. It is believed that more new compounds are required to further investigate the peculiarity of these multi-component tellurates.

2.2 Uses of tellurium

Tellurium's major use is as an alloying additive in iron, steel, and copper to improve machining characteristics. It is also used as a catalyst in the chemical industry and in electronic applications, such as photoreceptors and photovoltaic devices.

The largest use for tellurium was as a metallurgical alloying element. Approximately 60% of the market demand for tellurium was in steel, as a free-machining additive; in copper, to improve machinability while not reducing conductivity; in lead, to improve resistance to vibration and fatigue; in cast iron, to help control the depth of chill; and in malleable iron, as a carbide stabilizer.

Chemicals and catalyst usage made up about 25% of the world market with tellurium being used as a vulcanizing agent and accelerator in the processing of rubber and as a component of catalysts for synthetic fibre production. Electrical uses, such as photoreceptor

and thermoelectric applications, accounted for about 8% of tellurium demand. Other uses, as an ingredient in blasting caps and as a pigment to produce various colours in glass and ceramics, were about 7% of consumption [80]

Tellurium catalysts are used chiefly for the oxidation of organic compounds but are also used in hydrogenation, halogenation, and chlorination reactions. Tellurium dioxide is used as a curing and accelerating agent in rubber compounds. High-purity tellurium is used in electronics applications, such as thermoelectric and photoelectric devices. Thermal imaging devices use mercury-cadmium telluride as a sensing material.

Semiconducting materials using bismuth telluride are being employed in electronics and consumer products as thermoelectric cooling devices. These devices consist of a series of couples of semiconducting materials, which, when connected to a direct current, cause one side of the thermo-element to cool while the other side generates heat. These thermoelectric coolers are most commonly used in military and electronics applications, such as the cooling of infrared detectors, integrated circuits, medical instrumentation, and laser diodes. Their application in consumer products, such as portable food-and-beverage coolers, continues to increase.

Also, tellurites are of importance for their special properties such as non-linear optical properties, and electrical and ionic conductivities [81]. The asymmetric coordination polyhedron adopted by Se (IV) or Te (IV) atoms may result in non-centrosymmetric structures with consequent interesting physical properties, such as non-linear optical second harmonic generation (SHG) [82]. Furthermore, “lone-pair” cations such as Se(IV) and Te(IV), when mixed with a transition metal in the presence of halogenide anions, can be regarded as “chemical scissors” [83]. A critical review on the preparation, applications and properties of compounds of tellurium is presented by [80].

The present research includes investigation and preparation of certain selected transition metal tellurates which are chosen based on their ability to show various properties.

Various synthetic methodologies have been reported in the literature for synthesizing tellurium containing compounds.

Frank C. Mathers and Gail M. Bradbury prepared calcium tellurate by heating a mixture of tellurium dioxide and calcium hydroxide, oxidising it completely to calcium tellurate which on further treatment with nitric acid yield telluric acid [84].

Y. Dimitriev, E. Gatev and Y. Ivanova studied oxidation of $CuTeO_3$. Despite the fact that TeO_2 decomposes above 800 °C, there are other investigations [85] which show that some tellurites, especially those with heavy ions are oxidized to tellurates at high temperatures [86].

The novel metal tellurates M_3TeO_6, where M is a first-row transition metal, have been shown to be rich in crystalline chemistry [3,13,26,30]. Ferroelectricity [30], ferromagnetic and simple antiferromagnetic spin orders, complex incommensurate spin structure, and magnetic-field-driven polarization have all been observed [31].

2.3 Al_2TeO_6

2.3.1 In-general

There appear very few reports on the study of this material. Al_2TeO_6 ceramics are very useful ceramics in the fields of LTCC as they contain TeO_2 which is characterized by its low melting point [35,87,88] which is the most essential feature applicable in densification of compounds by sintering at lower temperature [87,89–92] and hence are suitable for high frequency applications [35,89]. Besides this, TeO_2 is a well known network former in the glass industry, reflecting glass good optical performance and chemical durability [35,93,94].

Although Al_2O_3 possess a variety of properties like low dielectric losses, good thermal conductivity, high mechanical strength, low fabrication cost, it requires a very high sintering temperature (~1600 °C)which limits its application and increases the preparation cost [35,87,95–99]. Addition of a glass to a material like Al_2O_3, seems to decrease its sintering temperature. Hence, this opens the door for the synthesis of Al_2TeO_6 as it will possess low sintering temperature; at the same time maintain a good dielectric property.

2.3.2 Synthesis reports:

Bayer in 1962 provided a first report on the formation of Al_2TeO_6 for 1: 1 stoichiometry under oxidizing atmospheres at temperatures between 650 and 700 °C and determined its crystal structure to be tetragonal tri-rutile [35]. The tri-rutile structure contain linear chains of edge-sharing octahedral with compositional sequence Al-Al-Te [100], Te^{6+} ion site symmetry in D_{2h}.

2.3.2.1 Solid State technique:

This is the most extensively studied method of producing a material and so is implemented by most of the chemists and physicist worldwide. It is the simplest method of obtaining a material and does not depend on various parameters like pH, rate of heating, time etc. like those of wet chemical synthesis. It involves mechanical grinding of two reactants together with in between heating the mixture. This process of heating and grinding continues till compound is formed. Hence, it is also called a ‘heat - beat technique’. This could be also achieved via ball milling wherein reactants are fused together using balls made of alumina or zirconia, which mill the composition in between them in the process of rubbing each other in an air tight cup under high speed rotations. However, this method holds several drawbacks such as non-homogeneity, time and energy consumption etc.

Xinming Su, Aiying Wu and Paula M. Vilarinho studied mechanism of phase formation and dielectric properties of Al_2TeO_6. It was synthesized by a very common method of ball milling solid state technique using zirconia balls. TeO_2 and Al_2O_3 powder mixtures were taken in the ratio 1: 1, ball milled with ethanol for 24 hours and dried at 70 °C in an oven. Further, the powders were calcined at 620 °C for 30 hours. Finally, after calcinations, the samples were ball milled for 24 hours in a planetary ball mill at 200 rpm using Teflon pots and zirconia balls [35].

A similar methodology was implemented by I. Kagomiya, Y. Kodama *et al*, by slightly modifying the heating temperature and composition for Al_2TeO_6-TeO_2 composite. Al_2O_3 and TeO_2 were weighed in the molar ratio 1:1 and was ball milled with ethanol for 24 hours using alumina balls. After drying, the mixed powders were calcined in air at 550-650 °C for 10 hours. The calcined powders were mixed with additional TeO_2 of 30-50 wt% and were again ball milled for 24 hours. The prepared powders were moulded into pellets, which were again sintered and studied for microwave dielectric properties [87]

Studies carried out by [35] has shown that the oxidation of tellurium dioxide to TeO_3 triggers the reaction between the starting reactants and is found to be crucial to the formation of Al_2TeO_6. I. Kagomiya *et al* [87] investigated a low temperature sintering condition for Al_2TeO_6 – TeO_2 ceramics for their microwave dielectric properties. G. Blasse et al presented a report on the luminescence study on Al_2TeO_6 doped U^{6+} which showed only a weak green luminescence far below room temperature [100].

2.4 Fe_2TeO_6

2.4.1 In-general

This metal tellurate of iron is found to be of great use as it exhibits magnetoelectric coupling - a very useful property of a material for various technological applications [101]. It is an antiferromagnet and highly suitable for switchable exchange bias applications [102–106]. Junlei Wang et al demonstrated Fe_2TeO_6 materials with dissipationless switching of boundary magnetization possible through voltage control [103]. These materials hold several applications such as magnetic random access memory, transducers, sensors, fourth state logic systems, exchange biased hetero structured magnetic memory [2,107].

2.4.2 Structure and Properties:

Fe_2TeO_6 is found to crystallize in tri-rutile tetragonal structure with $P4_2/mnm$ space group and was first reported by Bayer [101,102].

Figure below depicts the crystal structure of Fe_2TeO_6 that is, tetragonal trirutile with space group *P42/mnm*. It is clearly seen that each Fe and Te atom is surrounded by six oxygen atoms in an octahedral coordination. The cation oxygen octahedra form edge sharing chains which are alternately occupied by FeO_6 and TeO_6 octahedra in the ratio of 1:2. [102,104,108–111].

The cations are at the centres of the octahedra and alternate regularly AABAABAAB along the c axis. The closest Fe-Fe distance is 3.0 Å along the c axis with iron pairs each bridged by two oxygens with Fe-O-Fe angle of about 100°. The closest Fe-Fe distance between neighbouring chains is 3.6 Å and each iron is linked to four others by single oxygens with an Fe-O-Fe angle of about 140°[106,112,113].

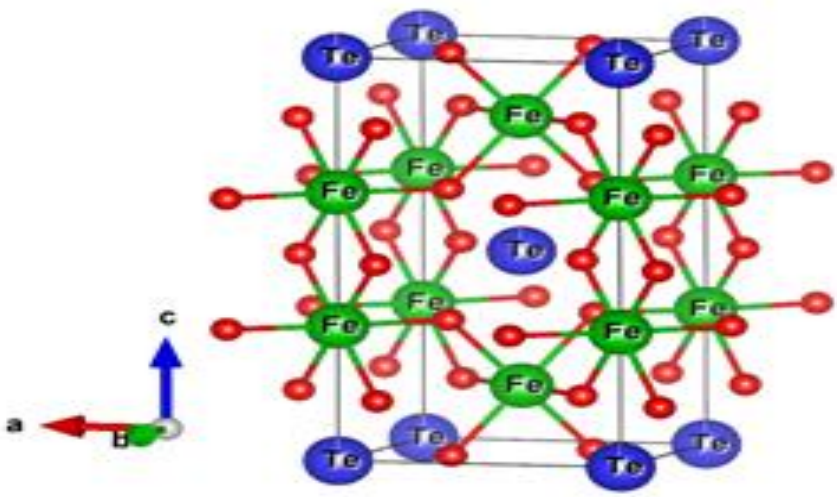

Fig. 2.1 Schematic structure of Fe_2TeO_6.

2.4.3 Magnetic structure of Fe_2TeO_6

The magnetic structure of Fe_2TeO_6 is shown in the figure below. Iron tellurate exhibits magnetoelectric coupling and orders antiferromagnetically at a temperature about 210 K, with spins are directed along c-axis. Its structure holds two molecules per unit cell. The Fe^{3+} ion lie in the 4 (e) sites with mm symmetry and the Te^{2+} ion lie in 2 (a) sites with symmetry mmm [106,111,112].

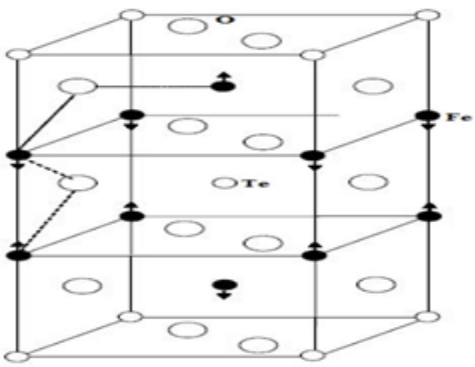

Fig. 2.2 Magnetic structure of Fe_2TeO_6

2.4.4 Synthetic methodology:

Various synthesis approaches have been employed by researchers earlier to produce iron tellurate in different forms like single crystal, powder, thin films etc.

2.4.4.1 Solid state method

This is the vigorously studied method by researchers all over the world as it is the simplest way to carry out polycrystalline solid. The starting materials are grounded properly to get good contact between the grains so they can react. The grounded compound is then made in the form of pellets by pressing it under pressure. These pellets are sintered further at 700 °C for 24 hours and crushed. In order to obtain homogeneity, the crushed powders are re-formed into pellets and sintered again [101,106–108].

Similarly, F. J. Berry, T. Birchall *et al* carried out synthesis of iron chromium tellurates by simply heating the metal oxides in air at 690 °C [43,104,110,112,114–117].

W. Kunnmann et al slightly changed the solid state synthesis, in which elemental tellurium and metal oxide were slowly heated initially (approx. 100 °C per day to 600 °C) to allow air oxidation of the tellurium with subsequent reaction. After this initial firing, the standard procedure of repeated grinding and firing at 700 °C was employed until an X-ray powder diffraction produced a single tetragonal phase [111].

Yan-Nian Shyr and Geoffrey L. Price synthesized iron tellurates as catalyst for the selective oxidation of 1-butene and propylene by taking $Fe(OH)_2$ prepared freshly via precipitation of $FeCl_2$ using aqueous NH_4OH and TeO_2 powder in 1:1 atomic ratio for Fe/Te in the case propylene oxidation and 2:1 atomic ratio of Fe/Te for 1-butene oxidation. This mixture was heated at 400 °C for 10 hours [53].

2.4.4.2 PLD technique

This is a very versatile, simple and time saving technique for producing compounds in the form of thin films which are highly useful for various technological applications. In this technique, a high-power pulsed laser beam is focussed to hit the target of the material that is to be deposited. This leads to ejection of plume (vapour) which is collected / deposited as a thin film on a substrate placed a short distance from a target. A plume of material is produced inside a vacuum chamber by the laser induced expulsion with stoichiometry similar to the target. Based on this technique, one can design a multi-element material for various applications in material study.

Highly textured iron tellurate thin films were grown by pulsed laser deposition by J. Wang et al. They first synthesized fine powders of Fe_2TeO_6 to be used as target material to generate thin films using solid state synthesis [103,112] which were then moulded into pellets which were sintered at 975 K. This target material was subjected to the energy of KrF excimer laser (130 mJ per pulse with 10 Hz pulse rate). The target was kept at a distance of 10 cm relative to the Al_2O_3 substrate, which was maintained at 300 °C for deposition time of 1 hour to achieve relatively thick films (several 100 nm) [103].

2.5 Ni_3TeO_6

2.5.1 In-general

Ni_3TeO_6 is very interesting metal tellurate with collinear antiferromagnet like behaviour and possesses magnetism, magnetic-field-driven electrical polarization [25,26,31]. Lei Xu, Chuanxiang Qin *et al.* presented a very first report on photochemistry of Ni_3TeO_6 as a result of small band gap suggested it to be an effective photocatalyst [25].

R. Mathieu, S. A. Ivanov *et al.* in 2013 investigated and analysed the structure and magnetic properties of doped Ni_3TeO_6 which show antiferromagnetic ordering at higher temperature than the pristine compounds [118]. M. Ali, R. Mishra *et al.* performed transpiration studies on Ni_3TeO_6 solid [119].

Raman Sankar, G. J. Shu et al obtained single crystal of Ni_3TeO_6 by flux growth method for the first time with ferromagnetic ordering studied for their growth and orientation. [31]. Zivkovic et al studied magnetic properties of nickel tellurate [26].

2.5.2 Synthesis

This compound has been prepared by several methods to obtain various forms like powders, single crystals etc.

2.5.2.1 Solid State method

Polycrystalline yellow-green Ni_3TeO_6 ceramics were prepared by solid state reaction of NiO and TeO_2 at 840 °C for 12 hours in air by R. Newnham and E. P. Meagher [120].

Similar method of synthesis by solid state was reported by Raman Sankar, G. J. Shu [31] which was used to produce polycrystalline Ni_3TeO_6 with NiO and TeO_2 taken in 3: 1 molar ratio in an alumina crucible, mixed well and calcined at 750 °C for 15 hours in air. The powder was further pressed into pellet and heated up at 800 °C for 2 days and then 830 °C for 2 days in air with intermediate grinding [121].

Ni_3TeO_6 was prepared by mixing NiO and TeO_2 in the molar ratio of 3: 1 and heating the mixture in a platinum boat in air at 1073 K for 24 hours with intermittent grinding [119]. C. Mallika and O. M. [122], by solid oxide electrolyte e.m.f. method. Manjulata Sahu *et al.* [115,122] G. Blasse and W. Hordijk [123] N. V. Golubko *et al.* [38] L. Zhao *et al.* [124]

Gerhard Bayer [85] Zupan *et al.* prepared Ni_3TeO_6 powders by mixing stoichiometric amounts of NiO and TeO_2 by solid state reaction [85,120] at 700 for 25 hours and then at 800 for 10 hours [125] G. M. Kaleva [34].

Single crystal of Ni_3TeO_6 and ceramics were synthesized by R. Mathieu, S. A. Ivanov *et al.* by Chemical transport [26,48,118] and solid state reactions respectively [126].

Green Ni_3TeO_6 polycrystalline powders and single crystals were synthesized by Stella Skiadopoulou *et al.* by solid state and flux growth methods from stoichiometric amounts of analytical grade NiO and TeO_2 and heating the mixture at 800 °C for 12 hours in O_2 flow in the case of solid state method. The single crystals were grown from a flux composed of the previously prepared powders of Ni_3TeO_6,V_2O_5,TeO_2,NaCl, and KCl in a molar ratio of 1:5:10:10:5. The mixture was heated for three days at 830 °C and then cooled down to 600 °C during five days. Plate-shaped green single crystals of 2 mm in diameter and with thicknesses 60–100 μm were obtained [1].

2.5.2.2 Chemical Transport method

Single crystals of Ni_3TeO_6 were synthesized by chemical transport by [126]. I. Zivkovic *et al.* [26] produced single crystals of Ni_3TeO_6 via chemical vapour transport reactions from the non–stoichiometric molar ratio NiO:CuO:TeO_2:$NiCl_2$ in 4:1:3:1 and then mixed this composition in an agate mortar and placed in a quartz ampoule which was evacuated to 10^{-5} torr and sealed. This ampoule was heated in a tube furnace at 700 °C for four days followed by slow cooling. The ampoule was placed in a two-zone gradient furnace between 750–600 °C and after ten weeks, two different compounds were observed as single crystals that is copper doped nickel tellurate towards one end and triclinic plates of nickel tallurate on the other end [26,127]

2.5.2.3 Flux growth method

Orientational Ni_3TeO_6 single crystals were grown using flux slow cooling method. Mixture of NiO, TeO_2 and Na_2O in molar ratio 3: 6: 2 was placed in a platinum crucible and subjected to temperature of 825 °C in furnace for 3 days to melt to homogenous liquid and then the temperature was lowered down to 600 °C. With slow cooling, high quality single crystals were obtained along the crucible wall [31]. Michael O. Yokosuk *et al.* [128].

Ni_3TeO_6 polycrystalline powders and single crystals were synthesized by Stella Skiadopoulou *et al.* [1] by solid state and flux growth methods from stoichiometric amounts of analytical grade NiO and TeO_2 and heating the mixture at 800 °C for 12 hours in O_2 flow in the case of solid state method. The single crystals were grown from a flux composed of the previously prepared powders of Ni_3TeO_6, V_2O_5, TeO_2, NaCl, and KCl in a molar ratio of 1: 5: 10: 10: 5. The mixture was heated for three days at 830 °C and then cooled down to 600 °C during five days. Plate-shaped green single crystals of 2 mm in diameter and with thicknesses 60–100 μm were obtained.

2.5.2.4 Sol – Gel method

Lei Xu *et al.* synthesized nickel tellurate by sol gel route using $Ni(NO_3)_2{\cdot}6H_2O$ and H_6TeO_6 in stoichiometric amount. Citric acid as gelling agent was added in the ratio, twice the molar weight of Ni^{2+} and Te^{6+}. Aqueous PVA was added to adjust its visco-elasticity till it becomes sticky while stirring the solution for 3 hours at 80 °C. This viscous solution was carefully coated on the glass substrates and wind dried to obtain precursor thin films. The films were peeled off from the glass-substrates, which contain Ni^{2+}, Te^{6+} ions and some organic components (citric acid and PVA). It was finally sintered at 600°C for 2 h to get Ni_3TeO_6 nanoparticles [25].

2.5.3 Structure and Properties:

R. E. Newnham and E. P. Meagher reported structural details on Ni_3TeO_6 revealing its structure to closely resemble corundum with octahedrally co-ordinate Ni^{2+} and Te^{6+} to a distorted hexagonal close packed array of oxygens. It was found to crystallize in polar space group R3 and the reflections obey the rhombohedral lattice [25,120,129,130]

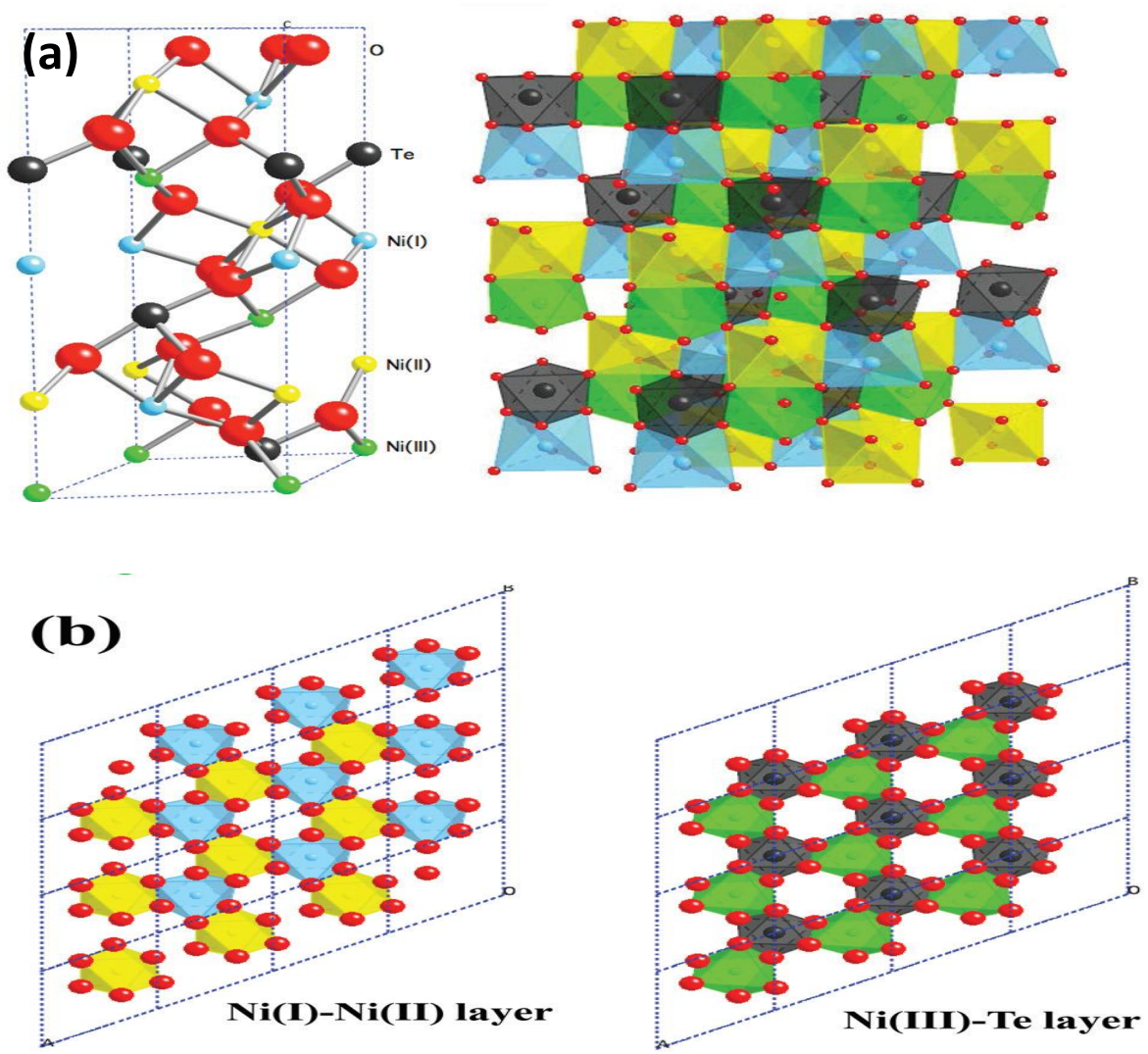

Fig. 2.3 (a) Crystal structure of Ni_3TeO_6 unit cell in ball-and-stick and polyhedral views showing stacked NiO_6 and TeO_6 octahedra with Ni(I) in blue, Ni(II) in yellow, Ni(III) in green, and Te in black, (b) $Ni(I)O_6$–$Ni(II)O_6$ and $Ni(III)O_6$ – TeO_6 honeycomb ring layers are stacked following R3 symmetry [31].

Trigonal symmetry with a space group of R3 (Fig. 2.3 (a)) shows the crystal structure of Ni_3TeO_6. It can be viewed as consisting of two stacking layers of NiO_6–NiO_6 and NiO_6–TeO_6

honeycomb rings. The $Ni(I)O_6$ and $Ni(II)O_6$ octahedra form a slightly corrugated honeycomb layer, while the $Ni(III)O_6$ octahedra form a trigonal layer in the adjacent plane without considering Te. Alternatively, we can include TeO_6 to describe $Ni(III)O_6$–TeO_6 as a layer of honeycomb rings that stack with the $Ni(I)O_6$–$Ni(II)O_6$ layer, as shown in Fig. 2.3 (b)

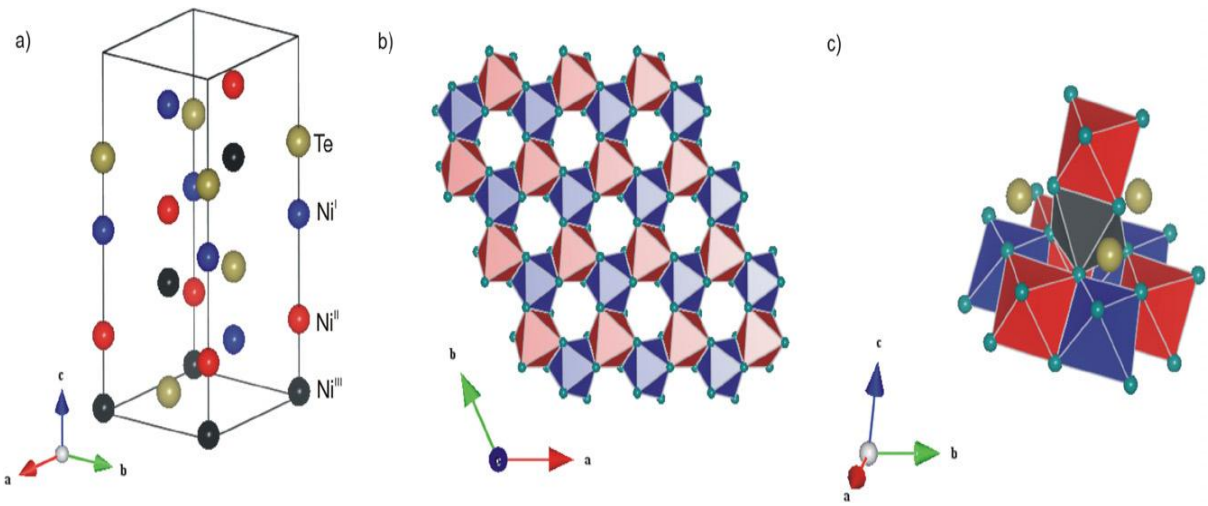

Fig. 2.4 Different views of the structure of Ni_3TeO_6 a) Unit cell (b) the view along the c axis with its hexagonal structure and (c) the link between the Ni (I) - Ni (II) hexagon and the Ni (III) octahedron (black) along the c axis [26].

Different views of the structure of Ni_3TeO_6: (a) the unit cell (oxygen ions are removed for clarity, Ni (III) placed at the origin), (b) the view along the *c* axis on the *ab* plane with its hexagonal structure and (c) the link between the Ni (I) – Ni (II) hexagon (blue and red) and the Ni (III) octahedron (black) along the *c* axis. Ni (II) ion (red octahedron) on top of Ni (III) belongs to the adjacent plane [26].

2.6 Cu_3TeO_6

2.6.1 In-general Cu_3TeO_6

This is the most stable composition in the CuO-TeO_2 system with interesting electrical properties due to presence of copper and tellurium. Cu serves in microelectronics as a potential electrode thus showing possible applications in base metal electrode multilayer ceramic capacitor (BME - MLCC) and low temperature co-fired ceramics (LTCC) in Cu_3TeO_6.

Te based compounds also possess useful applications in BME-MLCC and LTCC due to their low synthesis and sintering temperature and good dielectric properties [36,72,89–91,131]

Xiaoli Zhu *et al.* reported on the phase formation and systematic studies on the ceramic fabrication and its electrical properties providing understanding about Cu_3TeO_6 species [36]. Herak *et al.* [30] studied about the magnetic properties of single crystals of Cu_3TeO_6. It is reported to be a three dimensional antiferromagnet with spin web lattice [30,45,46,48,132,133]. Cu_3TeO_6 compound is an insulating material which belongs to an intriguing group of compounds where the magnetism is governed by $3d^9$ copper Cu^{2+} ions and shows antiferromagnetic transition at T_N ~60 K [45,48,49,133,134]. M. Herak, H. Berger reported studies on the magnetic properties by ac and dc susceptibility, torque magnetometry and neutron powder diffraction [30].

2.6.2 Structural properties

The crystal structure of Cu_3TeO_6 was calculated for the first time in 1968 by A. Hostachy *et al.* and revised in 1978 [36,134]. It has a cubic structure with space group *Ia3* with unit cell parameter of a = 9.538 Å and is built up by TeO_6 octahedra connected through

copper atoms. Each TeO_6 octahedron is connected to twelve distorted CuO_6 octahedra, forming a unique three-dimensional framework. It shows presence of three remarkable spin lattices – equilateral triangle, isosceles triangle and planar hexagon which are constructed by CuO_6 octahedra via corner sharing or edge sharing [30,45,46,48,49,133,134].

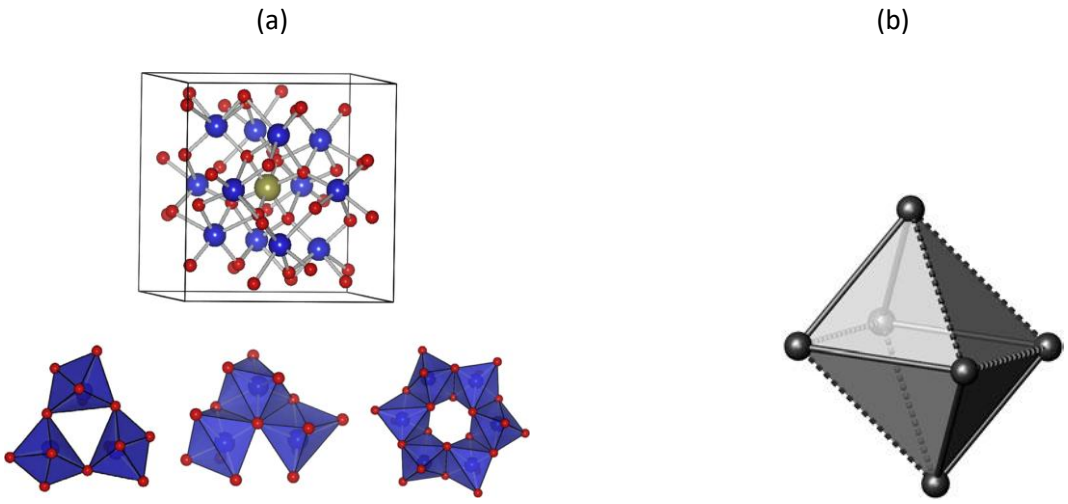

Crystal structure of Cu_3TeO_6 One Copper octahedron

Fig. 2.5 (a) Crystal structure of Cu_3TeO_6 presenting the linkage of a regular TeO_6 octahedron connected to twelve distorted CuO_6 octahedra (b). One copper octahedron [30,46].

2.6.3 Synthesis:

Synthesis has been carried out by various routes as follows:

2.6.3.1 Solid state ball milling method:

This is the widely used method for synthesis of tellurates and so is used for the synthesis of copper tellurate.

X. Zhu, Z. Wang *et al.* reported synthesis of copper tellurate by solid state ball milling reaction between copper oxide (CuO) and tellurium dioxide (TeO_2) powders in the molar ratio $3CuO/1TeO_2$. These components along with ethanol are milled thoroughly in a planetary ball miller im Teflon containers for 24 hours at a constant speed of 200 rpm. After

drying at 60 °C for 10 hours, the mixture was calcined at tempeartures ranging from 400 to 750 °C for 5 h in air [36].

2.6.3.2 Chemical transport method:

M. Herak, H. Berger *et al.* used this method to produce single crystals of copper tellurate by HBr in a sealed quartz tubes with temperatures ranging from 600 °C – 550 °C and 450 °C – 500 °C [30]. M. Mansson *et al.* and Z. He *et al.* used similar method for preparing single crystals of Cu_3TeO_6 [30,46,49]

Similarly, G Caimi *et al.* produced single crystals of Cu_3TeO_6 using polycrystalline $CuTeO_3$ and excess of TeO_2 in a alumina crucible up to 800 °C for 24 h. Platelet like single crystals of Cu_3TeO_6 was obtained on slowly cooling and separating it from the flux [45,48].

2.7 Solid state properties

2.7.1 Electrical properties

Copper is known to possess distinct electrical properties, hence, find its use in various electrical circuits and multi-functional components. M. A. Hassan and C. A. Hogarth studied d. c. electrical conductivity of CuO-TeO_2 glasses which was found to increase with temperature considering electrons as the source of transport and not the ions [135]. Copper containing compounds show effects of strong electronic correlations as well as magnetism in low dimension [36,45]. The electrical properties of Cu_3TeO_6 would be interesting as, this particular material possess antiferromagnetic behaviour. X. Zhu, Z. Wang *et al* elaborated on dielectric properties of Cu_3TeO_6 with respect to frequency and temperature and encountered two interesting anomalies one in lower temperature region and one in the higher [36].

R. Mathieu, S. A. Ivanov *et al* displayed interesting dielectric properties of Ni_3TeO_6 at high temperatures with ferroelectric property below 1000 K [1,118]. L. Zhao *et al* report excellent pyroelectric properties besides dielectric and ferroelectric [124].

$(Cu,Ni)_3TeO_6$ solid solutions prepared by G. M. Kaleva *et al.* investigated dielectric anomalies related to structural phase transitions [34,107,136].

S. D. Kaushik *et al.* investigated structural, magnetic and dielectric properties of Fe_2TeO_6. The temperature dependent dielectric measurements show an intrinsic behaviour of dielectric constant below 150 K [35,87,101,108].

2.7.2 Magnetic properties

All tellurates are highly encountered for their magnetic properties. In the case of Cu_3TeO_6, the magnetism is governed by $3d^9$ copper Cu^{2+} ion. The first investigation of its local magnetic properties was carried out by Martin M. Et al using muon-spin relaxation/rotation (μ+SR) which clearly showed a long-range 3D magnetic order below T_N i.e. 61.7 K [30,49]. Zhangzhen He and Mitsuru Itoh observed magnetic behaviours of the grown crystals by means of magnetic and heat capacity measurements, presenting a long-range antiferromagnetic ordering at around 60 K [46].

K. Y. Choi, P. Lemmens, E. S. Choi and H. Berger reported on the magnetic susceptibility of the S = ½ three-dimensional spin web compound Cu_3TeO_6, which was found to show an antiferromagnetic ordering at T_N 61 K and a deviation from the Curie–Weiss law around 150 K with an evidence of pronounced magneto-elastic effects [48,132,133]. Paramagnetic to ferromagnetic transition at around 185 K followed by an enhanced antiferromagnetic transition 45 K for $Co_{3-x}Mn_xTeO_6$ has been studied by Harishchandra Singh *et al.* [41,42,137,138]. Magnetic properties of doped manganese tellurate was studied by S. A. Ivanov *et al* [47] and the magnetic properties of Ni_3TeO_6 was studied by I. Zivkovic *et al.* and were found to show antiferromagnetic spins below T_N with ferromagnetic planes along one of the axis [26,34].

2.7.3 Optical properties

It is well known fact that the crystal structure has a lot of influence on the optical properties on any compound, and since tellurates show variety of structural modifications they are likely to possess optical properties like phololuminescence. A luminescence study has been carried out by G. Blasse *et al.* on Al_2TeO_6 which they considered interesting due trirutile structure of Al_2TeO_6 containing Al-Al-Te chains and D_{2h} symmetry of Te^{6+} [100].

Near Infrared photoluminescence was reported by Hong-Tao Sun *et al.* on compounds containing tellurium and found that the emissions strongly depend on the excitation wavelengths, most possibly resulting from the co-existence of other Te-related optically active centers [139].

This suggests that other Te containing compounds are expected to show good PL properties which give us an opportunity to explore them in our research.

2.7.4 Catalytic and Antibacterial studies

There appear quite few reports on the catalytic activity of tellurium containing compounds, which are mostly involved with organo-tellurium compounds. Nicola Petragnani and Helio A. Stefani have reported a number of organic reactions over Te-containing reagents [50,52]. Tellurium catalysts are used chiefly for the oxidation of organic compounds but are also used in hydrogenation, halogenation, and chlorination reactions. Tellurium dioxide is used as a curing and accelerating agent in rubber compounds and as a component of catalysts for synthetic fiber production [80]. Haibo Li *et al.* reported an enhanced catalytic performance towards oxygen reduction reaction and methanol oxidation reaction over Te template compounds which served as a sacrificing template as well as a reducing agent which could be attributed to the electronic and geometric structure effects of Te [51]. Iron tellurate

catalysts are reported to be novel catalysts by Yan-Nian Shyr and Geoffrey L. Price to show selective oxidation of 1-butene to butadiene and propylene to acrolein.

It is very interesting to know that Te compounds were used as antimicrobials prior to the discovery of antibiotics, in treating health related problems such as leprosy, tuberculosis, syphilis and other infections [27,140–144]. Potassium tellurite was used by Alexander Fleming in 1932, to isolate gram-positive cocci from the infected media and proposed antibacterial effects of Te comparable to penicillin [145–147]. Te has also been used as a discriminating marker in the selective media to isolate some resistance pathogens including Corynebacterium diphtheriae, Staphylococcus aureus, Vibrio cholera, and Shigella species [141,148] as well as some Te-resistant Rhizobium species from the soil [149]. Tellurite-mediated antibiotic-potentiating effects were indicated by Quiroz *et al* which showed Te to retain synergistic effects with several traditional antibiotics against tellurite-resistant Escherichia coli as well as antibiotic-resistant S. aureus species [27,150]. Antioxidant and antimicrobial activity of tellurium dioxide has been explored by Zhong Cailing *et al*. by oxygen radical absorbance capacity (ORAC) and agar diffusion bioassay method respectively, wherein the antioxidant and antimicrobial activity of sols was found to be dose specific [54].

This literature survey allowed us to understand the past, present and future of all the compounds containing Te and provided lot of information about their synthesis, properties, applications etc. In the present thesis, synthesis of tellurates is achieved by novel route and their various properties are explored.

Chapter 3

Experimental

Various preparative methods have been reported for the synthesis of tellurates which accordingly bring about different structural modifications in the system, resulting change in properties.

Here, we report the synthesis of various pristine and doped metal tellurates by co-precipitation method, which is the most simple, environmentally friendly and by sol-gel method.

3.1 Co-precipitation Method

It is wise to implement such a preparative method, which serve in producing the desired compound at the same time, doesn't harm the environment. Hence, co-precipitation method is the suitable example, which involves precipitation of more than one ion simultaneously with homogeneity in its formation, without producing harmful gases or decomposing matter. Selected metal tellurates are prepared by this method.

3.1.1 $Cu_{3-x}M_xTeO_6$ (M = Co, Ni, Zn and Mn)

Doped and pristine copper tellurates were obtained in their pure form by co-precipitation method. A series of $Cu_{3-x}Co_xTeO_6$ (x = 0, 0.1, 0.2, 0.3, 0.4 and 0.5) were prepared using $Cu(NO_3)_2$, (Sigma-Aldrich purity ≥ 99.99%) as a source for Cu ions and $Co(NO_3)_2$, (Sigma-Aldrich purity 99.9%) for Co ions dissolved in distilled water. TeO_2 (Sigma-Aldrich, purity ≥ 99%) was dissolved separately in aqueous NaOH solution till a clear solution is obtained. Both metal nitrates solution and TeO_2 solution were slowly mixed to obtain a precipitate of hydrated metal tellurate precursor. Complete precipitation was achieved using 2% NH_3 solution (pH = 7 - 8). This precipitate was then filtered, washed with distilled water and first dried in air, then in an oven at 200 °C for 3 h. It was homogenized and ground in an agate mortar and pestle to a fine size. Further, was finally calcined at 400

°C for 3 h and 600 °C for 5 h continuously in the air to produce a series of Co-doped copper tellurate.

Similarly, nickel doped copper tellurates were prepared with the concentration of Ni ranging from 0 to 0.5. In this case, the source for Ni was obtained from $Ni(NO_3)_2.6H_2O$ (Sigma-Aldrich, 99%) dissolved in distilled water along with copper nitrate salt. The rest of the procedure remained unchanged as mentioned above to produce $Cu_{3-x}Ni_xTeO_6$ series.

$Cu_{3-x}Zn_xTeO_6$ and $Cu_{3-x}Mn_xTeO_6$ compositions were obtained in a similar manner with - $Zn(NO_3)_2$ (Sigma-Aldrich, 99%) as a source for Zn ion and $Mn(NO_3)_2.4H_2O$ (Sigma Aldrich, 99%) as a source for Mn ion. Followed by this was the co-precipitation step as described above.

3.1.2 $Cu_3Te_{1-x}M_xO_6$ (M = W, Mo)

The synthesis process remains the same here. Two compositions (x = 0.1, 0.2), each of tungsten and molybdenum were synthesized using H_2WO_4 (Sigma-Aldrich, 99%) as a source of W and $(NH_4)_6Mo_7O_{24}$ (Sigma-Aldrich, 99.9%) as a source for Mo. For the synthesis of tungsten doped copper tellurate, stoichiometric amounts of $Cu(NO_3)_2$ was dissolved in distilled water whereas, H_2WO_4 was first dissolved in aqueous NaOH solution. To this, the stoichiometric proportion of TeO_2 was added and dissolved in it. This mixture was added drop-wise to the copper nitrate solution, which generated a precipitate, which was filtered, washed and dried in air. It was crushed to finer size with the help of agate mortar and pestle. Further, it was heated in an oven at 200 °C for 3 h and homogenized using mortar and pestle and was finally calcined at 400 °C for 3 h and 600 °C for 5 h continuously in the air.

3.1.3 $Cu_{2.9}M_{0.1}TeO_6$ (M = Fe, Eu and Ag)

Iron-doped copper tellurate with stoichiometry $Cu_{2.9}Fe_{0.1}TeO_6$ was prepared by a co-precipitation method using required quantities of $Cu(NO_3)_2$ and $Fe(NO_3)_3$ (Sigma –Aldrich, purity 99.9%) source for Cu and Fe ions respectively. NaOH dissolved TeO_2 was taken in stoichiometric amounts, which was then added to the metal salts solution, to obtain a precipitate. This precipitate was filtered washed with distilled water and dried in air. Further heat treatment was given as mentioned above.

Similarly, europium doped copper tellurate was produced as $Cu_{2.9}Eu_{0.1}TeO_6$. Eu_2O_3 (Sigma – Aldrich, 99.9%) was taken as a source for Eu. It was brought to the solution form by dissolving in dilute HNO_3. To this was added $Cu(NO_3)_2$ salt. TeO_2 dissolved in NaOH was slowly added to the metal ions solution. Complete precipitation was obtained with the help of 2% NH_3 solution. This precipitate was filtered, washed with distilled water and dried in air. Further heat treatment was given as mentioned in the synthesis of Co-doped copper tellurate.

Silver doped copper tellurate was prepared in a similar manner using, $AgNO_3$ (Sigma–Aldrich, > 99%) and $Cu(NO_3)_2$ as a source for silver and copper respectively.

3.1.4 $Ni_{3-x}M_xTeO_6$ (M = Co, Cu and Zn)

Pristine nickel tellurate along with a series of doped nickel tellurates was prepared by co-precipitation method. To prepare $Ni_{3-x}Co_xTeO_6$, $Co(NO_3)_2$ (Sigma – Aldrich, 99.9% purity) was used along with $Ni(NO_3)_2$ salt. NaOH dissolved TeO_2 was taken in stoichiometric amounts, which was then added to the metal salts solution, to obtain a precipitate. Using 2% NH_3 solution, until all the ions fully precipitated (pH=7-8). The obtained precipitate was then filtered, washed and first dried in air followed by an oven heating at 200 °C for 3 h. It was mixed thoroughly and ground in an agate mortar and pestle

to a fine size. Further, was finally calcined at 500 °C for 3 h and 750 °C for 5 h continuously in the air to produce a series of Co-doped nickel tellurate. For the preparation of $Ni_{3-x}Cu_xTeO_6$ and $Ni_{3-x}Zn_xTeO_6$, respective metal ion sources were taken. Rest of the procedure remained the same as above for co-precipitation synthesis.

3.1.5 $Ni_3Te_{1-x}M_xO_6$ (M = W, Mo)

The synthesis process here remained the same as that of $Cu_3Te_{1-x}M_xO_6$ (M=W, Mo). Two compositions (x=0.1, 0.2), each of tungsten and molybdenum were synthesized using H_2WO_4 (Sigma-Aldrich, 99%) and $(NH_4)_6Mo_7O_{24}$ (Sigma-Aldrich, 99.9%) respectively. For the synthesis of tungsten doped nickel tellurate, stoichiometric amounts of $Ni(NO_3)_2$ was dissolved in distilled water whereas, H_2WO_4 was first dissolved in aqueous NaOH solution. To this, the stoichiometric proportion of TeO_2 was added and dissolved in it. This mixture was added drop-wise to the nickel nitrate solution, which generated a precipitate, which was filtered, washed with distilled water and dried in air. It was crushed to finer size with the help of agate mortar and pestle. Further, it was heated in an oven at 200 °C for 3 h and homogenized using mortar and pestle and was finally calcined at 500 °C for 3 h and 750 °C for 5 h continuously in the air.

3.1.6 Fe_2TeO_6 and $Fe_{1.9}Eu_{0.1}TeO_6$

Here, we took $Fe(NO_3)_3$ (Sigma – Aldrich, 99.9% purity) as a source for Fe ion and dissolved it in distilled water. Separately, dissolved TeO_2 in aqueous NaOH and added this mixture drop wise to the metal salt solution. Generation of brown colored precipitate occurred. Complete precipitation was achieved using 2% NH_3 solution. The precipitate obtained was filtered and washed with distilled water. It was dried in air, then in an oven at 200 °C for 3 h. It was ground to fine size and then further heated at 500 °C for 3 h followed by 700 °C for 3 h.

For preparing $Fe_{1.9}Eu_{0.1}TeO_6$, Eu_2O_3 was first dissolved in dilute HNO_3 acid, to which was then added water dissolved $Fe(NO_3)_3$ salt. TeO_2 was separately dissolved in aqueous NaOH solution and was added dropwise to the metal ions solution. On obtaining the hydroxide precipitate, 2% NH_3 solution was added to ensure complete precipitation (pH = 7 - 8). The precipitate obtained was filtered and washed with distilled water. Finally, it was grounded and heat treatment was given as above.

3.1.7 Al_2TeO_6

Preparation of Al_2TeO_6 was slightly different from the rest of the tellurates and totally depended on the pH of the metal ion solution. It involved $Al(NO_3)_3$ (Sigma – Aldrich, 99.9% purity) dissolved in distilled water. pH of this was adjusted to ~1, using 2% dilute HNO_3 acid. TeO_2 dissolved in NaOH was added drop-wise to the above acidified solution, initiating precipitate formation. The pH of the solution was made to 7 - 8 using 2% NH_3. Formed precipitate was filtered and dried in air. In the next step, the dried precipitate was heated in an oven at 200 °C and then was grounded. It was further heated at 500 °C for 3 h and 750 °C for 5h continuously in the air to obtain Al_2TeO_6.

3.2 Sol-Gel Method

Using citric acid as a gelling agent, following series of compounds were prepared by sol-gel method

3.2.1 $Cu_{3-x}M_xTeO_6$ (M = Co, Ni, Zn and Mn)

$Cu_{3-x}Co_xTeO_6$, $Cu_{3-x}Ni_xTeO_6$ and $Cu_{3-x}Zn_xTeO_6$ series were prepared using $Co(NO_3)_2$ (Sigma – Aldrich, 99.9%), $Ni(NO_3)_2$ (Sigma – Aldrich, 99.9%) and $Zn(NO_3)_2$ (Sigma-Aldrich, 99.9%) respectively for dopant ions along with $Cu(NO_3)_2$ in distilled water. TeO_2

was dissolved in required amounts of dilute HNO_3 acid. Both dissolved TeO_2 and metal salt solutions were brought together and stirred well. To this mixture was added citric acid in the ratio, 2: 1 (citric acid: metal ions) to initiate gel formation. It was then heated for evaporation while stirring on a hot plate. On the formation of a viscous gel, it was transferred to a pre-heated oven at 200 °C for 3 h, for the decomposition to occur, which resulted in the formation of a foamy carbonaceous matter. This was ground and heated in a furnace at 400 °C to remove the organic matter and further sintered in a furnace at 600 °C to obtain the desired composition of metal tellurates.

3.3 Experimental characterization techniques under study

3.3.1 Thermal Analysis (TG-DTA/DSC)

Thermogravimetry (TG) is a thermal technique involving weight changes in a sample under a controlled temperature program. Changes in the mass of a sample are measured as a function of time and temperature and this helps us in studying various physical and chemical properties like decomposition, oxidation, reduction, sublimation, vaporization, absorption etc. This technique can be applied to inorganic as well as organic materials, polymers, plastics, paints, coatings etc. Various processes in TG are understood by the graphical representation of percent weight loss with temperature, which enables one to identify the phenomena taking place.

Differential thermal analysis (DTA) is a thermoanalytical technique in which both sample and the reference are kept under the same conditions i.e. same temperature (heating or cooling) and any temperature difference between them is recorded. Heat absorbed or evolved by the sample is detected relative to the inert reference. Hence, the plot of differential temperature (between the sample and reference) against the time or the temperature is plotted to understand various changes taking place in the sample under study. DTA can be used to

study thermal processes like fusion, crystallization, sublimation etc. In the present study, TG – DTA analysis are performed simultaneously on the prepared metal tellurate precursors on the instrument, NETZSCH TG-DTA STA 409PC, in an air atmosphere with a heating rate of 10 °C/min from room temperature to 800 °C.

Differential scanning calorimetry is an analytical technique which gives the measure of the enthalpy changes in a sample with respect to temperature or time. If the sample absorbs heat (endothermic) or gives out heat (exothermic), the energy required will accordingly be more or less to increase the temperature with the reference rate. The difference between the energy applied gives the energy utilized or liberated by the sample. Hence, the result of a DSC analysis is a curve of heat flux versus temperature or time. DSC measures the heat flow in materials and provides information about phase changes, such as amorphous and crystalline transitions, glass transition temperature and melting point as well as chemical changes. The data can be used to determine the specific heat capacity of materials and to describe the materials for their thermal behavior. Here, we have performed the analysis over Perkin Elmer DSC 8000 instrument, to study the heat effects associated with the transition under the influence of temperature [151].

3.3.2 Powder X-Ray Diffraction (XRD)

XRD is the most important characterization tool for identifying the purity and phase formation of a crystalline material without destructing the sample. It provides structural information like crystal type, lattice parameters, crystallite size etc of the material.

The incident monochromatic X-rays like Cu Kα or Mo Kα, interact with the material under study where the atoms present in the material scatter the X-ray incident on to them. The constructive interference of the scattered X-rays by atoms in an ordered lattice produces a diffraction pattern determined by the Bragg's law as follows:

$$n\lambda = 2dsin\theta$$

Where λ is the wavelength of the X-rays, d is the distance between the pairs of adjacent lattice planes, θ is the incident angle and n is the integer called order of reflection and normally taken as 1.

Graphical representation of the diffraction pattern obtained gives the intensity of the scattered radiation as a function of scattering angle 2θ. The maximum intensity peaks at specific angles help in estimating the spacing between the lattice planes, d, thus facilitating phase identification. Whereas, the width of the peaks helps in calculating the crystallite size using Scherer equation which can be expressed as:

$$D = \frac{n\lambda}{\beta cos\theta}$$

Where D is the crystallite size, n = shape factor with typical values for about 0.9, λ = X-ray wavelength, β = FWHM (full width at half maximum), θ is the Bragg's angle. The X-ray diffraction studies here were carried out on RIGAKU Ultima IV diffractometer using Cu-Kα radiations, λ=1.5418 Å, with Ni filter. The samples were scanned in 2θ ranging from 10 - 80 º in steps of 0.02 degree.

3.3.3 Infra-Red Spectroscopy (IR)

IR spectroscopy is a very useful technique in characterizing any material in terms of its purity and presence of functional moieties. It is a vibrational spectroscopy which enables vibrations of molecules at a certain frequency, characteristic of its structure. For any molecule to absorb IR radiation, the vibrations in the molecule should cause a change in its dipole moment. This is the most important criteria for a molecule to be IR active. When the IR radiation is allowed to pass through the sample, absorption will take place only when the

frequency of incident light matches the vibrational frequency of the molecule. Examining the transmitted light would reveal how much energy was absorbed.

Here, very trace amount of sample was mixed well with KBr, grounded in mortar and pestle and placed over sample holder. The vibrational spectrum was recorded from 400 - 4000 cm^{-1} to acquire information about the metal oxygen bond in the final sintered compounds and the precursor. IR spectra were recorded on SHIMADZU IR PRESTIGE-21 spectrophotometer.

3.3.4 UV-Visible Diffused Reflectance Spectroscopy (UV-DRS)

UV–DRS instrumental technique provides information about the material, by exciting the valence electrons to empty orbital on absorbing of UV–Visible light. For solid samples, light cannot pass through the sample, and thus it is reflected in different directions (diffuse reflection). In diffuse reflectance, one measures this relative change in the amount of reflected light off of a surface. Barium sulfate is used to run a baseline since white powder effectively reflects 100% of all visible wavelengths of light that interacts with it.

The energy levels that are separated by energy in the visible region absorb some of the light energy to move electrons from the filled energy level (valence band) into this empty level (conduction band). This causes a decrease in the amount of light at that particular energy, relative to a reference ($BaSO_4$). Which means % reflectance will also decrease. It is a nondestructive technique, very useful in obtaining the band gap of materials. Diffused reflectance spectra for all the samples were recorded on Shimadzu UV 2450 UV–Visible spectrophotometer in the wavelength range of 200 - 800 nm with BaSO4 as a reference. The optical band gap of the catalyst was determined using Tauc equation as given below:

$$\alpha h\nu = A\left(h\nu - E_g\right)^n$$

Where A = constant, α = absorption coefficient, h = Plank's constant, ν = frequency of vibration, n = 1/2 for direct bandgap semiconductor and Eg is the optical band gap. The graphs of $(\alpha h\nu)_2$ v/s photon energy (hν) in eV were plotted for the samples. The point of intersection on the x-axis (hν) obtained by extrapolating the linear section of a plot where $(\alpha h\nu)_2$ is on the y-axis, gives the optical band gap value (Eg).

3.3.4 X-Ray Photoelectron Spectroscopy (XPS)

XPS is the most powerful characterization technique for identifying the valence state of elements present in a material and chemical analysis of materials. It makes use of photo-ionization and energy-dispersive analysis of the emitted photoelectrons to study the composition and electronic state of the surface region of a sample. In XPS the photon is absorbed by an atom in a molecule or solid, leading to ionization and the emission of a core (inner shell) electron. The kinetic energies of the emitted photoelectrons E_K, is measured by electron spectrometer and since the emitted electrons' kinetic energies are known, the electron binding energy of each of the emitted electrons can be determined by using an equation that is based on the conservation of energy:

$$E_B = h\nu - E_K - \Phi$$

Where E_B is the binding energy (BE) of the electron which is the characteristic of the orbital of the ejected photoelectron, $h\nu$ is the energy of the X-ray photons being used, E_K is the kinetic energy of the electron as measured by the instrument and Φ is the work function dependent on both the spectrometer and the material. This equation is essentially a conservation of energy equation.

Here, the prepared materials were characterized using the instrument PHI VERSA PROBE II with Mg-Kα as the X-ray source. First, a full scan or survey scan is recorded over a wide binding range, allowing the identification of elements present. Then a high-

resolution spectrum for the required element is obtained in their respective binding energy range, enabling us to plot a graph of intensity versus binding energy (eV).

3.3.5 Scanning Electron Microscopy-Energy Dispersive Spectroscopy (SEM-EDS)

Material's morphological characteristics are best understood with the help of SEM technique. It provides us with an image of the particle arrangement, its size, shape etc. The basic principle involves, hitting the atoms by an electron beam, producing various signals which are collected to give information about the surface features.

EDS analysis was carried out on prepared samples to understand the elemental composition present. SEM-EDS analysis was carried out on Carl Zeiss EVO 18 instrument. It involves a beam of X-rays, incident onto the sample which may elevate an electron to an excited state. The arrival of the electron to the ground state results in characteristic x-ray emission. These x-rays are then detected and utilized to give useful information about the constituent elements present in the compound.

3.3.6 Transmission Electron Microscopy (TEM)

In material science, TEM plays an important part in determining the particle form, shape, size, intentionally created defects, surface layers or impurities, dislocations, grain boundaries etc. allowing visuals at the atomic scale and offering high resolution.

The beam of electrons strikes the specimen and parts of it are transmitted depending upon the thickness and electron transparency of the specimen. This transmitted segment is focused into an image on a phosphor screen or charge coupled device (CCD) camera wherein the stroked image generates light to make it visible. When more electrons get transmitted

through, the image carries lighter areas whereas the darker areas of the image signify those areas of the sample that fewer electrons are transmitted through. In the present study, TEM images were generated using the instrument Philips CM 200.

3.3.7 DC (Direct Current) Electrical Resistivity

Electrical resistivity measurements are carried out by measuring the current through a sample at a fixed voltage, which on substituting in the relation below gives resistance and thus, resistivity:

$$R = \rho \frac{L}{A}$$

R = Resistance

ρ = Resistivity

A = cross-sectional area of the pellet

L = thickness of the pellet

Graphical representation of the study involves a plot of log ρ verses 1000/T, which enables us to identify the material behavior as conductor, insulator or semiconductor under the influence of temperature. If the sample shows an increase in resistivity with an increase in temperature, it is said to behave like a semiconductor. If it shows a decrease in ρ with an increase in temperature, it behaves like a conductor since, at a higher temperature, the motion of electrons gets lowered due to thermal collisions. It is a very useful technique in the fields of material science for the study of semiconductors, insulator materials.

The sample in the form of a pellet is used which is prepared by pressing the powdered compound in a hydraulic press at a pressure of 3 ton. This pellet is sintered first before using

at high temperature to attain good strength. This is then placed in a two probe conductivity cell and the studies were carried out from room temperature to 450 °C in air. At a constant voltage of 2 volts, current alterations were obtained with increasing temperature.

3.3.8 Vibrating Sample Magnetometer (VSM)

VSM is a highly sophisticated, versatile, highly accurate instrument which enables the study of various magnetic properties of a material under study. VSM measures the magnetization of a small sample of magnetic material placed in an external magnetic field by converting the dipole field of the sample into an AC electrical signal. A sample to be studied is placed in a brass holder at the bottom of the sample rod inside the uniform magnetic field and then vibrated sinusoidally using vibrator made of linear actuators or modified audio speakers. This induces a voltage in the pickup coil which is measured through the lock-in amplifier using the piezoelectric signal as its reference signal. Lock-in measurement enables the measurement of the signal weaker than the noise. By measuring in the field of an external electromagnet, it is possible to obtain the results of a material study.

The magnetic properties presented for this work were performed using QUANTUM DESIGN PPMS VSM instrument. The magnetization with the varying magnetic field (up to 3 Tesla i.e. 30000 Oe) was measured at 50 K and 300 K (M-H). The plots of magnetization (emu/g) versus field (Oe) represent the magnetic property of samples. The magnetization with varying temperature (M-T) was also studied at the applied constant magnetic field. The plots of magnetization (emu/g) versus temperature (K) are presented here.

3.3.9 Thermoelectric Power (TEP)

The thermoelectric power (TEP) also known as Seebeck coefficient of a material is a measure of the magnitude of an induced thermoelectric voltage in response to a temperature difference across that material. Thermoelectric power is an important tool to study various intrinsic properties of bulk samples as a sign of the dominant charge carriers as well as the carrier concentrations [152]. The highly efficient behavior of thermoelectric generators and thermoelectric coolers is based on the use of materials with high Seebeck coefficient [153][154].

Physically, the magnitude and sign of the Seebeck coefficient can be approximately understood as being given by the entropy per unit charge carried by electrical currents in the material. It may be positive or negative. In conductors that can be understood in terms of independently moving, nearly-free charge carriers, the Seebeck coefficient is negative for negatively charged carriers (such as electrons) and positive for positively charged carriers (such as electron holes).

Thermoelectric power measurements were carried out in order to measure the conduction phenomena on the prepared samples, which displayed semiconductor behavior at a higher temperature. Thermoelectric power or Seebeck coefficient (α) is given by, $\alpha = \Delta V/\Delta T$, where ΔV is the voltage developed across the sample and ΔT is the temperature difference across the sample and the sign of this α represents the type of charge carriers responsible for electronic transport in semiconductors [151,155–160]. The sample in the form of a pellet is placed in a two probe TEP measurement set up.

3.3.10 Inductively coupled plasma atomic emission spectroscopy (ICP-AES)

ICP-AES is an analytical technique, used in the quantitative estimation of elements present in the sample. It is also used for the analysis of trace elements in a sample. In the present study, the analysis is carried out on ARCOS, Simultaneous ICP Spectrometer. It is a type of emission spectroscopy that uses the inductively coupled plasma to produce excited atoms and ions that emit electromagnetic radiation at wavelengths characteristic of a particular element. It is a flame technique with a flame temperature in a range from 6000 to 10000 K. The intensity of this emission is indicative of the concentration of the element within the sample.

3.3.11 Dielectric Study

The Dielectric (DE) analysis is an important study, which can be used to gain the knowledge with respect to the electrical properties of a material medium as a function of temperature and frequency. The relative dielectric constant (ε_r) evaluates the maximum energy that can be stored in the material whereas tan δ determines, how well a material can absorb the electromagnetic field [161]. Dielectric constant, as well as dielectric loss, depends strongly on the frequency.

The dielectric material increases the storage capacity of the capacitor by neutralizing the charges at the electrodes. If an AC source of voltage is placed across the capacitor containing dielectric material, the resulting current is obtained due to charging and loss. The interaction of the material with an electric field is described as permittivity.

In this thesis, the dielectric measurements were made using the sample in the form of the pellet on the instrument Wayne Kerr 6500P LCR meter in a frequency range of 20 Hz to 10 MHz and temperature up to 600 °C.

Assuming the capacitance of a parallel plate capacitor, the dielectric constant is given by:

$$\varepsilon = \frac{Cd}{A\varepsilon_{\circ}}$$

Where, C = Capacitance of the material in Farad

d = thickness of the pellet in meters

A = cross-sectional area of the pellet in m^2

ε_o = permittivity of free space, 8.854×10^{-12} F/m.

3.3.12 Photoluminescence Study (PL)

Photoluminescence is a very useful optical, nondestructive technique for studying the optical properties of the material. It gives information about material quality, band gap, impurity and defect detection etc. In a typical analysis, the light energy source is irradiated onto a sample with energy greater than the band gap energy of that material, where it is absorbed and a process called photo-excitation occurs. The photo-excitation causes the material to jump to a higher electronic state while releasing energy (photons) as it relaxes and returns to back to a lower energy level. The emission of light or luminescence by this process is called photoluminescence.

Here, photoluminescence studied were carried out on JOBIN YVON FLUROLOG-3-11 SPECTROFLUOROMETER with xenon lamp source to measure the excitation-emission spectra.

3.4 Photo-catalytic activity

Degradation of organic pollutants like dyes, certain emulsions etc is a major problem faced by many of the industrialists as the harmful intermediates obtained while producing various products lead to hazard issues to the environment. Methylene blue is one such toxic dye which is used tremendously in industries producing cloth dyeing, paper and leather and textile industry. Hence, its disposal is a real concern. Photo-catalytic processes are among the most studied methods in solving such problems related to pollution.

In this process, light photon generates electron-hole pair on exposing the semiconductor. On exposure to solar radiation, the semiconductor will get excited to give the excited state. This excited state will provide an electron to the conduction band leaving behind a hole in the valence band. This electron is then trapped by molecular O_2, forming O_2^- ion. The valence band hole generates hydroxyl radical from hydroxyl ions, which can easily attack the adsorbed dye.

In this work, a solution of methylene blue was prepared with the concentration of 10 ppm. 50 ml of this was taken into three separate conical flasks. 0.1g of the catalyst was added to all the flasks, it was swirled, corked and kept in sun. The first, second, third, flasks were removed at an interval of one, two, three hours respectively. The solution was filtered using an ordinary filter paper and then their absorption was measured in the UV-VIS spectrophotometer. A graph of absorption versus time was plotted.

3.5 Partial propylene oxidation

Partial oxidation of propylene to acrolein was studied over a few selected catalysts using a fixed bed glass reactor. All the reaction parameters like temperature, the flow of gases etc were kept under control and the reactor was placed in an electrically heated furnace for uniform heating of the catalyst bed. Propylene, oxygen, and nitrogen were fed into the reactor. Outlet gases were analyzed using an online NUCON 5765 gas chromatograph, equipped with a flame ionization detector.

3.6 Antibacterial Study

Antibacterial studies were tested against two different emerging opportunistic bacterial pathogens namely Gram-negative *Escherichia coli* and Gram-positive *Staphylococcus aureus* by agar well diffusion method for selected metal tellurates (Heatley, 1994). A stock solution of (20 mg/ml) of all the four compounds was prepared in DMSO separately and used for the assay. The overnight grown pathogens were platted on nutrient agar. Sterile cork borer (6 mm) was used to bore wells and different concentrations of nanoparticle suspension were loaded on to the wells. The plates were incubated at 37 °C, 24 h and were checked for the zone of inhibition around the colony which is the measure of antibacterial activity.

Chapter 4

Characterization and Spectroscopic studies

Characterization is a very important step when dealing with the material study as it enables a better understanding of the compound and the authenticity of the compound in its raw as well as final form. Characterization techniques such as TG-DTA, XRD, IR, UV-VIS DRS, SEM-EDX, TEM and XPS were employed.

4.1 Thermal Analysis (TG-DTA/DSC)

The precursors of the compounds prepared by co-precipitation and sol-gel methods were studied using TG – DTA techniques.

4.1.1 Pristine Cu_3TeO_6 and $Cu_{2.9}Co_{0.1}TeO_6$ *(by co-precipitation method)*

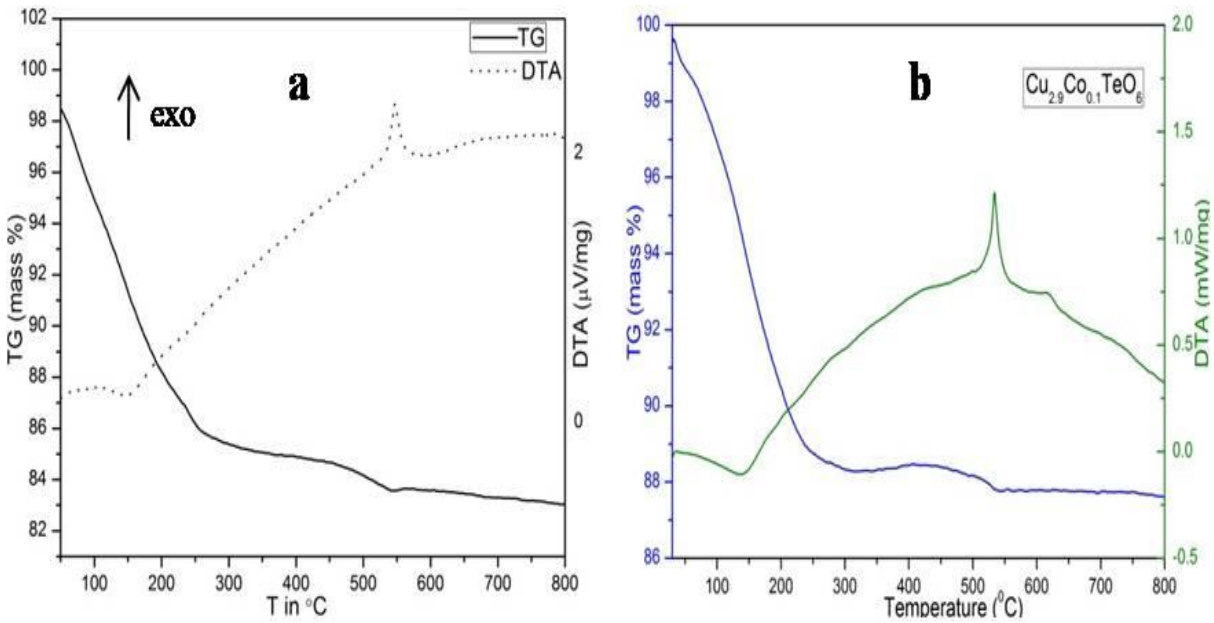

Fig. 4.1 TG–DTA curves of precursors of (a) pristine Cu_3TeO_6 and (b) $Cu_{2.9}Co_{0.1}TeO_6$.

Metal tellurate precursors were obtained on filtering the precipitate and drying them in the air. These precursor compounds were subjected to heating from 30 °C to 800 °C at a rate of 10 °C / min in air. Above Fig. 4.1 shows various thermal processes taking place in the precursor of pure Cu_3TeO_6 (a) and cobalt doped copper tellurate (b). As seen in the TG curve, initial weight loss of nearly 10% is observed up to 250 °C which could be attributed to the

loss of water molecules present in the precursor. According to A. C. Roberts et al., a molecule of water is almost completely structurally attached within the Cu_3TeO_6 framework [162]. DTA curve also shows an endothermic peak at the around same temperature. As the temperature is raised further, a slight kink is observed in the TG curve at around 550 °C with a corresponding exothermic peak in the DTA curve at the same temperature. This could be due to the conversion of amorphous form to crystalline form at that particular temperature. Heating beyond this temperature does not lead to any weight loss.

4.1.2 $Cu_{2.7}Ni_{0.3}TeO_6$ *(by co-precipitation method)*

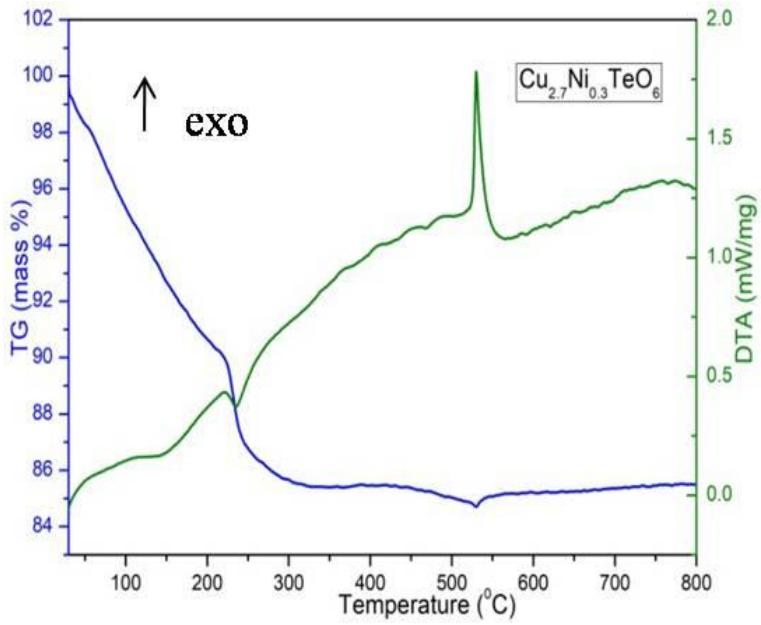

Fig. 4.2 TG–DTA curves of $Cu_{2.7}Ni_{0.3}TeO_6$ precursor.

Figure 4.2 shows TG–DTA analysis on the precursor of $Cu_{2.7}Ni_{0.3}TeO_6$ synthesized via co-precipitation depicting similar behaviour as seen in Fig. 4.1. An endotherm in the DTA curve is observed at ~250 °C with corresponding weight loss in the TG curve. This is because of the water present in the precursor which is lost on heating. The loss of adsorbed moisture / water takes place first followed by the loss of lattice water. As mentioned before, copper tellurate structure holds a molecule of water within itself [162]. It can be seen from Fig. 4.2

that the TG curve reveal two step weight loss process from 30–250 °C with respective kinks in DTA. Thus, this could be considered for the loss of physisorbed water and structural water. At around 550 °C, DTA shows a sharp exothermic peak indicating conversion of amorphous to crystalline phase with no weight loss further in TG curve.

4.1.3 $Cu_{2.9}Zn_{0.1}TeO_6$ *(by co-precipitation method)*

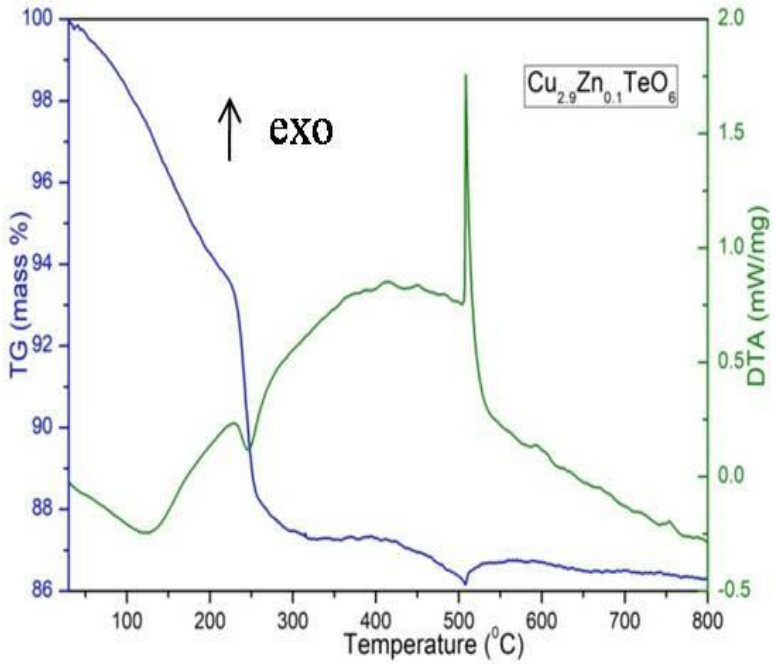

Fig. 4.3 TG–DTA curves of $Cu_{2.9}Zn_{0.1}TeO_6$ precursor.

Series of zinc doped copper tellurates prepared by co-precipitation method were studied using TG–DTA analysis and the results are displayed in Fig. 4.3. Initially, there is weight loss up to 200 °C due to loss of water, followed by loss of lattice water around 250 °C which is indicated by a kink in DTA curve. The crystallization starting point is indicated by a sharp peak in the DTA curve at around 550 °C with a slight shakeup a point in TG. This probably could be due to the effects from DTA analyses that cause TG to produce an annoyance. There is no weight loss observed further on heating up to 800 °C.

4.1.4 Ni_3TeO_6 *(by co-precipitation method)*

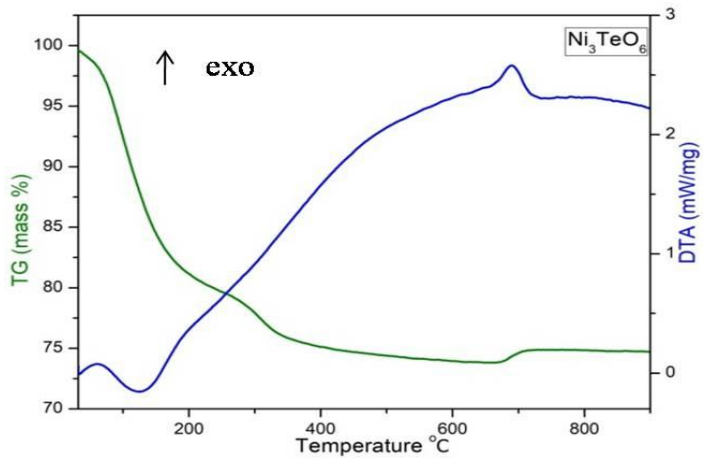

Fig. 4.4 TG–DTA curves of Ni_3TeO_6 precursor.

Temperature-dependent thermal behaviours of the Ni_3TeO_6 precursor is shown in Fig. 4.4. The TG curve for precursor shows a loss in weight up to 350 °C due to the loss of water, with the corresponding endotherm in DTA. Further, there is an exothermic peak observed at around 700 °C in DTA suggesting the conversion of glassy amorphous phase to crystalline phase for Ni_3TeO_6 occuring at a higher temperature.

4.1.5 Fe_2TeO_6 and Al_2TeO_6 *(by co-precipitation method)*

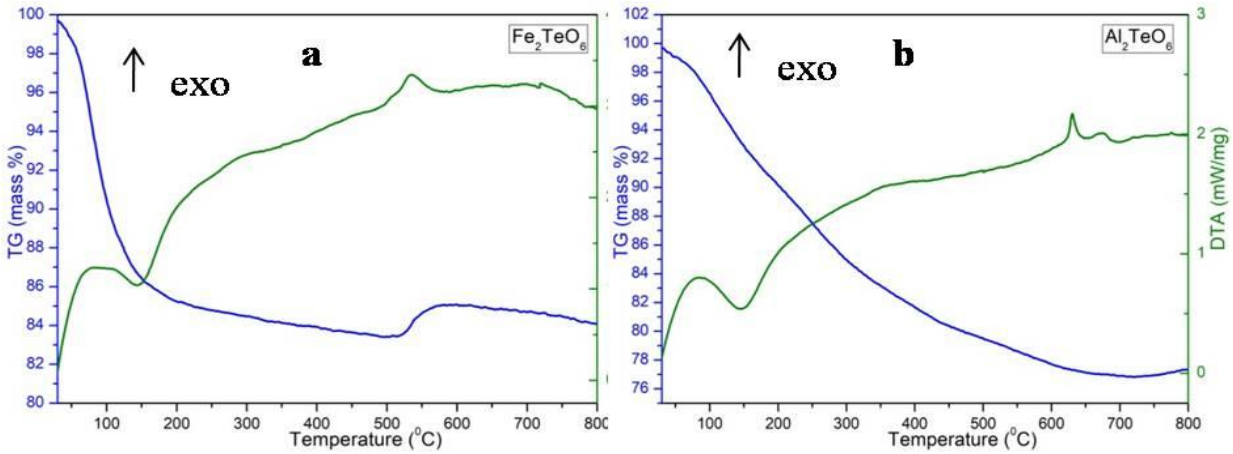

Fig. 4.5 TG–DTA curves of precursors of (a) Fe_2TeO_6 and (b) Al_2TeO_6.

The above Figure 4.5 presents TG–DTA analysis of Fe_2TeO_6 and Al_2TeO_6 precursor. Initial weight loss in both the cases is due to loss of physisorbed water. The commencement of crystallization is found to vary slightly with composition. For a Fe_2TeO_6 precursor, it appears at around 550 °C whereas for Al_2TeO_6 it arises at a higher temperature at around 650 °C. These compounds show thermal stability beyond their phase conversion point and can be well sintered above this.

4.1.6 Doped and pristine Cu_3TeO_6 *(by sol-gel method)*

Cobalt-doped copper tellurate compounds were prepared using sol-gel method and their precursors were obtained in the form of a viscous gel prior to decomposition. This gel precursor was studied for simultaneous TG–DTA analysis at a heating rate of 10 °C per minute in the air up to 800 °C. As shown in Fig. 4.6 (a and b), the hydrated gel loses water from 30 °C – 190 °C, thus showing loss in weight in TG curve. There also appears a endotherm in DTA, signifying loss of water. On further heating, the gel up to ~ 350 °C, the organic components from the compound are decomposed showing a sudden drop in weight in TG which is accompanied by exothermic peaks in the DTA curve. Beyond 350 °C, there is gain in weight observed in TG with corresponding sharp exothermic peak in DTA. This could probably be due to the oxidation of Cu and Te to form the oxide.

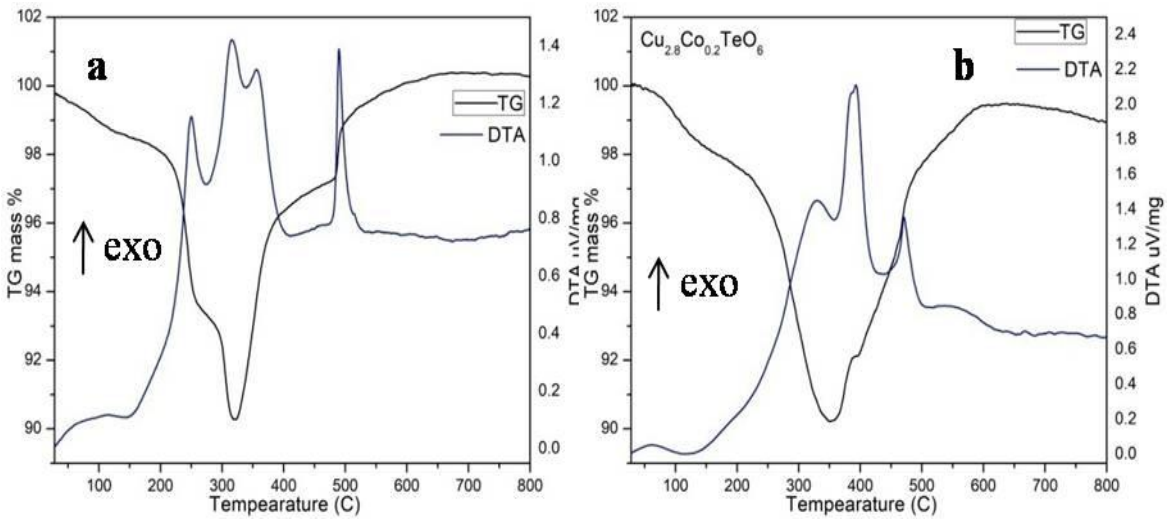

Fig. 4.6 TG–DTA curves of (a) Cu_3TeO_6 and (b) $Cu_{2.8}Co_{0.2}TeO_6$ precursors.

4.2 X-ray diffraction technique (XRD)

4.2.1 Pristine and cobalt doped Cu_3TeO_6 *(by co-precipitation method)*

X-ray diffraction studies on $Cu_{3-x}Co_xTeO_6$ (x = 0.1, 0.3, 0.5) tellurates are presented in Fig. 4.7 (a). All the peaks are assigned to the cubic system with space group *Ia*3 [92] and reveal the monophasic formation of pristine and doped compounds with peaks corresponding to the Cu_3TeO_6 (JCPDS card # 22-0251). Fig. 4.7 (b) shows temperature initiated phase conversion from amorphous to crystalline. Crystallite size is obtained using Scherrer's formula and is presented in Table 4.1 showing reduction in size with doping.

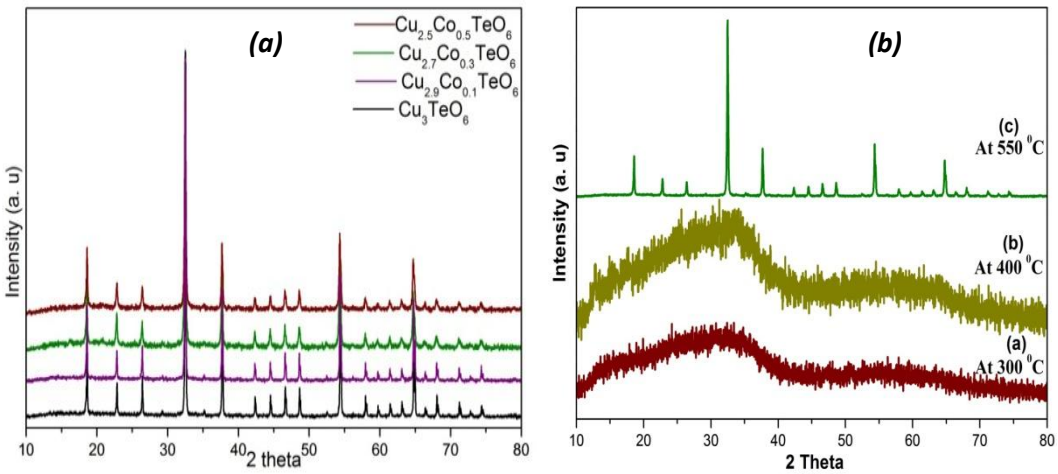

Fig. 4.7 XRD pattern of (a) Pristine and Co doped Cu_3TeO_6 and (b) temperature dependent phase conversion process.

Table 4.1 Calculated Scherer's crystallite size of $Cu_{3-x}Co_xTeO_6$ (x = 0, 0.1, 0.3 and 0.5) samples showing sizes smaller in doped compounds than in pristine.

Sample	Average crystallite size in nm
Cu_3TeO_6	54
$Cu_{2.9}Co_{0.1}TeO_6$	54
$Cu_{2.7}Co_{0.3}TeO_6$	39
$Cu_{2.5}Co_{0.5}TeO_6$	40

4.2.2 Pristine and nickel doped Cu_3TeO_6

Fig. 4.8 represents the X-ray diffractogram of pure and nickel doped copper tellurate compounds. All the doped compounds are observed to show XRD patterns matching the cubic crystal system of Cu_3TeO_6 (JCPDS card # 22-0251), without any extra / impurity peak. This shows that compounds formed are monophasic in nature.

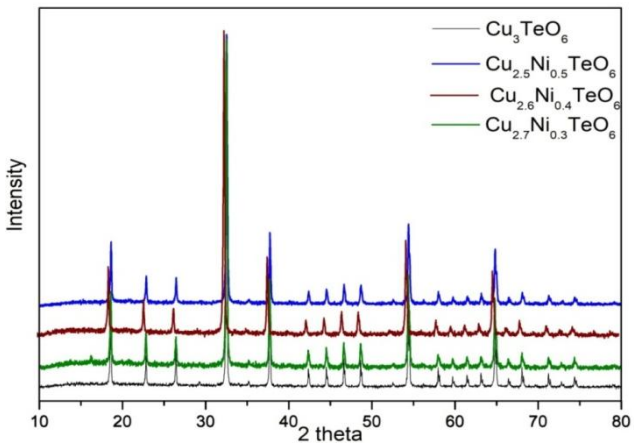

Fig. 4.8 XRD pattern of Cu_3TeO_6 and Ni-doped Cu_3TeO_6.

4.2.3 Zinc doped Cu_3TeO_6 and manganese doped Cu_3TeO_6

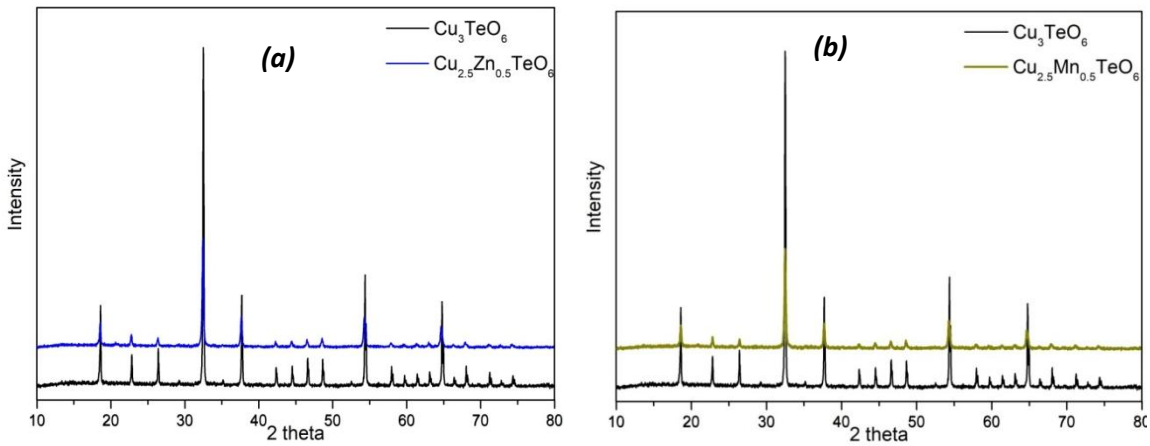

Fig. 4.9 XRD pattern of (a) Zn doped Cu_3TeO_6 and (b) Mn doped Cu_3TeO_6.

Fig. 4.9 presents the XRD patterns of zinc doped copper tellurates and manganese doped copper tellurate. The data was recorded from 10 - 80° range at room temperature with Cu Kα source of radiation. The powder pattern is found to match the reported card (JCPDS card # 22-0251) with no traces of secondary phase which signifies the formation of the cubic phase.

4.2.4 Tungsten doped Cu_3TeO_6 and molybdenum doped Cu_3TeO_6

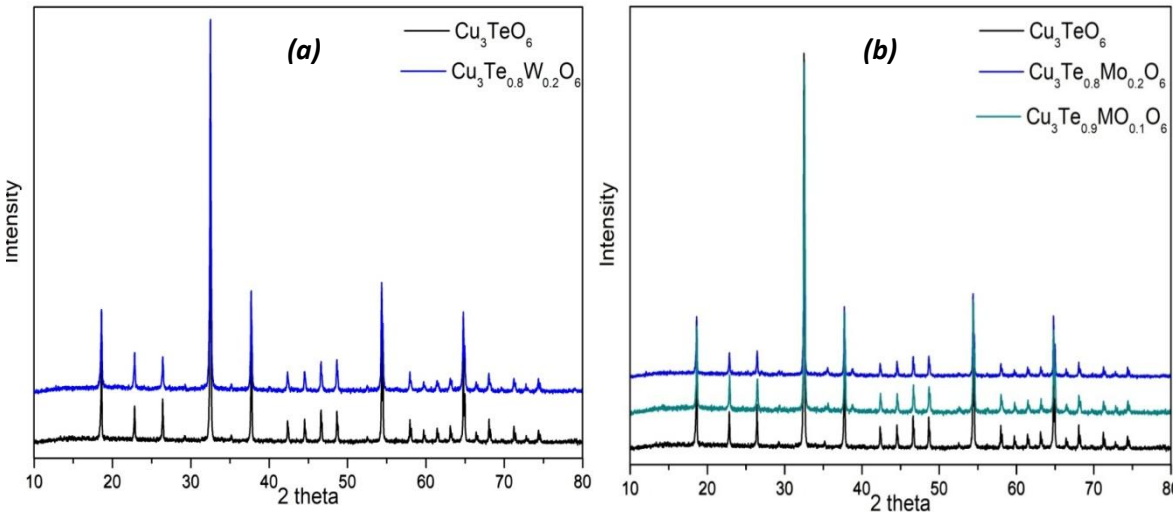

Fig. 4.10 XRD pattern of (a) W doped Cu_3TeO_6 and (b) Mo doped Cu_3TeO_6.

XRD patterns for tungsten and molybdenum doped Cu_3TeO_6 compounds are shown in Fig. 4.10 (a) and (b) which appraise the structural information of the compounds. All the peaks are assigned to the cubic structure of copper tellurate with space group *Ia*3, without any other impurity peak. This could also tell that tungsten and molybdenum could substitute tellurium in not more than 2% which would otherwise lead to impurity peak in the powder diffraction pattern.

4.2.5 Pristine and doped $Cu_{2.9}M_{0.1}TeO_6$ (M=Ag, Fe, Eu)

Fig. 4.11 presents XRD patterns of pristine and Ag, Fe and Eu doped copper tellurates with cubic phase, justified by all the peaks lying in the region 10 – 80° without any extra peak. These peaks match well with the reported data with the space group P42/mnm. The patterns obtained are clearly monophasic without any impurity.

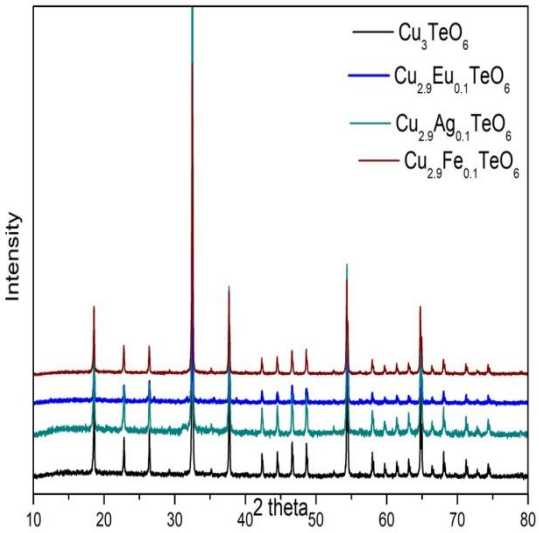

Fig. 4.11 XRD pattern of Ag-doped Cu_3TeO_6, Eu doped Cu_3TeO_6 and Fe doped Cu_3TeO_6.

4.2.6 Pristine and doped Ni_3TeO_6

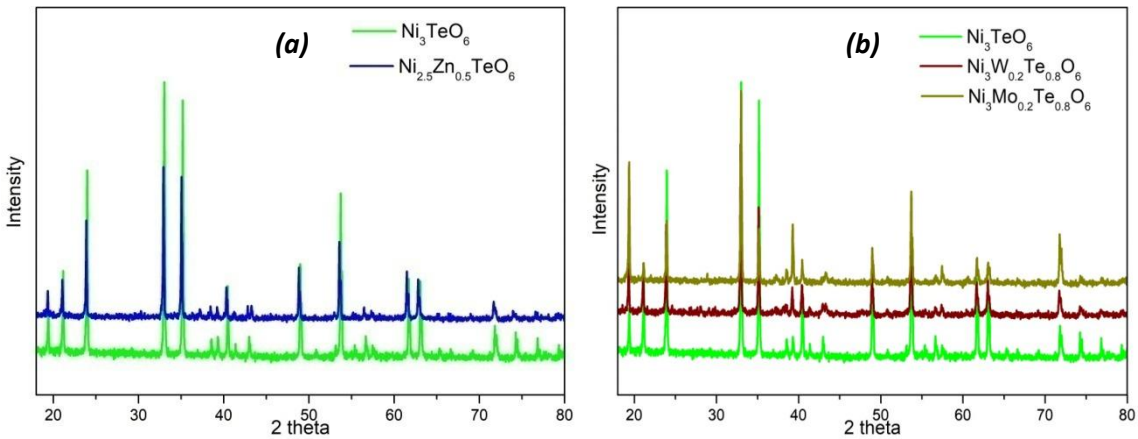

Fig. 4.12 XRD pattern of (a) Zn doped Ni_3TeO_6 and (b) W and Mo-doped Ni_3TeO_6.

Phase and structure identification of pure and doped nickel tellurate samples was carried out using X-ray powder diffraction and the results obtained are shown in Fig. 4.12 (a) and (b). All the peaks obtained from the diffraction pattern were indexed to the rhombohedral structure corresponding to the reported data (JCPDS card # 20-0794) with space group *R3*.

4.2.7 Pristine and doped Fe_2TeO_6 and pristine Al_2TeO_6

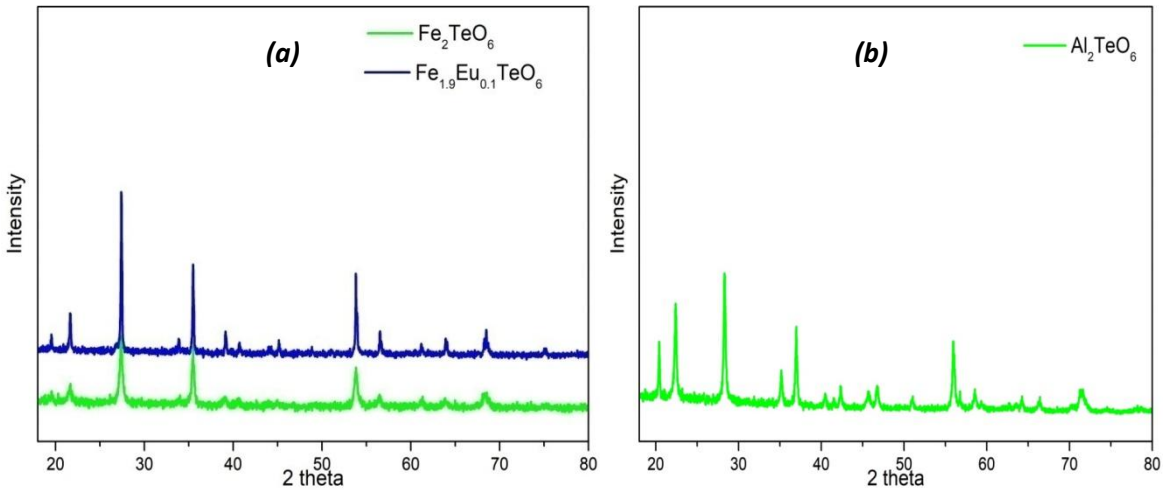

Fig. 4.13 XRD pattern of (a) pristine and doped Fe_2TeO_6 and (b) Pristine Al_2TeO_6.

Fig. 4.13 (a) presents X-ray diffraction patterns of pristine and doped iron tellurates with tetragonal phase, justified by all the peaks lying in the region 10 – 80° without any extra peak. These peaks match well with the reported data (JCPDS card # 15-0686) and the space group possessed is *P42/mnm*. Diffraction pattern for pristine aluminium tellurate prepared by co-precipitation method has been shown in Fig 4.13 (b). The 2 theta peaks in the compound are assigned to the tetragonal phase with space group same as that of Fe_2TeO_6 that is *P42/mnm*. The pattern obtained is clearly monophasic without any impurity.

By sol-gel method

4.2.8 Pristine and doped Cu_3TeO_6

Compounds of tellurium prepared via sol-gel route provided clear, the monophasic formation of copper tellurate and doped copper tellurates as shown in Fig. 4.14. The highest dopant concentration of prepared tellurates is presented which are found to match the

reported data (JCPDS card # 22-0251) for the cubic structure of copper tellurate with space group *Ia3*.

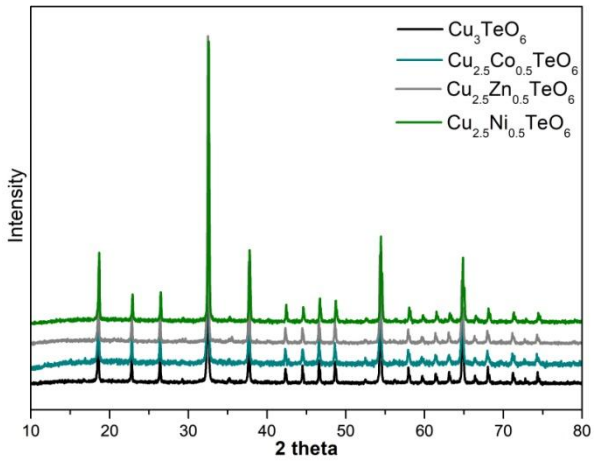

Fig. 4.14 XRD pattern of Cu_3TeO_6 and doped Cu_3TeO_6 by sol-gel method.

4.3 Infrared spectroscopy

4.3.1. Pristine and cobalt doped Cu_3TeO_6 *by co-precipitation method*

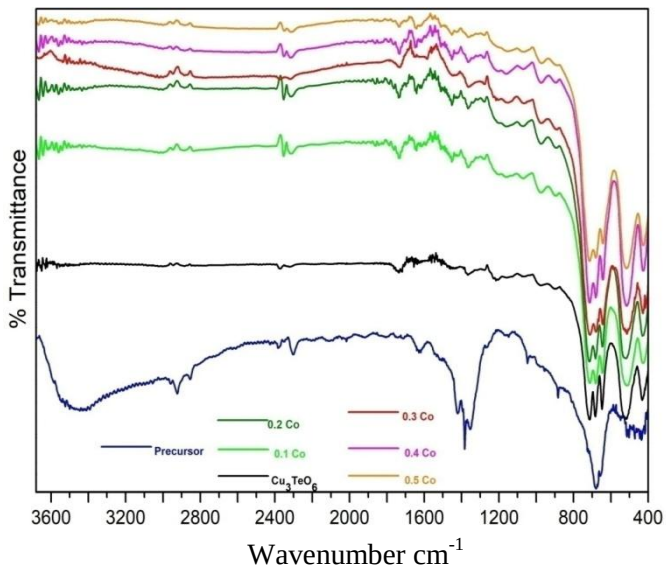

Fig. 4.15 IR spectra of pristine and Co-doped Cu_3TeO_6 precursor and oxide.

IR spectra of pure Cu_3TeO_6 and cobalt doped hydrated precursors and final oxides prepared by co-precipitation method are shown in Fig. 4.15. The hydrated precursor shows the presence of water and nitrate moieties around 2800 – 3600 cm^{-1} and 1200 – 1600 cm^{-1}

respectively. The final oxides are without all these impurities and possess stretching vibrations in the region 400 – 800 cm^{-1} due to metal – oxygen bonds which lies between 400 – 550 cm^{-1} for Te^{6+}-O and 700 – 800 cm^{-1} for M–O [89,163,164].

4.3.2. Pristine and nickel doped Cu_3TeO_6 *by co-precipitation method*

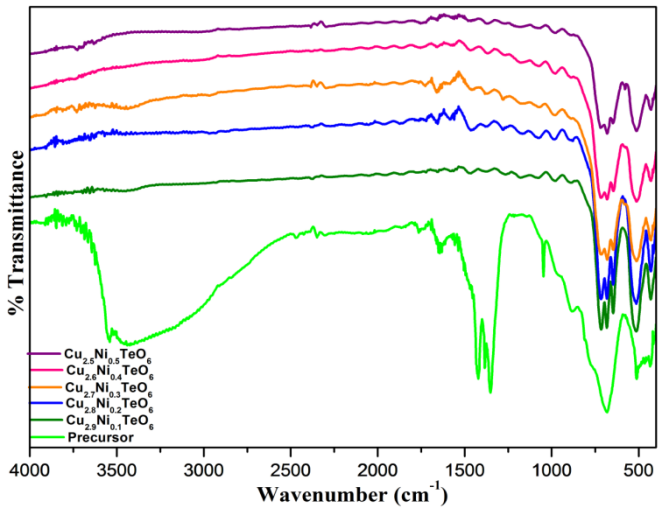

Fig. 4.16 IR spectra of Ni-doped Cu_3TeO_6 precursor and oxide.

Fig. 4.16 represents infrared spectra for hydrated precursor and final metal tellurate oxides. In precursor spectrum, a broad band is observed due to the presence of water molecules in the IR region from 2800 – 3600 cm^{-1} and a prominent peak in between 1300 - 1400 cm^{-1} could be assigned for the presence of nitrate moieties [165]. All these peaks for vibrations of the precursor are observed to vanish on heating to form oxides. Hence, final metal oxides obtained show only M–O vibrations without any other impurity.

4.3.3. Zinc and Manganese doped Cu_3TeO_6 *by co-precipitation method*

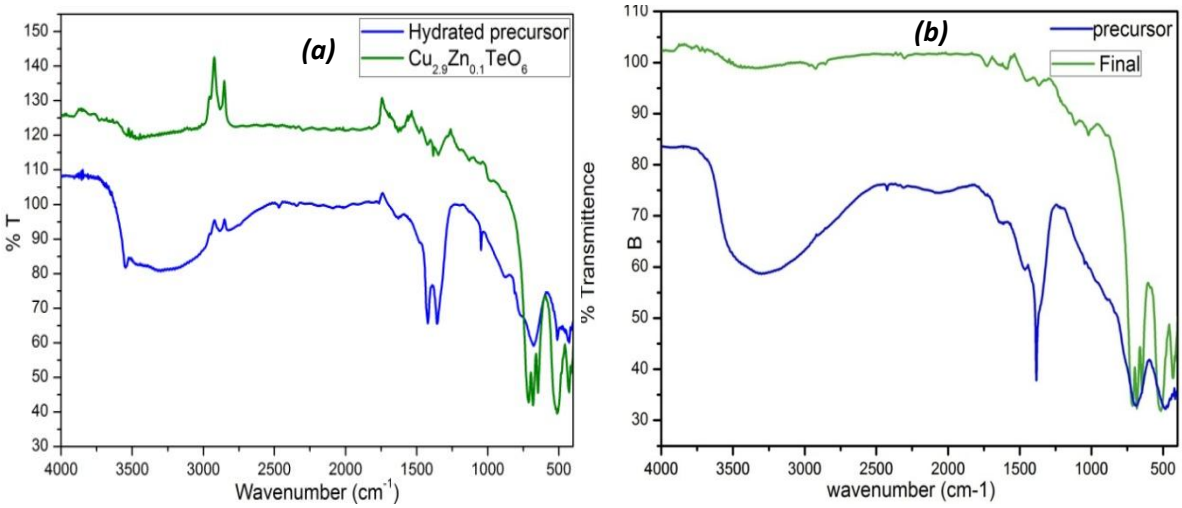

Fig. 4.17 IR spectra of (a) Zn-doped Cu_3TeO_6 and (b) Mn-doped Cu_3TeO_6 precursor and oxide.

IR spectrum for zinc doped copper tellurate and Mn-doped copper tellurate is presented in the above Fig. 4.17 (a) and Fig. 4.17 (b) respectively for pristine and final oxide. It is found to show similar results to that of the above-mentioned compounds. Precursor shows the presence of water and nitrate moieties which appear to be completely absent in the final oxides showing their clear patterns without any impurities. The final oxides show the appearance of only M–O stretching vibration bands in the region from 400 – 800 cm^{-1}. This suggests the qualitative formation of metal tellurates.

4.3.4. Pristine and cobalt doped Cu_3TeO_6 *by sol-gel method*

Infrared spectra of the gel and calcined sample for cobalt doped copper tellurate compounds prepared by sol-gel technique are presented in Fig. 18. All the existing spectra for precursor shows the presence of various organic functionalities like O–H, carboxylic, nitrates from the complexing agents i.e. citric acid. The stretching and bending vibrations for O–H are seen at around 3150 cm^{-1} and 1630 cm^{-1} respectively along with C=O at around 1700 cm^{-1}

representing free carbonyl stretching. A prominent peak at 1388 cm^{-1} could be assigned to nitrate moieties. All these features revealed that the gel was hydrated one which on further heating led complexation to occur, which on further decomposition gave a pure form of desired metal tellurate compounds as seen in the spectra for final metal oxides. Final metal oxides show no other vibrations than metal oxygen stretching vibrations, which mark their qualitative formation on decomposition. All the M–O vibration bands are found to appear in the region in between 400 – 800 cm^{-1}.

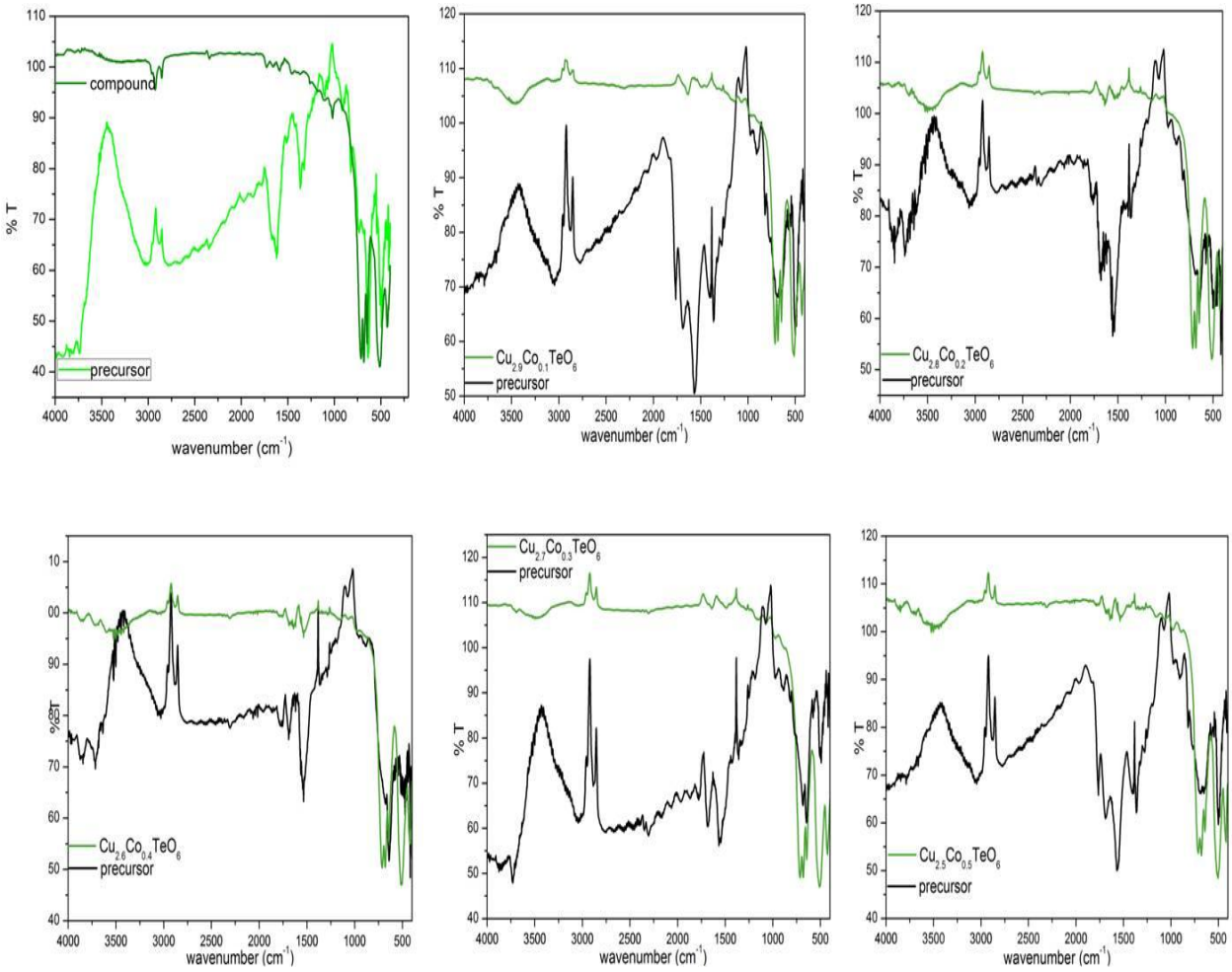

Fig. 4.18 IR spectra of pristine and Co-doped Cu_3TeO_6 precursor and oxide.

4.4 UV-Visible Diffused Reflectance Spectroscopy.

The diffuse reflectance spectroscopy (DRS) for all the samples were recorded in the range 200 to 800 nm and the % reflectance was measured against the wavelength. The plots were converted to absorbance using Kubelka Munk function and were plotted against the wavelength. Using the absorbance values, Tauc plots were generated which gave optical band gap.

4.4.1 Pristine Cu_3TeO_6 and cobalt doped Cu_3TeO_6

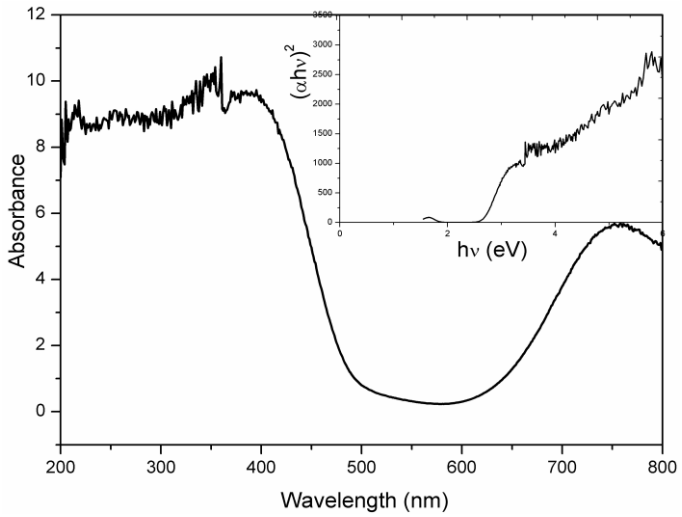

Fig. 4.19 UV-DRS spectra of pristine Cu_3TeO_6 with Tauc plot in the inset.

Diffused reflectance spectroscopic study was carried out on pristine and cobalt doped copper tellurates. The absorption v/s wavelength spectra for pristine and cobalt doped copper tellurate is shown in Fig. 4.19 Fig. 4.20. The absorption takes place in between 200 – 400 nm region and is found to increase in width and intensity on doping with cobalt. These absorbance values were then used to generate Tauc plot from Tauc equation. Using this plot, band gaps were obtained for all the samples which were found to lie in the semiconductor range. The pristine compound was found to possess a band gap value of 2.8 eV. The doped

samples showed a slight decrease in their band gap values with increase in cobalt concentration as shown in Table 4.2. This decrease could possibly be due to the structural deformation caused on doping cobalt in place of copper, as cobalt is known to introduce additional acceptor level close to the valence band edge resulting in narrowing the band gap with a consequent reduction of the energy associated with the transition [166,167]. Absorption in the visible region could be probably due to d – d transition as the compounds are intensely coloured.

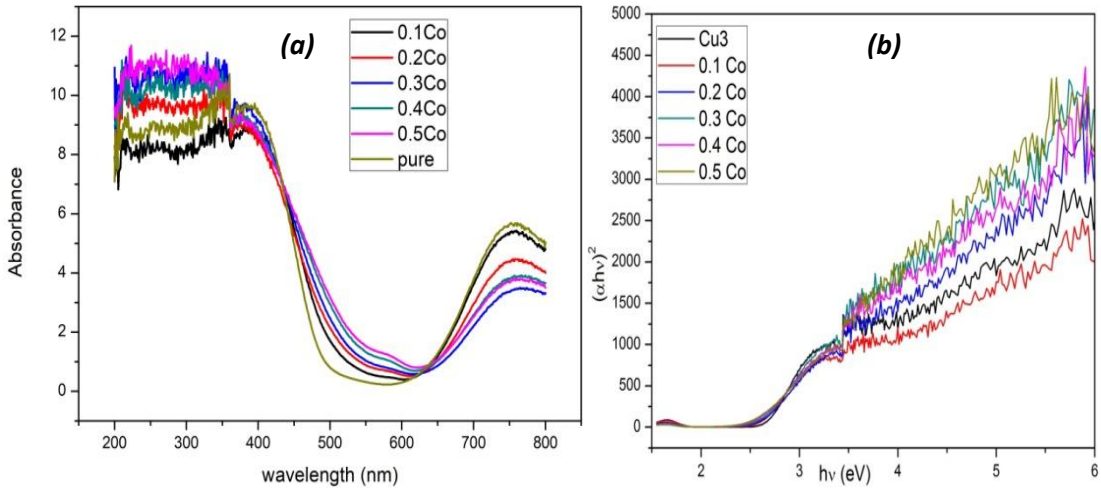

Fig. 4.20 UV-DRS spectra of (a) pristine and Co-doped Cu_3TeO_6 with (b) Tauc plots.

Table 4.2 Obtained band gap values for $Cu_{3-x}Co_xTeO_6$ (x = 0 - 0.5) samples.

Sample	Band gap (eV)
Cu_3TeO_6	2.8
$Cu_{2.9}Co_{0.1}TeO_6$	2.7
$Cu_{2.8}Co_{0.2}TeO_6$	2.6
$Cu_{2.7}Co_{0.3}TeO_6$	2.6
$Cu_{2.6}Co_{0.4}TeO_6$	2.5
$Cu_{2.5}Co_{0.5}TeO_6$	2.5

4.4.2 Nickel doped Cu_3TeO_6

The diffuse reflectance spectroscopy (DRS) for all the samples were recorded in the range 200 to 800 nm and the % reflectance was measured against the wavelength which displayed similar results. The plots of absorbance against the wavelength were plotted (Fig. 4.21). Using the absorbance values, Tauc plot was obtained which gave the optical band gap (inset). The plot has a distinct linear region which denotes the onset of absorption. Thus, extrapolating this linear region to the abscissa yields the energy of the optical band gap of the material. All the band gap values are found to lie in the semiconductor (Table 4.3) region. The visible region shows an absorption hump which could be due to the d – d transition occurring in the system.

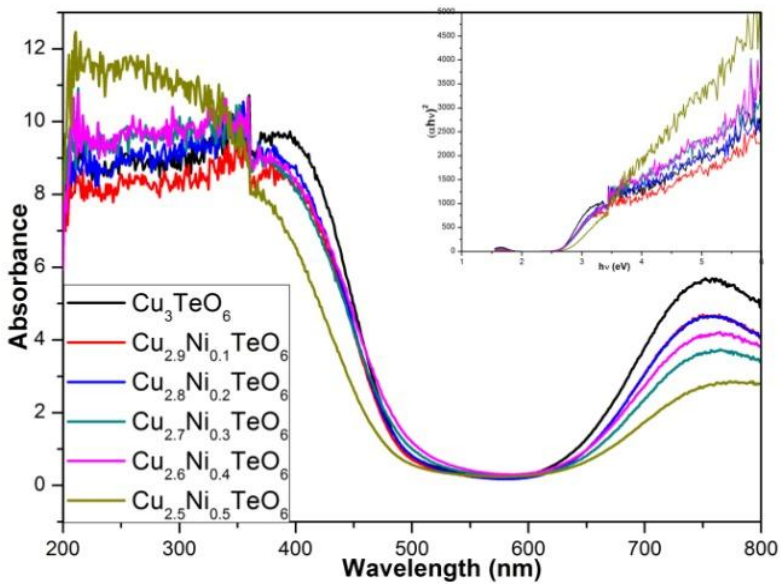

Fig. 4.21 UV - DRS spectra of pristine and Ni-doped Cu_3TeO_6 with Tauc plot in the inset.

Table 4.3 Obtained band gap values for $Cu_{3-x}Ni_xTeO_6$ (x = 0 - 0.5) samples.

Sample	Band-gap (eV)
Cu_3TeO_6	2.8
$Cu_{2.9}Ni_{0.1}TeO_6$	2.8
$Cu_{2.8}Ni_{0.2}TeO_6$	2.8
$Cu_{2.7}Ni_{0.3}TeO_6$	2.7
$Cu_{2.6}Ni_{0.4}TeO_6$	2.7
$Cu_{2.5}Ni_{0.5}TeO_6$	2.7

4.4.3 Zinc doped Cu_3TeO_6

Fig. 4.22 (a) shows the absorption spectra for zinc doped copper tellurates which are found to show absorption in UV region, followed by a hump in the visible region. Using the absorption values, Tauc plot as shown in Fig. 4.22 (b) were obtained in order to get the band gap values of prepared materials, which were found to lie in the semiconductor range. These values are presented in Table 4.4.

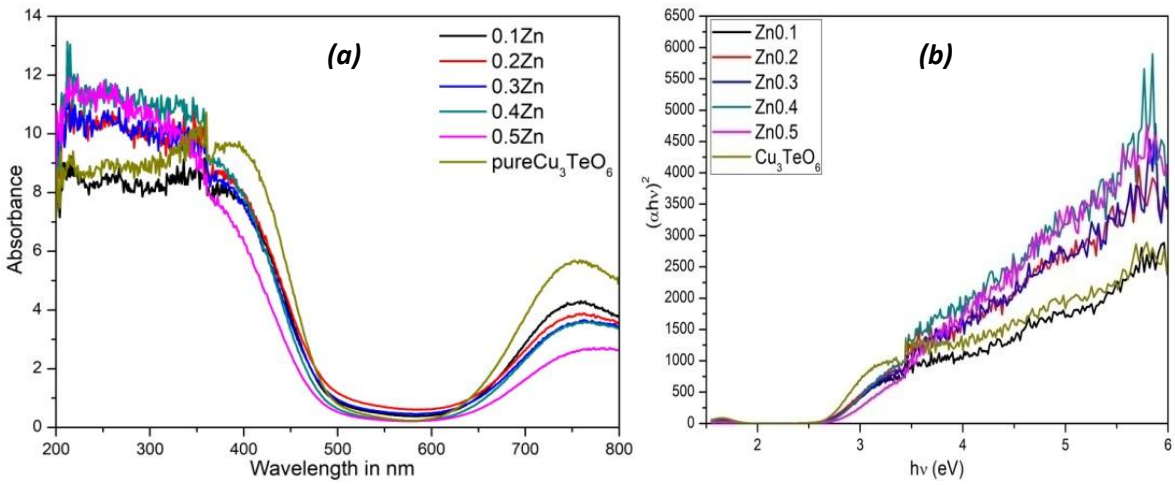

Fig. 4.22 UV - DRS spectra of (a) pristine and Zn doped Cu_3TeO_6 with (b) Tauc plot.

Table 4.4 Obtained band gap values for $Cu_{3-x}Zn_xTeO_6$ (x = 0 - 0.3) samples.

Sample	Band gap (eV)
Cu_3TeO_6	2.8
$Cu_{2.9}Zn_{0.1}TeO_6$	2.8
$Cu_{2.8}Zn_{0.2}TeO_6$	2.7
$Cu_{2.7}Zn_{0.3}TeO_6$	2.7

4.4.4 Manganese doped Cu_3TeO_6

The band gap values for Mn-doped copper tellurates were investigated using the absorbance values obtained from UV – DRS spectroscopy which enabled to plot Tauc plot as shown in the below Fig. 4.23 with inset showing absorbance v/s wavelength with absorption in UV region. The obtained band gap values are thus found to lie in the semiconductor region. A decrease in band gap values is observed with increasing dopant concentration, but they are found to lie below the pristine i.e. Cu_3TeO_6.

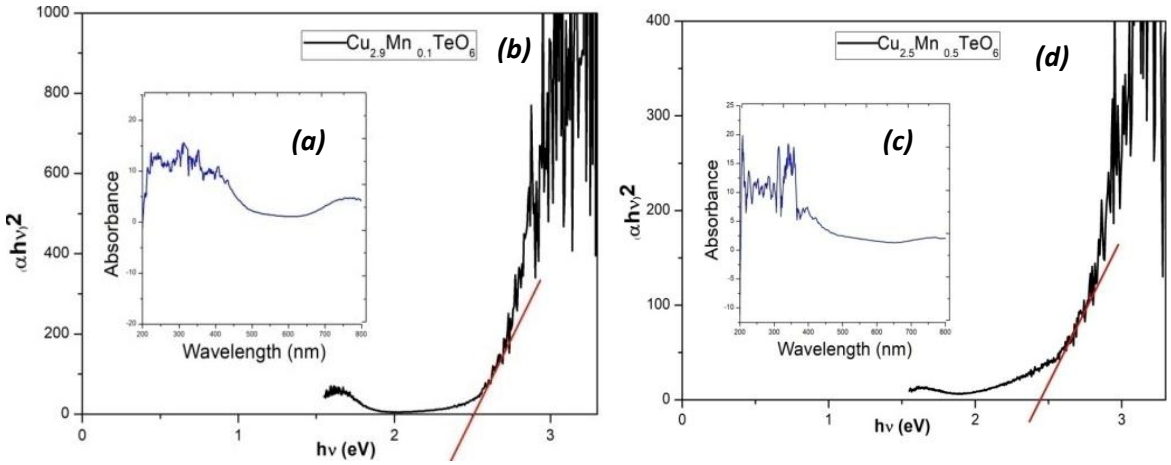

Fig. 4.23 UV - DRS spectra of (a, c) Mn-doped Cu_3TeO_6 in the inset and (b, d) representing Tauc plot.

Table 4.5 Obtained band gap values for $Cu_{3-x}Mn_xTeO_6$ (x = 0 - 0.5) samples.

Sample	Band gap (eV)
Cu_3TeO_6	2.8
$Cu_{2.9}Mn_{0.1}TeO_6$	2.5
$Cu_{2.5}Mn_{0.5}TeO_6$	2.4

4.4.5 $Cu_{2.8}M_{0.2}TeO_6$ (M = W and Mo)

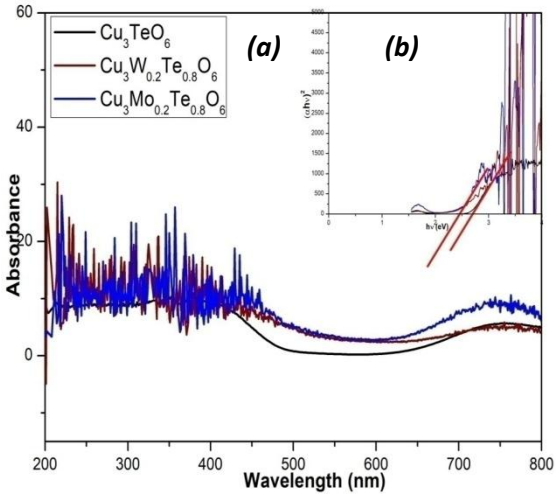

Table 4.6 Obtained band gap values for $Cu_3M_xTe_{1-x}O_6$ (where M = W and Mo; x = 0, 0.2)

Sample	Band gap (eV)
Cu_3TeO_6	2.8
$Cu_3W_{0.2}Te_{0.8}O_6$	2.4
$Cu_3Mo_{0.2}Te_{0.8}O_6$	2.4

Fig. 4.24 UV - DRS spectra of (a) W and Mo-doped Cu_3TeO_6 and (b) Tauc plot in the inset.

The absorbance spectra for W and Mo-doped copper tellurates are presented in Fig. 4.24. The band gap values derived from the Tauc plot are found to lie in the semiconductor region with absorption between 200 – 450 nm for the doped samples. Both W and Mo-doped samples show almost the same value for band gap but when compared with the pristine compound, appear to become narrower (Table 4.6).

4.4.6 Ni_3TeO_6

Fig. 4.25 presents absorbance spectrum of pristine nickel tellurate showing absorption in the UV region. The band gap value obtained from Tauc plot appears to be around 3 eV, which is slightly wider than the values mentioned so far in this chapter.

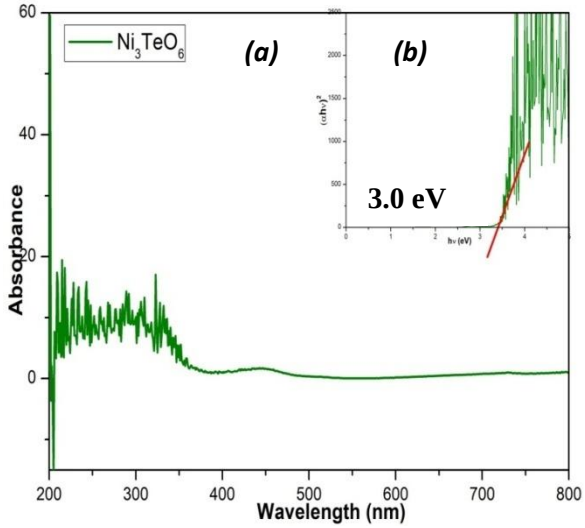

Fig. 4.25 UV - DRS spectra of (a) Ni_3TeO_6 and (b) Tauc plot in the inset.

4.5 ICP-AES

ICP-AES technique was employed to determine the chemical composition of the materials. The results obtained show a very close resemblance with the expected values (Table 4.7).

Table 4.7 Results of the ICP-AES analysis on pristine and doped Cu_3TeO_6

Sample Composition	Metal concentration (wt %)		
	Cu	**M**	**Te**
Cu_3TeO_6	47.5	-	33.1
$Cu_{2.7}Zn_{0.3}TeO_6$	44.2	4.2	33.2

4.6 Scanning Electron Microscopy (SEM)

4.6.1 Pristine Cu_3TeO_6

The surface morphology and microstructures of the pristine Cu_3TeO_6 compound are displayed in Fig. 4.26. The images show agglomerated as well as separated particles with square or cube-shaped morphology. Particles appear to lie close to each other on their edges and are likely to possess developed grain boundaries as seen from the figure which are considered to cause some effect in the properties of compounds [168,169]. Energy dispersive spectroscopy (EDS) on Cu_3TeO_6 is presented for elemental analysis and it is compared with the theoretical values (Fig. 4.26 d). The observed percentage values of each element are in good agreement with the values obtained from theoretical calculations. This suggests that all ions are well precipitated during synthesis and are present in proper stoichiometry.

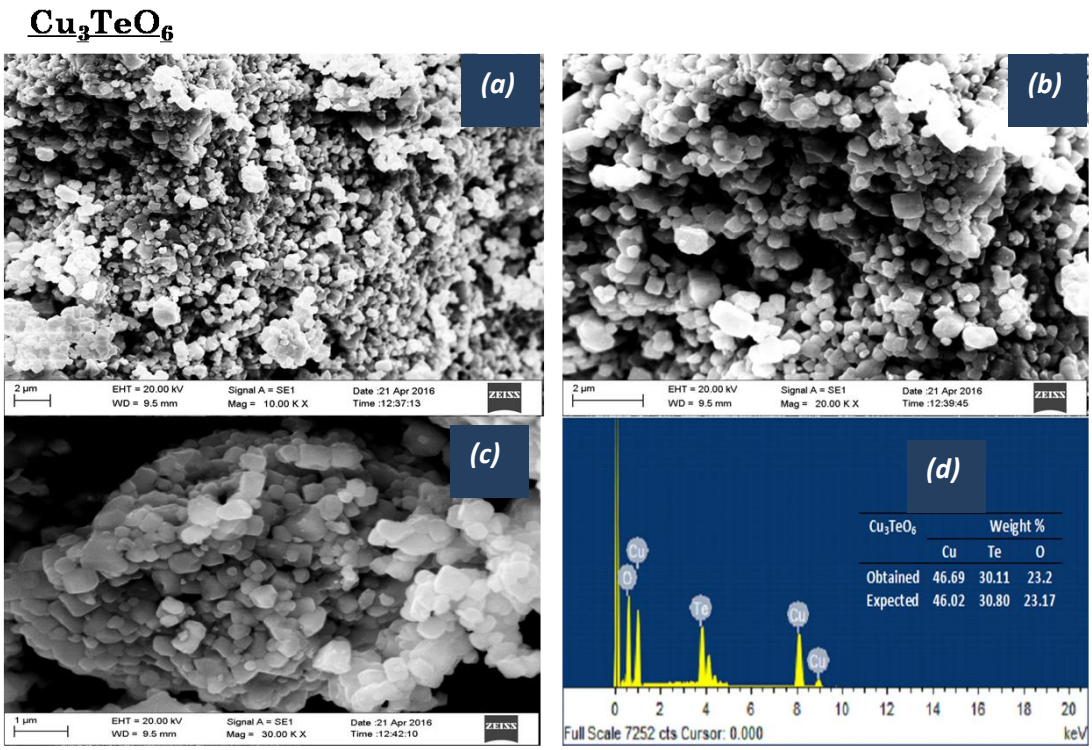

Fig. 4.26 SEM images of pristine Cu_3TeO_6 (a, b and c) with EDS analysis (d).

4.6.2 Cobalt-doped Cu_3TeO_6

The SEM image of $Cu_{2.9}Co_{0.1}TeO_6$ and the $Cu_{2.5}Co_{0.5}TeO_6$ sample is observed to possess similar shaped particles but with smaller particles (Fig. 4.27) compared to the particles of Cu_3TeO_6 (Fig. 4.26) with well-developed grain boundaries. EDS analysis has also been carried out on the highest and the lowest cobalt doped composition and are found to show values close to the theoretically calculated ones (Fig.4.27 b and c).

$Cu_{2.9}Co_{0.1}TeO_6$ **$Cu_{2.5}Co_{0.5}TeO_6$**

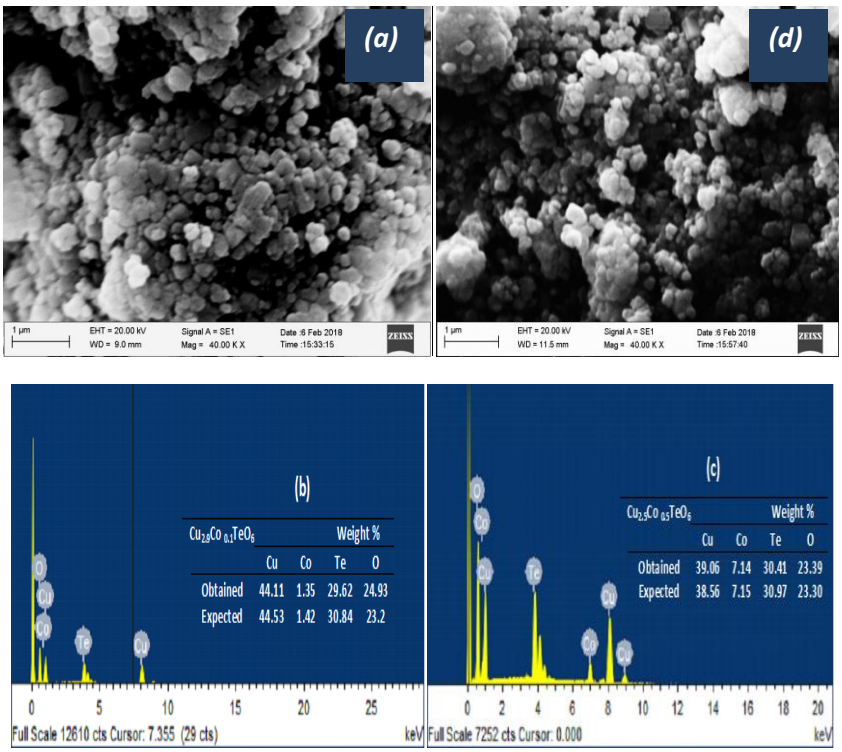

Fig. 4.27 SEM images of $Cu_{2.9}Co_{0.1}TeO_6$ and $Cu_{2.5}Co_{0.5}TeO_6$ (a and d) with EDS analysis (b and c for $Cu_{2.9}Co_{0.1}TeO_6$ and $Cu_{2.5}Co_{0.5}TeO_6$ respectively).

4.6.3 Nickel doped Cu_3TeO_6

Fig. 4.28 represents SEM images for Ni-doped copper tellurate for 0.1 and 0.3 nickel concentrations respectively. Both the compositions show cube shaped morphologies with densely packed particles. It is very much clear from the figure that the highest doped compound possesses smaller particles with developed grain boundaries than the other composition. Particle sizes in both the cases are found to lie in the micron range. EDS data is reported for three concentrations of nickel, which are, $Cu_{2.9}Ni_{0.1}TeO_6$, $Cu_{2.7}Ni_{0.3}TeO_6$ and $Cu_{2.5}Ni_{0.5}TeO_6$. The observed percentage composition values of each element are in good agreement with the values obtained from theoretical calculations.

$Cu_{2.9}Ni_{0.1}TeO_6$ **$Cu_{2.7}Ni_{0.3}TeO_6$**

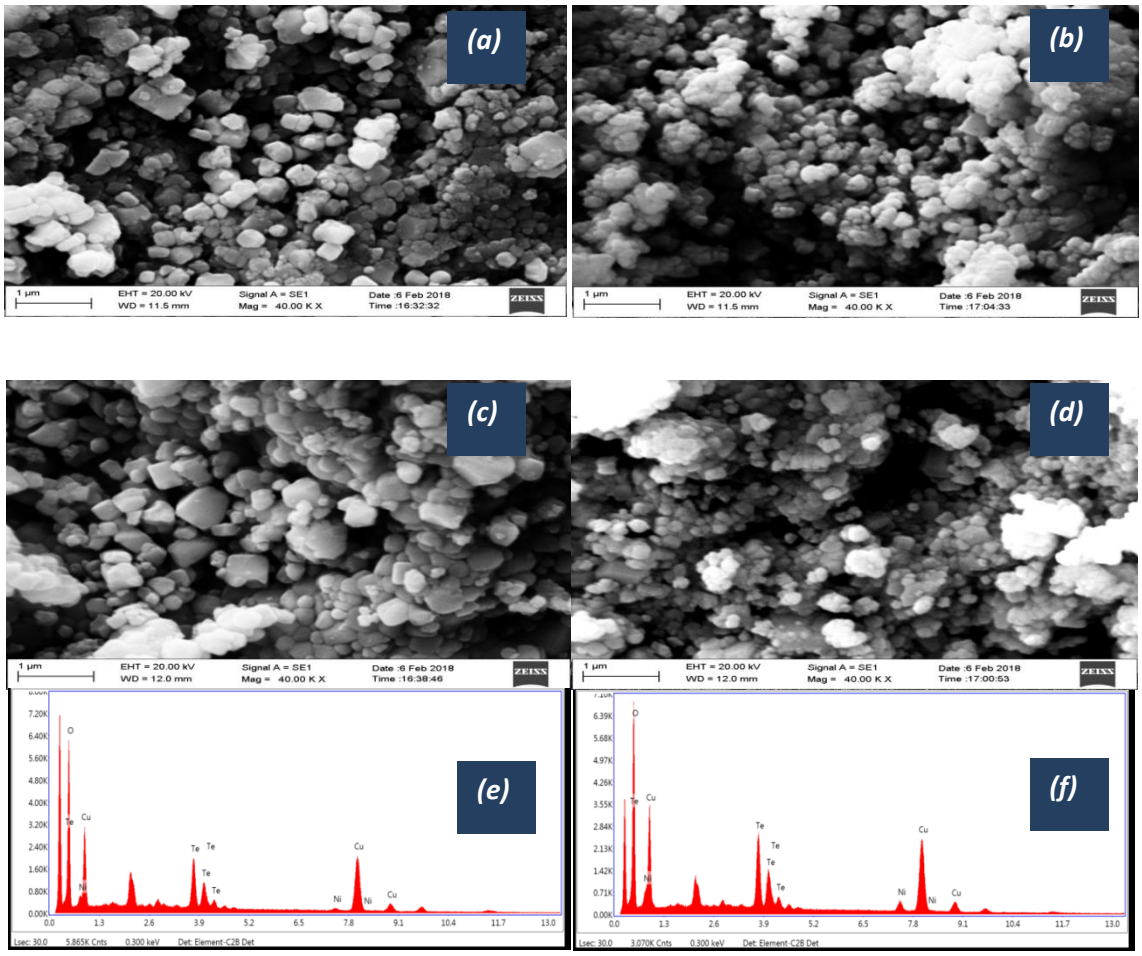

Elements	Wt % Obt.	Wt % Calc.
O	18	23
Te	26	31
Ni	1.44	1.42
Cu	55	45

Elements	Wt % Obt.	Wt % Calc.
O	16	23
Te	25	31
Ni	4.5	4.3
Cu	45	42

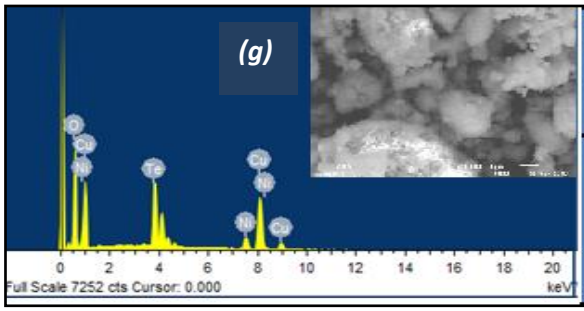

Elements	Weight % obtained	Weight % theoretical
Cu	39.6	38.6
Ni	6.6	7.1
Te	30.35	31
O	23.4	23.3

Fig. 4.28 SEM images of $Cu_{2.9}Ni_{0.1}TeO_6$ (a and c) and $Cu_{2.7}Ni_{0.3}TeO_6$ (b and d) with EDS analysis (e, f and g for $Cu_{2.9}Nio_{0.1}TeO_6$, $Cu_{2.7}Ni_{0.3}TeO_6$ and $Cu_{2.5}Ni_{0.5}TeO_6$ respectively).

4.6.4 Silver doped Cu_3TeO_6

The SEM image for the $Cu_{2.9}Ag_{0.1}TeO_6$ compound is shown in Fig. 4.29 along with its EDS analysis. All the images present micron-sized particles, agglomerated and densely piled up one above the other presenting highly developed grain boundaries similar to pristine copper tellurate. Its composition analysis was carried out using EDS which enabled us to correlate their percent weight obtained values with the calculated ones wherein it showed to match the expected values.

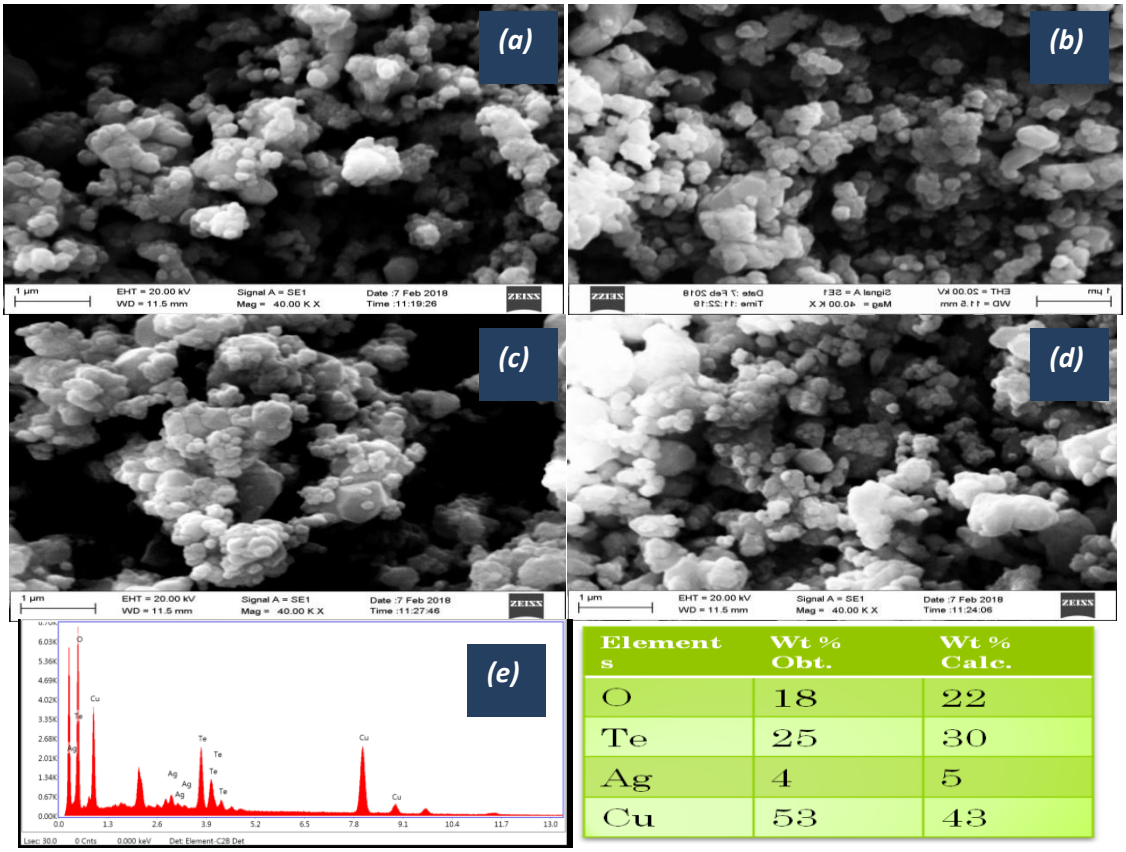

Elements	Wt % Obt.	Wt % Calc.
O	18	22
Te	25	30
Ag	4	5
Cu	53	43

Fig. 4.29 SEM images of $Cu_{2.9}Ag_{0.1}TeO_6$ (a, b, c and d) with EDS analysis (e).

4.6.5 Molybdenum and tungsten doped Cu_3TeO_6

$Cu_3Mo_{0.1}Te_{0..9}O_6$

Morphological studies along with elemental analysis were carried out on Mo-doped copper tellurate (Fig. 4.30) which depicted their densely adhered cube-like particles. This micron-sized sample was analysed by EDS which provided elemental composition of the sample and was found to represent the expected weight percent values.

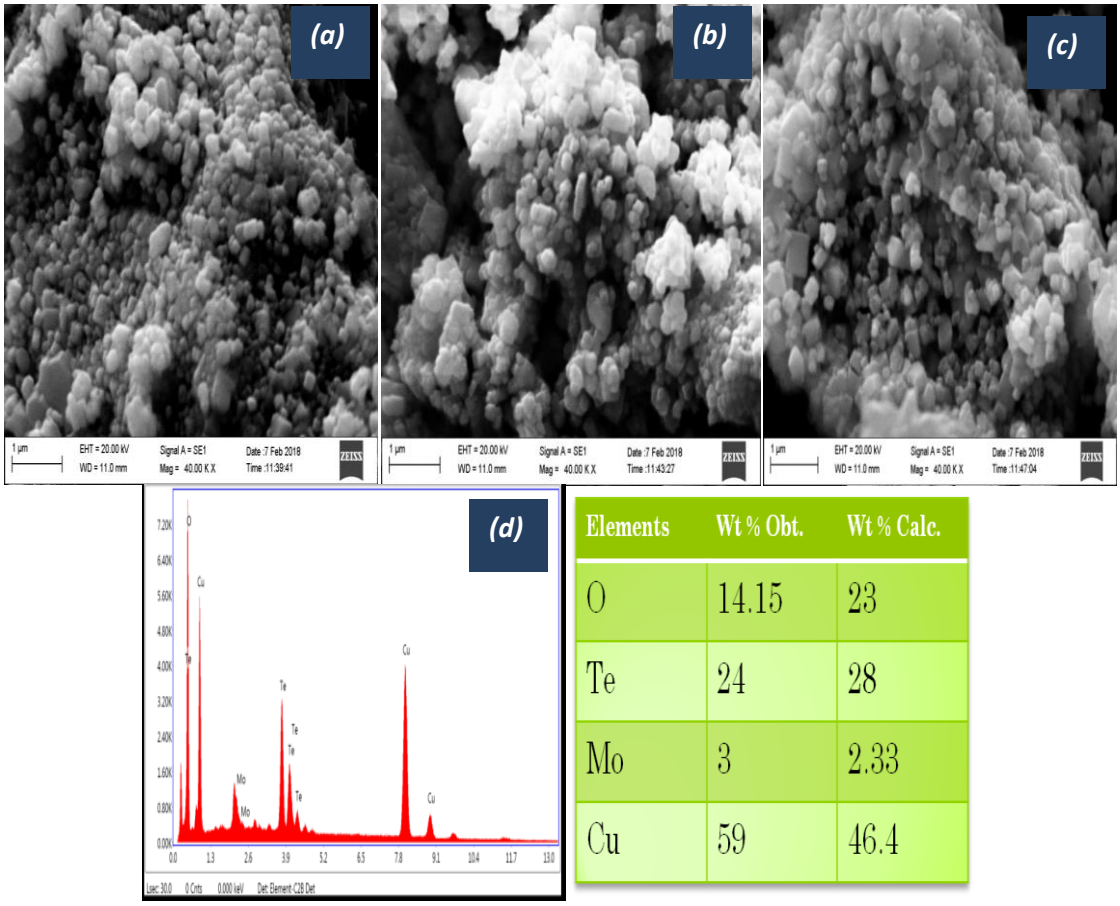

Elements	Wt % Obt.	Wt % Calc.
O	14.15	23
Te	24	28
Mo	3	2.33
Cu	59	46.4

Fig. 4.30 SEM images of $Cu_3Mo_{0.1}Te_{0.9}O_6$ (a, b and c) with EDS analysis (d).

$Cu_3W_{0.1}Te_{0.9}O_6$

The SEM-EDS analysis is presented for W doped copper tellurate in Fig. 4.31 which represent the weight percent obtained matching the theoretically calculated ones.

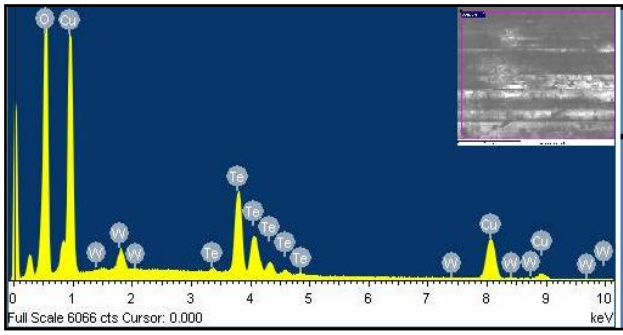

Elements	Weight % obtained	Weight % theoretical
Cu	43.4	45.4
Te	27.8	27.35
W	4.0	4.4
O	24.7	22.9

Fig. 4.31 SEM EDS analysis on $Cu_3W_{0.1}Te_{0.9}O_6$.

4.6.6 Pristine Ni_3TeO_6

The surface morphology of nickel tellurate particles is presented in Fig. 4.32. The particles appear to show spherical irregular shapes of geometry which are densely arranged on one another. The sizes of particles are found to lie in the micron range. Although the arrangement of particles is compact, each one of it projects out visibly. EDS analysis showed obtained value are consistent with the calculated ones.

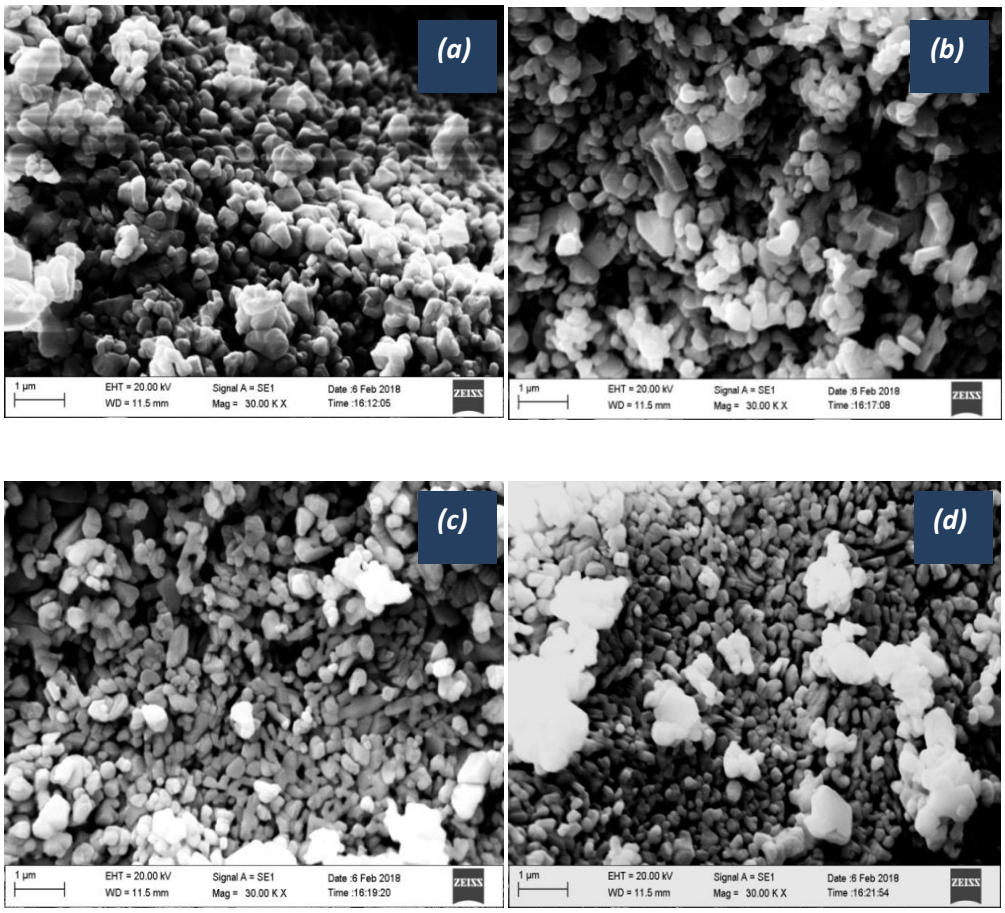

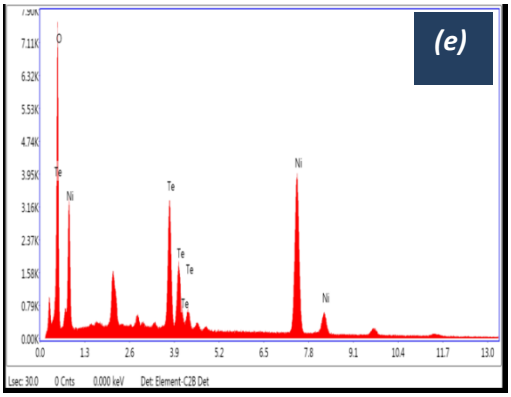

Elements	Wt % Obt.	Wt % Calc.
O	14	24
Te	26	32
Ni	46	44

Fig. 4.32 SEM images of Ni_3TeO_6 (a, b, c and d) with EDS analysis (e).

4.6.7 Pristine Fe_2TeO_6 and Eu doped Fe_2TeO_6

Fig. 4.33 represents surface morphology of pristine Fe_2TeO_6 and Eu doped iron tellurate. The images show agglomerated particles with a mixture of small and slightly bigger sized particles. It is observed that the doped compound possess a smaller set of particles than the pristine revealing the effect of dopant on the structural features. EDS analysis on pristine iron tellurate is shown which reveal that the observed values lie in close proximity with the calculated ones.

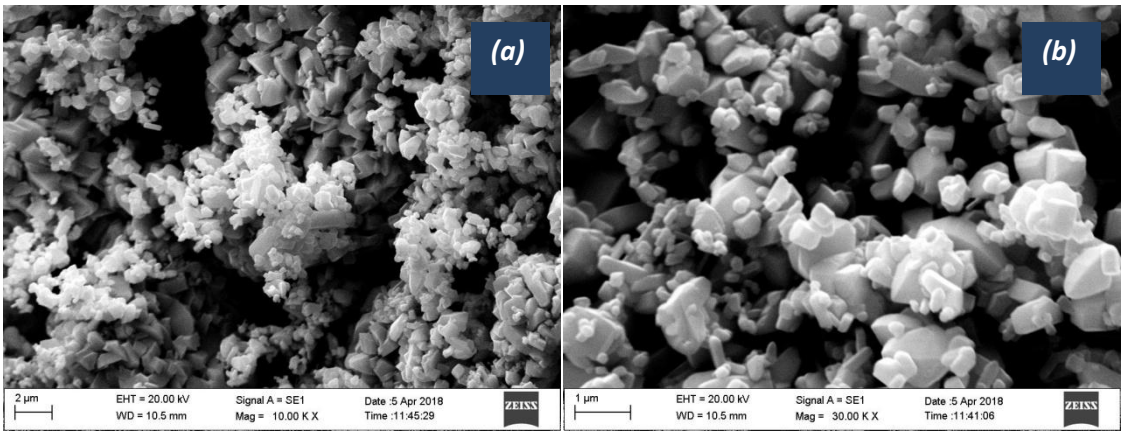

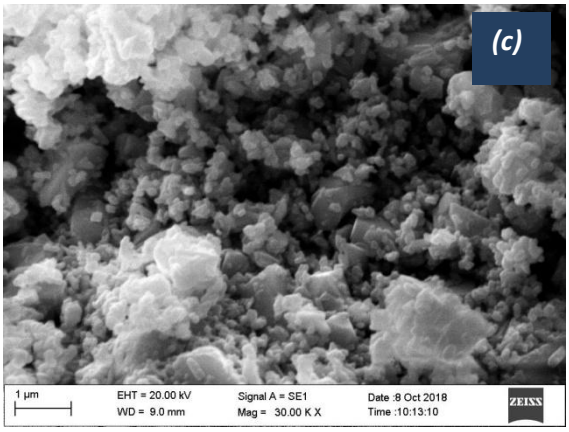

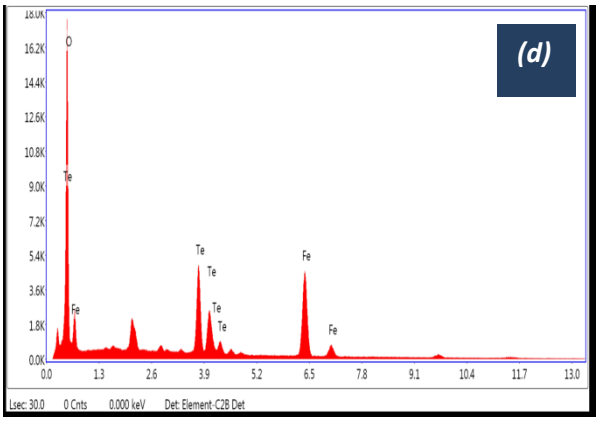

Elements	Wt % Obt.	Wt % Calc.
O	23	29
Te	37	38
Fe	40	33

Fig. 4.33 SEM images of Fe_2TeO_6 (a, b) and $Fe_{1.9}Eu_{0.1}TeO6$, (c) with EDS analysis on of Fe_2TeO_6 (d).

4.6.8 Pristine Al_2TeO_6

The morphological features of pristine Al_2TeO_6 are represented in Fig. 4.34 which shows some interesting structural features. Particles appear to hold rod-like elongated morphology, which seems like spikes at some places. EDS reveals the existence of all the expected elements in the system.

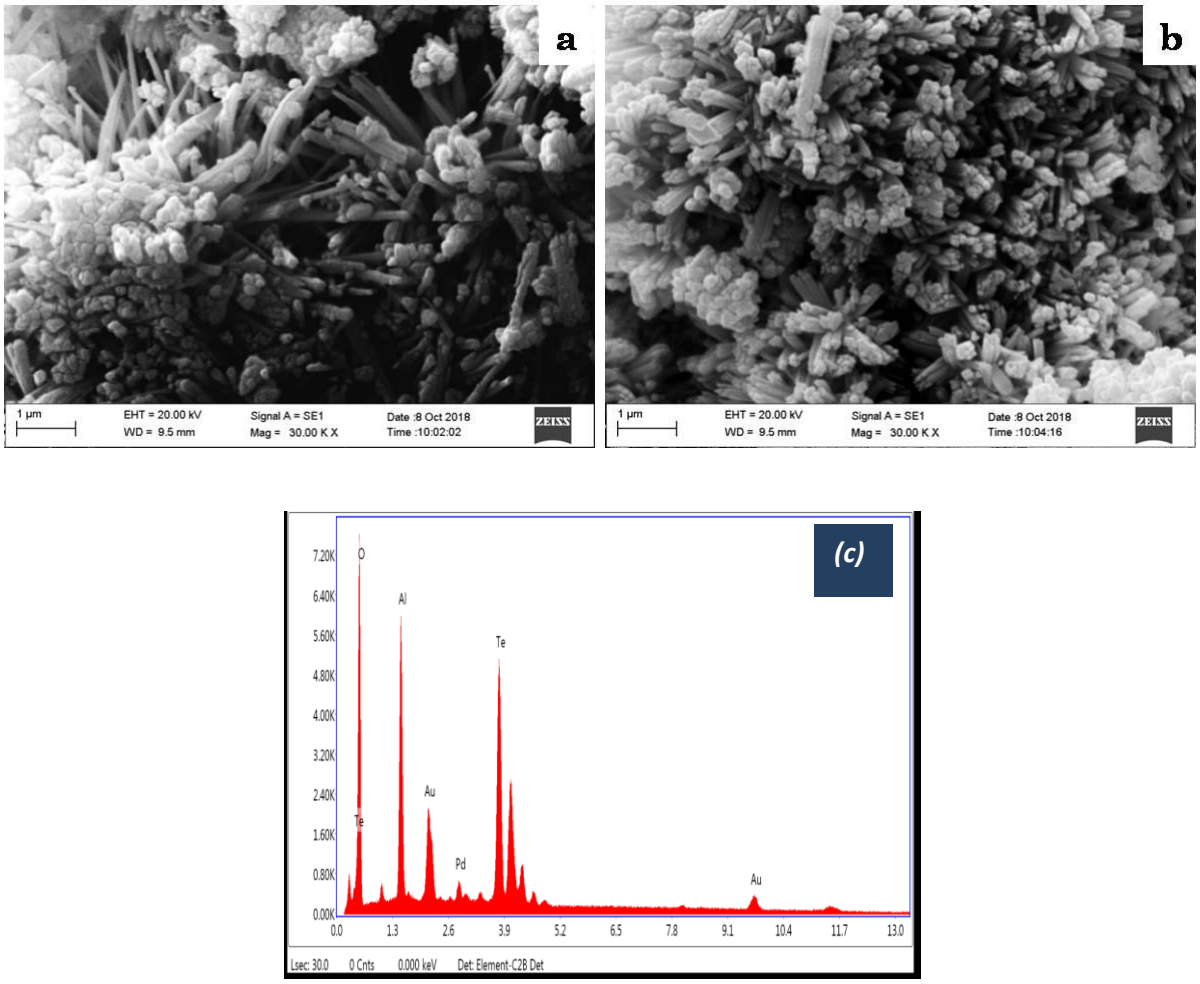

Fig. 4.34 SEM images of Al_2TeO_6 compound (a and b) with EDS analysis (c).

4.6.9 Tungsten doped Ni_3TeO_6

Fig. 4.35 represents surface morphology of W doped nickel tellurate i.e. $Ni_3Te_{0.9}W_{0.1}O_6$. The images possess particles with a mixture of elongated structures. It is observed that the surface of these structures carries some dusty particles on to them. These structural features are totally different from the pristine nickel tellurate. EDS analysis reveals the presence of all expected elements in the sample.

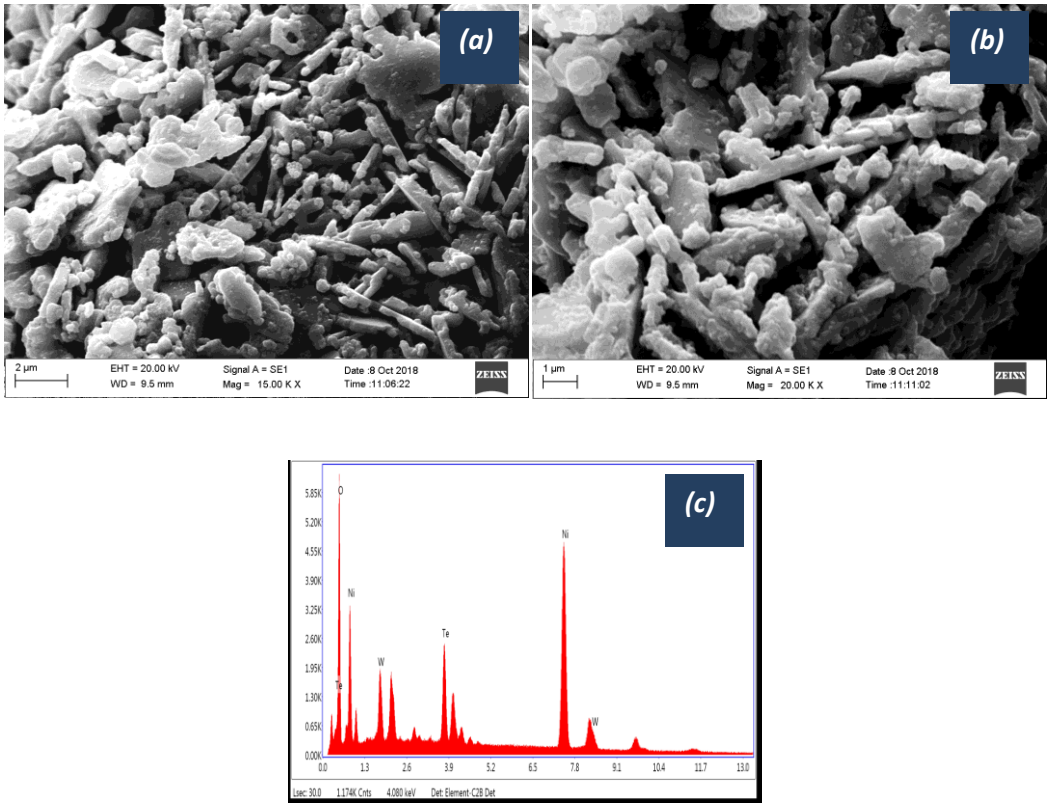

Fig. 4.35 SEM images of W doped Ni_3TeO_6 (a and b) with EDS analysis (c).

4.6.10 Molybdenum doped Ni_3TeO_6

Particle morphology of Mo-doped nickel tellurate i.e. $Ni_3Te_{0.9}Mo_{0.1}O_6$ presents similar structures like that of the W doped nickel tellurate as shown in Fig. 4.36. The images possess elongated plate-like structures with some grainy particles on their surfaces. These structural features are totally different from the pristine nickel tellurate. EDS analysis reveals the presence of all expected elements in the sample.

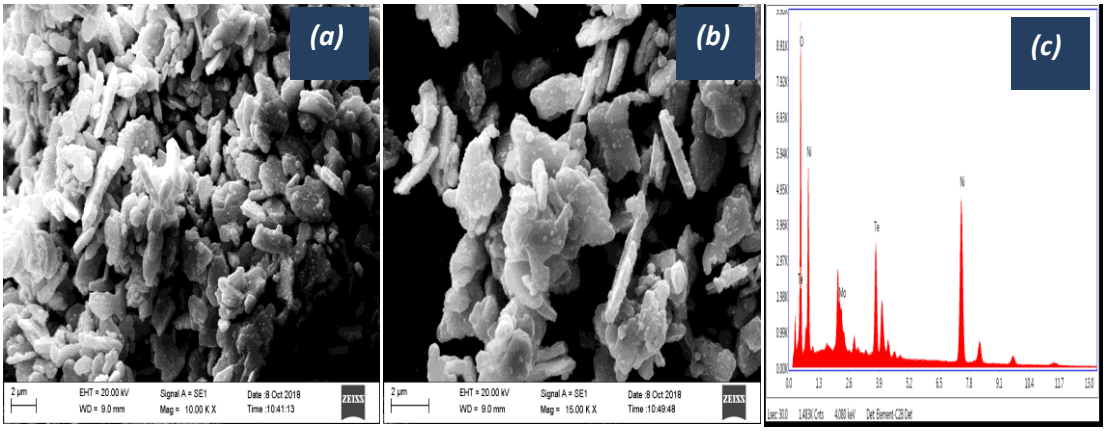

Fig. 4.36 SEM images of Mo-doped Ni_3TeO_6 (a and b) with EDS analysis (c).

4.6.11 Manganese doped Cu_3TeO_6

The surface morphology of manganese doped copper tellurate i.e. $Cu_{2.7}Mn_{0.3}TeO_6$ particles is presented in Fig. 4.37. The particles appear to show granular morphologies which densely connect each other. EDS analysis shows the presence of expected elements in the system.

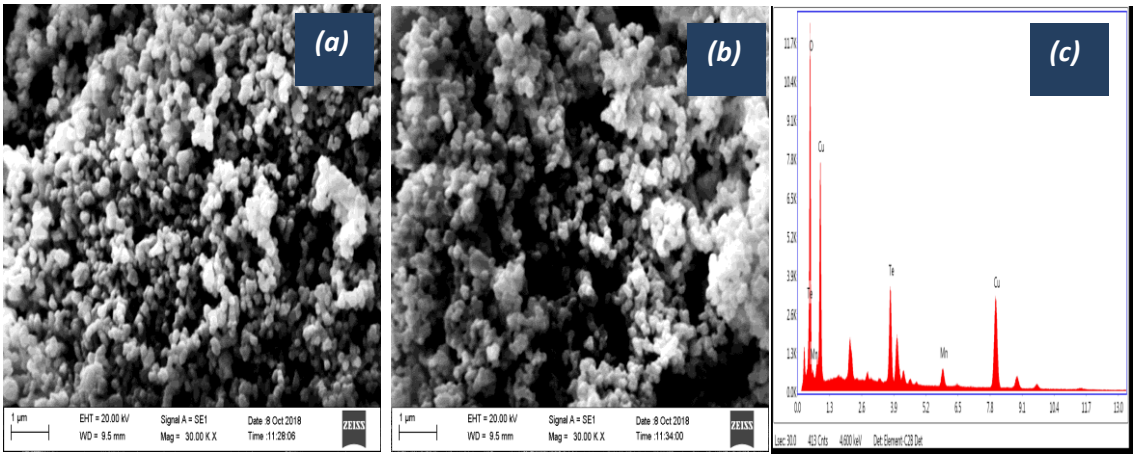

Fig. 4.37 SEM images of Mn-doped Cu_3TeO_6 (a and b) with EDS analysis (c).

4.6.12 Zinc doped Cu_3TeO_6

Morphological studies along with elemental analysis were carried out on Zn doped copper tellurate in Fig. 4.38 which portrayed their densely adhered, agglomerated particles. This micron-sized sample was estimated for EDS which provided elemental composition of the sample and was found to represent the expected elements.

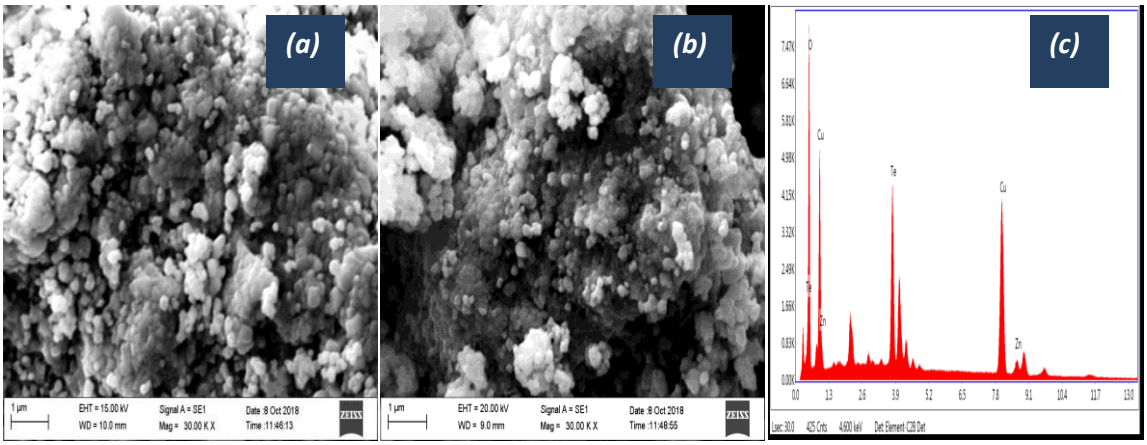

Fig. 4.38 SEM images of Zn doped Cu_3TeO_6 (a and b) with EDS analysis (c).

4.7 Transmission Electron Microscopy (TEM)

4.7.1 Pristine Cu_3TeO_6

The TEM images of the pristine sample are shown in Fig. 4.39. The images show agglomerated as well as separated particles with square or cube-shaped structure. Particles appear to live side by side to each other with sizes in the micron range. Pristine tellurate contains dense equiaxial, sub-micron grains and so possess well-developed grain boundaries.

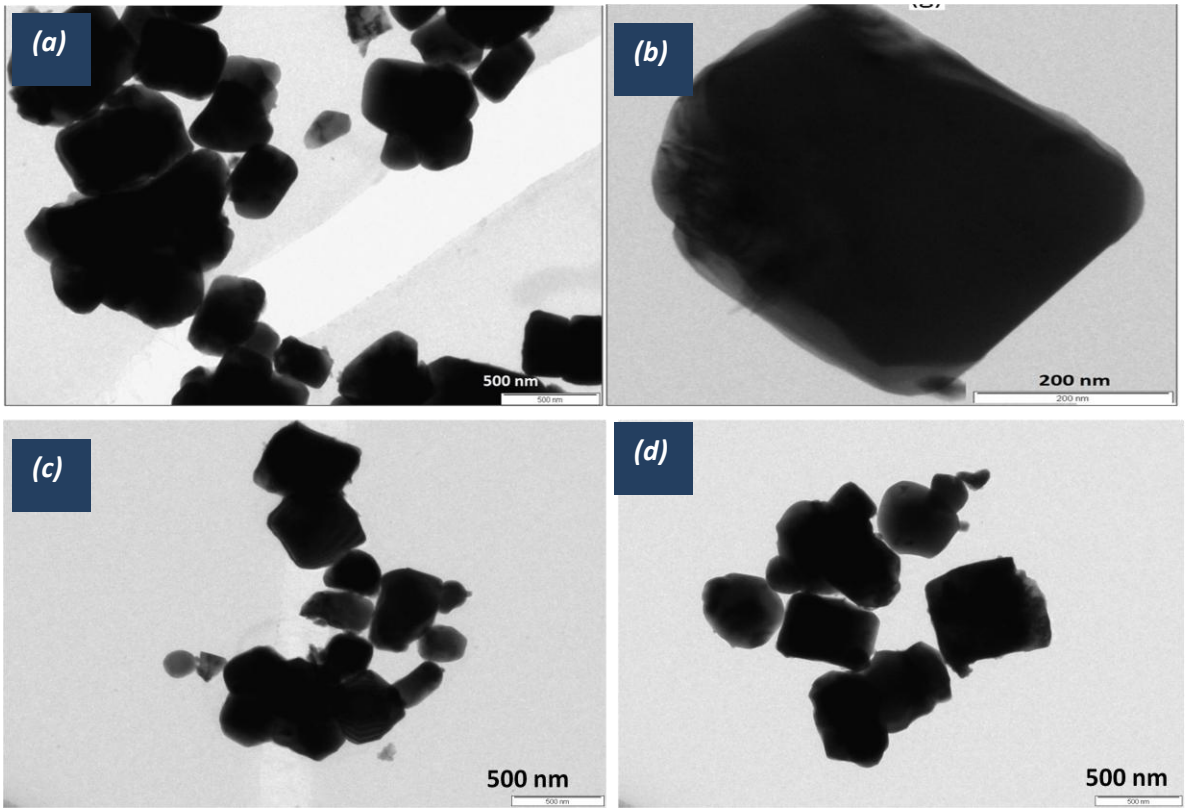

Fig. 4.39 TEM images of Cu_3TeO_6 (a, b, c and d).

4.7.2 Cobalt-doped Cu_3TeO_6

Fig. 4.40 represents the TEM images of cobalt doped copper tellurates depicting their shape and size. The images are presented from 'a' to 'e' are arranged with an ascending order of the cobalt ion concentration. It is noted that, with an increase in cobalt dopant concentration, particle size decreases, with the smallest size in the highest concentration. $Cu_{2.5}Co_{0.5}TeO_6$ sample is observed to possess smaller particles compared to the particles of Cu_3TeO_6 which show relatively higher particle size. The dense-equiaxial, micro grains are seen to possess well-developed grain boundaries, to a higher extent in doped then in the pristine compound due to small sizes of doped samples.

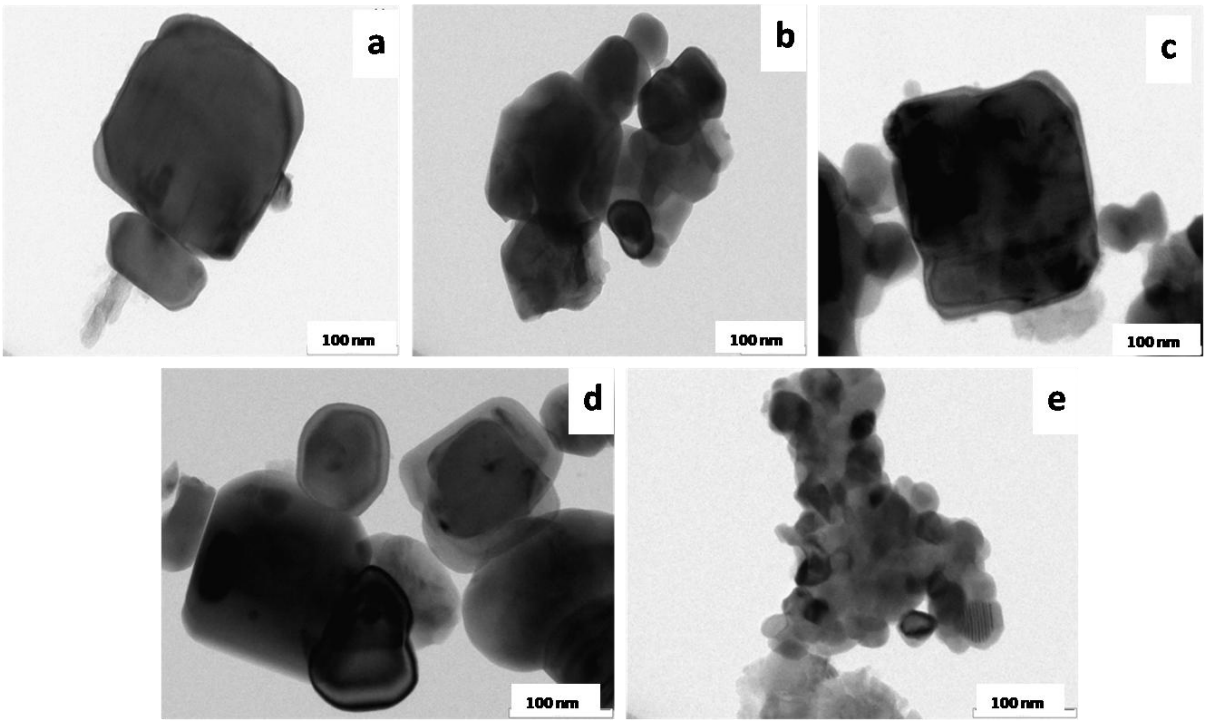

Fig. 4.40 TEM images of Co-doped Cu_3TeO_6 from (a) to (e) are arranged with an ascending order of the cobalt ion concentration with scaling of 100 nm.

4.7.3 Nickel doped Cu_3TeO_6

The TEM of nickel-doped copper tellurate compounds are presented in Fig. 4.41 which show agglomerated particles with irregular morphologies. Particle dimensions are found to lie in the micron range. No other specific structural features are observed.

$Cu_{2.5}Ni_{0.5}TeO_6$ and $Cu_{2.7}Ni_{0.3}TeO_6$

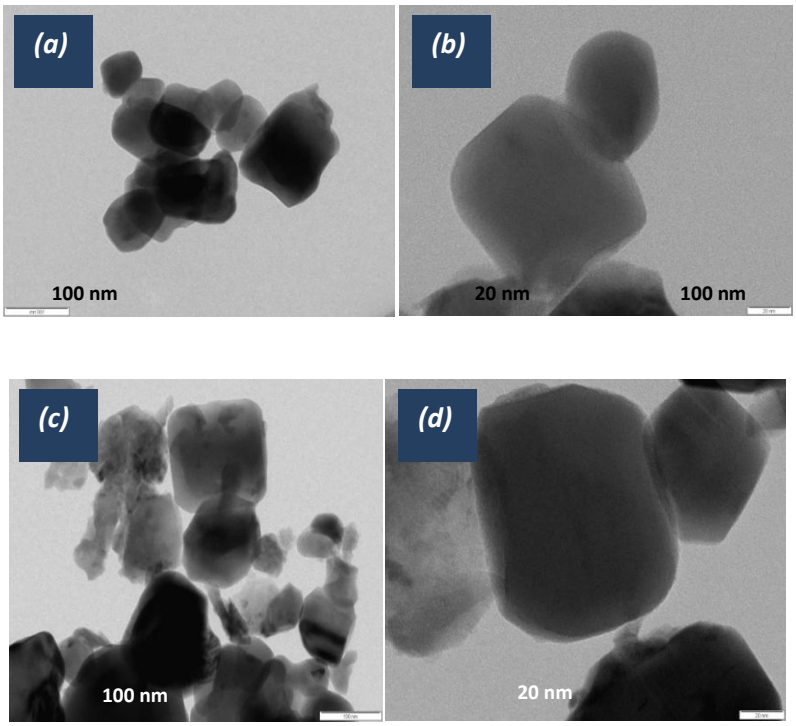

Fig. 4.41TEM images of $Cu_{2.5}Ni_{0.5}TeO_6$ (a and b) $Cu_{2.7}Ni_{0.3}TeO_6$ (c and d).

4.7.4 Pristine Ni_3TeO_6

Fig. 4.42 represents TEM images of pristine nickel tellurate which possess particles in the micron range. Particles appear to present shapes of the hexagon in between the irregular species.

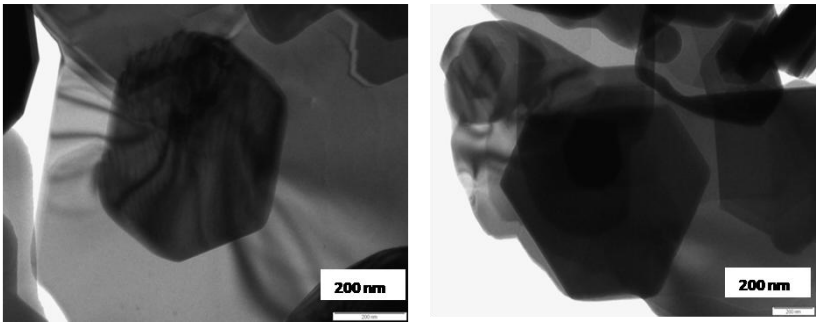

Fig. 4.42 TEM images of Ni_3TeO_6 at 200 nm.

4.8 X-ray Photoelectron Spectroscopy (XPS)

X-ray photoelectron spectra (XPS) were obtained, so as to understand the surface composition and chemical state of the metal ions.

4.8.1 Pristine Cu_3TeO_6

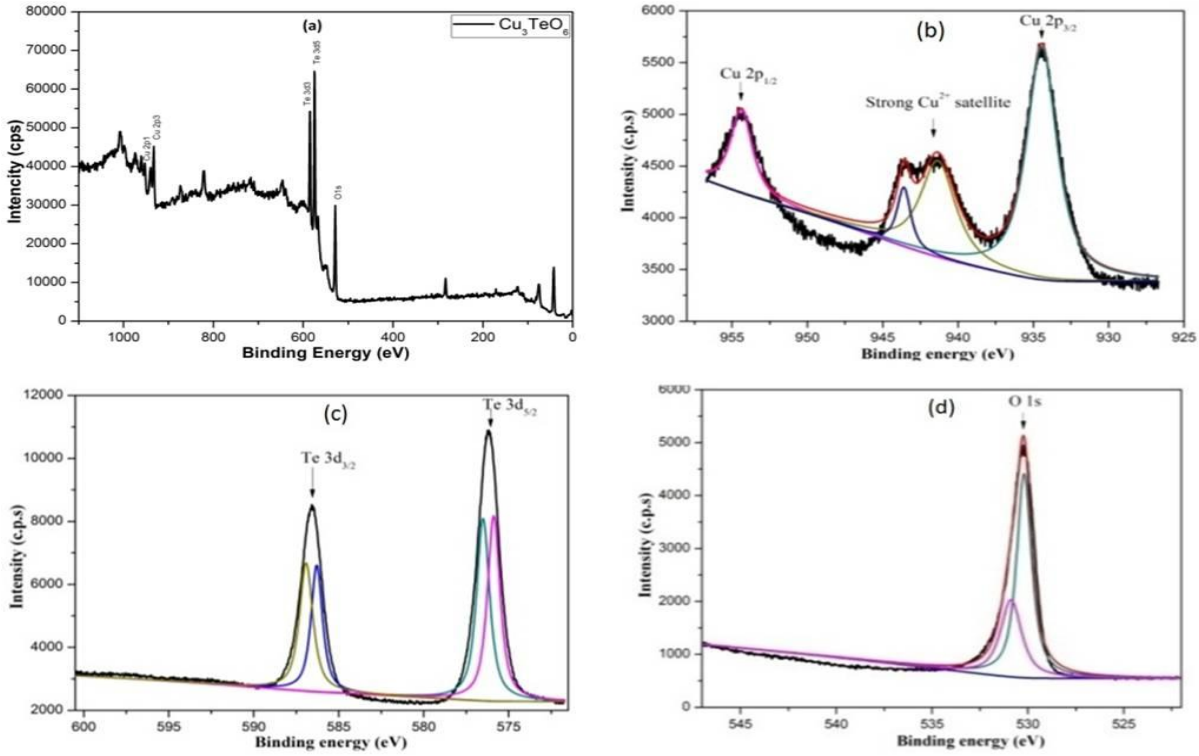

Fig. 4.43 High resolution XPS scan for pristine Cu_3TeO_6 showing (a) full scan (b) Cu 2p (c) Te 3d (d) O 1s peaks.

Fig. 4.43 shows high-resolution XPS spectra of Cu (2p), O (1s) and Te (3d) elements of pristine copper tellurate. Full scan XPS spectra of the pristine sample are shown in Fig. 4.43 (a) which disclose the elements present in the compound. XPS spectrum of copper for pristine copper tellurate is shown in Fig. 4.43 (b). It presents two signals for Cu ($2p_{3/2}$) and Cu ($2p_{1/2}$) at 934.49 eV and 954.41 eV respectively along with a strong Cu^{2+} satellite at ~ 943 eV. These are the characteristic features of copper in 2+ oxidation state [164].

Te (3d) spectra of Cu_3TeO_6 Fig. 4.43(c) shows the presence of two peaks at 576.23 eV (Te $3d_{5/2}$) and 586.6 eV (Te $3d_{3/2}$) which approach in between valence states of tellurium (Te^{6+} and Te^{4+}) perhaps in 1: 1 ratio. XPS spectra of O (1s) shows a characteristic peak at 529.7 eV for lattice oxygen along with a shoulder peak at ~ 532 eV which is observed due to surface oxygen or defect oxygen [170,171] (Fig. 4.43(d)). No other impurity peak was observed, which confirmed the purity of pristine copper tellurate.

4.8.2 Cobalt-doped Cu_3TeO_6

Full scan XPS spectrum for doped copper tellurate along with individual high resolution Cu 2p spectrum are shown in Fig. 4.44 (a`) and 4.44(b`) respectively. The Cu 2p spectrum represents two signals positioned at 934.49 eV and 954.41 eV for Cu ($2p_{3/2}$) and Cu ($2p_{1/2}$) respectively along with a strong Cu^{2+} satellite at ~ 943 eV. This presents a characteristic feature of Cu in 2+ oxidation state.

The $Cu_{2.7}Co_{0.3}TeO_6$ sample shows the presence of two peaks for Te $3d_{5/2}$ and Te $3d_{3/2}$ at 576.05 eV and 586.44 eV along with two shoulder peaks at 577.3 eV and 587.9 eV (Fig. 4.44(c`)), which correspond to Te^{6+} and Te^{4+} ions. This suggest that both Te^{6+} and Te^{4+} could be present in the system since the reported value for Te^{4+} is 576.1 eV (Te $3d_{5/2}$) and 586.5 eV (Te $3d_{3/2}$) and reported value for Te^{6+} is 577.3 eV (Te $3d_{5/2}$) and 587.7 eV (Te $3d_{3/2}$) [172][173][174]. A similar trend is observed in Te 3d spectrum of $Cu_{2.5}Co_{0.5}TeO_6$ (Fig. 4.45 (e)), wherein, peak of Te^{4+} get shifted towards lower side (575.6 eV for Te $3d_{5/2}$) with relatively less intensity than $Cu_{2.7}Co_{0.3}TeO_6$ and peak of Te^{6+} towards higher side (577.9 eV for Te $3d_{3/2}$) with prominent separation (Fig. 4.45 e).

Relatively more amount of defect oxygen species are observed in doped samples (Fig. 4.44(d`) and Fig 4.45 (d)) than in pristine Fig. 4.43(d). The surface oxygen species are found to increase on Co doping (Fig. 4.44(d`) and Fig. 4.45 (d)) in view of the fact that metal doping usually accompanies the creation of defects [175]. This could be the probable reason for dual valence of Te in higher doped samples.

High-resolution XPS spectrum of Co (2p) of the doped sample is given in Fig. 4.44(e). It shows the presence of two peaks at 780.72 eV and 796.3 eV corresponding to Co $2p_{3/2}$ and Co $2p_{1/2}$ along with shakeup satellites at 785 eV and 798 eV respectively. The energy difference between Co $2p_{3/2}$ and Co $2p_{1/2}$ peaks is found to be around 15.58 eV, which is close to the standard value for CoO (15.5 eV) [175]. These features are characteristic of Co (II). The satellite peak at 785 eV is approximately 5 eV higher in energy than the Co $2p_{3/2}$ main peak, which further confirms the 2+ valence of Co ion [164,175,176]. XPS analysis on $Cu_{2.5}Co_{0.5}TeO_6$ sample present similar interpretation (Fig. 4.45).

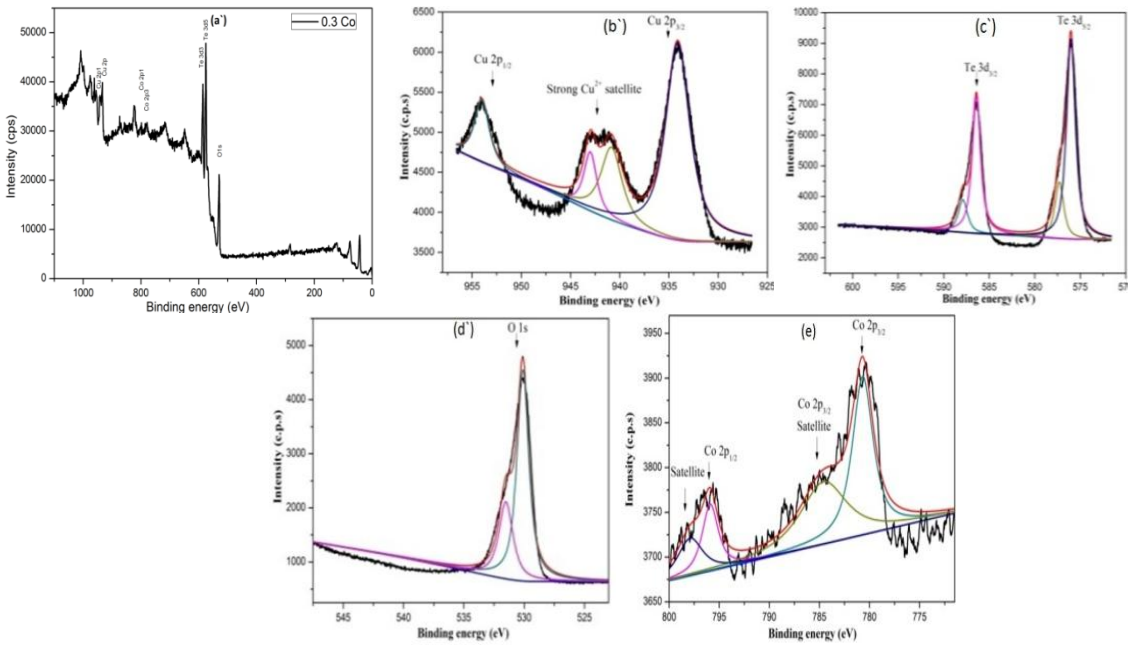

Fig. 4.44 XPS scan for Co-doped Cu_3TeO_6 shows (a`) full scan (b`) Cu 2p (c`) Te 3d (d`) O 1s (e) Co 2p peaks.

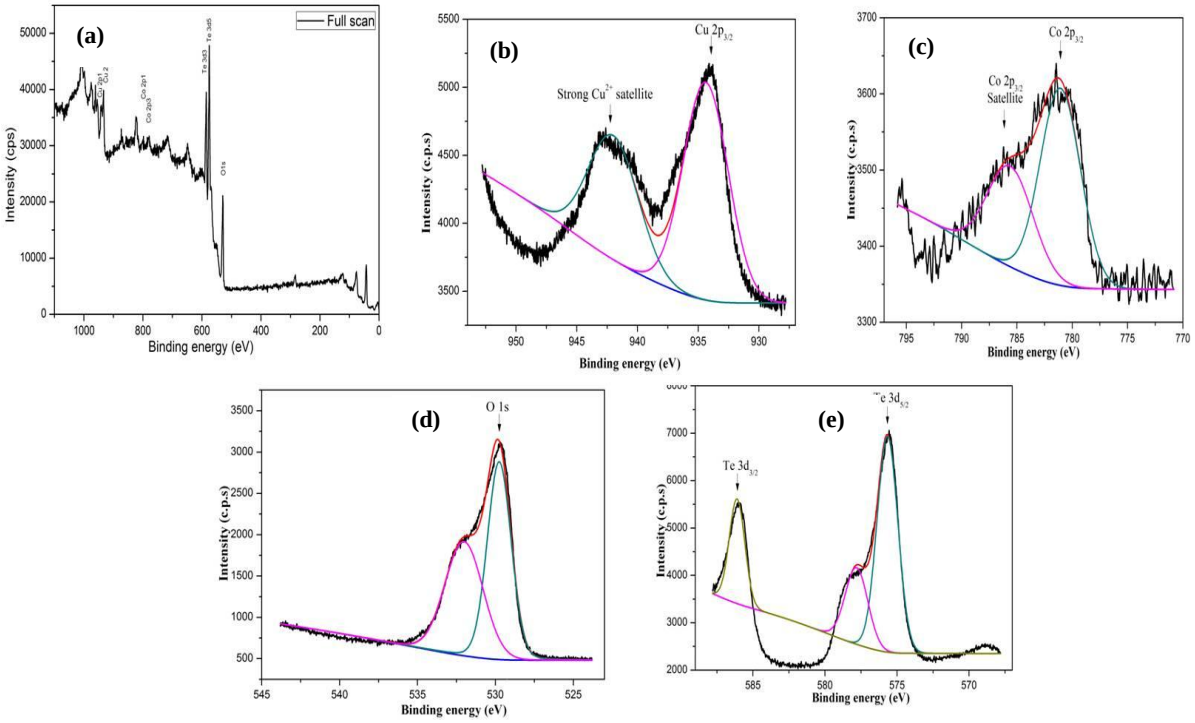

Fig. 4.45 XPS scan for $Cu_{2.5}Co_{0.5}TeO_6$ showing (a) full scan (b) Cu 2p (c) Co 2p (d) O 1s (e) Te 3d peaks.

4.8.3 Nickel doped Cu_3TeO_6

The XPS spectra for nickel doped copper tellurate compound $Cu_{2.7}Ni_{0.3}TeO_6$ is presented in Fig.4.46. It shows spectra for Cu 2p with two major peaks i.e. Cu $2p_{3/2}$ and Cu $2p_{1/2}$ at 934.49 eV and 954.41 eV along with their respective satellites, confirming its existence in 2+ oxidation state. The spectrum for dopant Ni 2p is shown, which reveals the presence of nickel in 2+ valence, as it displays Ni $2p_{3/2}$ major peak at 855.3 eV along with its satellite at 861.6 eV [177,178]. Te 3d spectrum shows two peaks at 576.4 eV and 586.7 eV for Te $3d_{5/2}$ and Te $3d_{3/2}$ representing its Te^{6+} form. The fitting spectrum for O 1s shows characteristic peaks at 529.7 eV and 532 eV which are attributed to the bonded lattice oxygen and defect oxygen respectively.

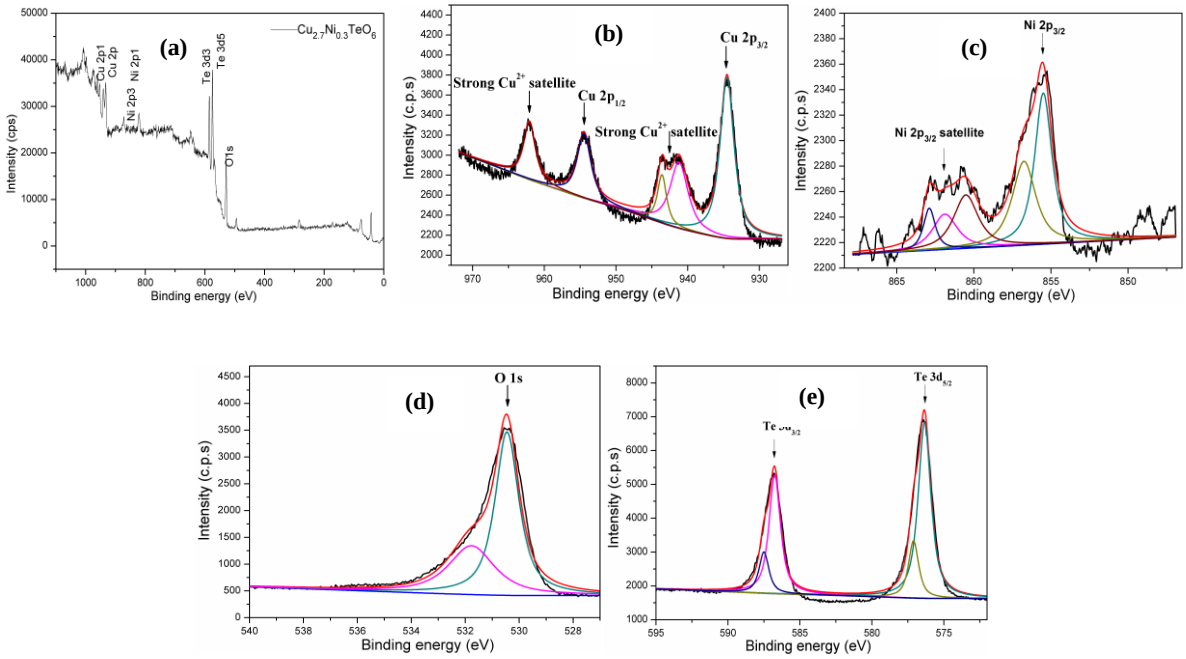

Fig. 4.46 XPS scan for $Cu_{2.7}Ni_{0.3}TeO_6$ *showing (a) full scan (b) Cu 2p (c) Ni 2p (d) O 1s (e) Te 3d peaks*

4.8.4 Manganese doped Cu_3TeO_6

The representative XPS spectra are presented for manganese doped copper tellurate $Cu_{2.5}Mn_{0.5}TeO_6$ in Fig. 4.47 for Cu 2p, Mn 2p, Te 3d and O1s. The full scan spectra indicate the presence of expected ions in the compound. The spectrum for copper presents two peaks at 934.5 eV and 954.5 eV for Cu $2p_{3/2}$ and Cu $2p_{½}$ with their corresponding satellites suggesting 2+ valency of Cu. Mn 2p core spectra is shown to possess binding energy at 641.1 eV and 652.9 eV for Mn $2p_{3/2}$ and Mn $2p_{1/2}$ respectively indicating its existence as Mn^{2+} [179–183] Tellurium spectrum display characteristic binding energy for Te^{6+} with Te $3d_{5/2}$ peak at 576.3 eV and Te $3d_{3/2}$ at 586.7 eV. The O 1s spectrum represents splitting similar as observed for earlier compounds with lattice oxygen at 530.3 eV and surface/defect oxygen at 532.1 eV.

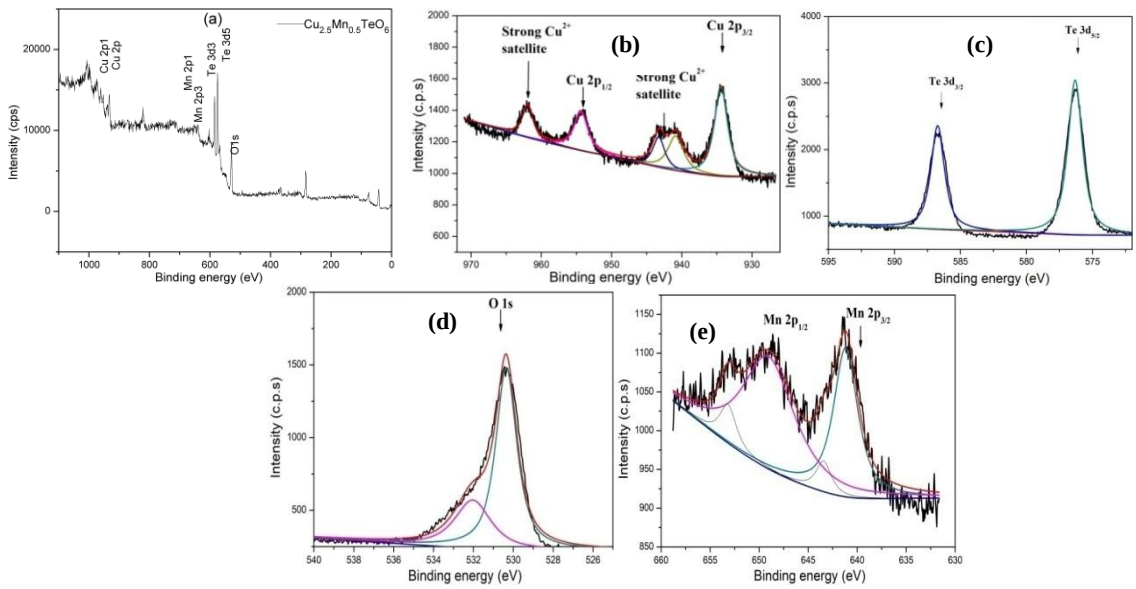

Fig. 4.47 XPS scan for $Cu_{2.5}Mn_{0.5}TeO_6$ *showing (a) full scan (b) Cu 2p (c) Te 3d (d) O 1s (e) Mn 2p peaks.*

4.8.5 Zinc doped Cu_3TeO_6

The XPS analysis spectra for the $Cu_{2.7}Zn_{0.3}TeO_6$ compound are presented in Fig. 4.48 along with full scan spectrum, which reveals the presence of anticipated elements. The Cu core spectra represent two peaks at 934.5 eV and 954.4 eV corresponding to Cu $2p_{3/2}$ and Cu $2p_{1/2}$ respectively with their satellites at 942.6 eV and 962.5 eV respectively confirming its oxidation state as 2+. The binding energy peak for Zn $2p_{3/2}$ is positioned at 1021.5 eV which is expected to be a peak for 2+ oxidation state of Zn ion as mentioned in the literature [55,184]. Te exhibits +6 oxidation states as evident from the XPS spectrum with binding energies of 576.4 eV and 586.7 eV for Te $3d_{5/2}$ and Te $3d_{3/2}$ respectively. Oxygen spectrum is found to show a slightly different peak from its usual pattern. The binding energies for lattice oxygen and defect oxygen at observed at 530.3 eV and 532.2 eV respectively with enhanced surface oxygen peak as observed from the spectrum. Hence, it is considered to possess high oxygen content at the surface due to a greater amount of oxygen vacancies [178].

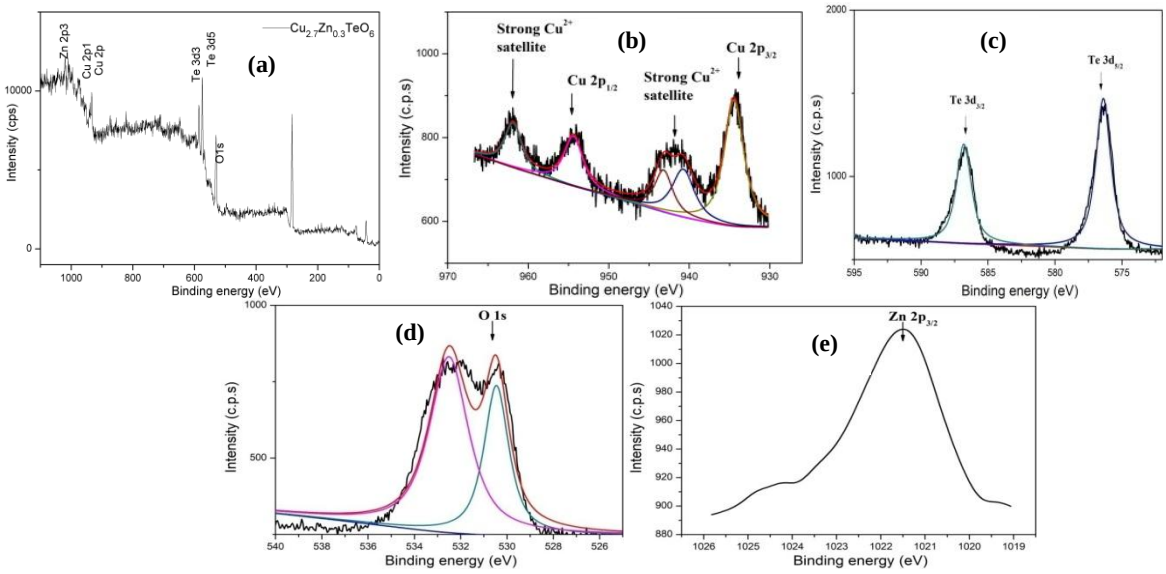

Fig. 4.48 XPS scan for $Cu_{2.7}Zn_{0.3}TeO_6$ *showing (a) full scan (b) Cu 2p (c) Te 3d (d) O 1s (e) Zn 2p peaks.*

4.8.6 Tungsten doped Cu_3TeO_6

Fig. 4.49 represents XPS spectra for W doped copper tellurate, i.e. $Cu_3W_{0.1}Te_{0.9}O_6$ compound consisting of full scan spectrum which provide information on the elements present and other individual element spectra. Spectrum for Cu 2p shows two major peaks for Cu $2p_{3/2}$ and Cu $2p_{1/2}$ at 934.9 eV and 954.8 eV respectively accompanied with their respective satellites at 942.6 eV and 962.6 eV. This conveys the occurrence of copper as Cu^{2+}. The peaks for tungsten are observed at 35.6 eV and 37.7 eV for W $4f_{7/2}$ and W $4f_{5/2}$, which are found to coincide with the values for W^{6+} in the literature [185] remarking the valence of tungsten as W^{6+} in the present system. The fitting of Te 3d spectrum shows two distinct peaks at 576.7 eV and 587.3 eV for Te $3d_{5/2}$ and Te $3d_{3/2}$ resulting in Te^{6+}. The O 1s spectra as usual hold one peak for lattice oxygen at 530.8 eV accompanied with a hump for defect oxygen at 532.0 eV.

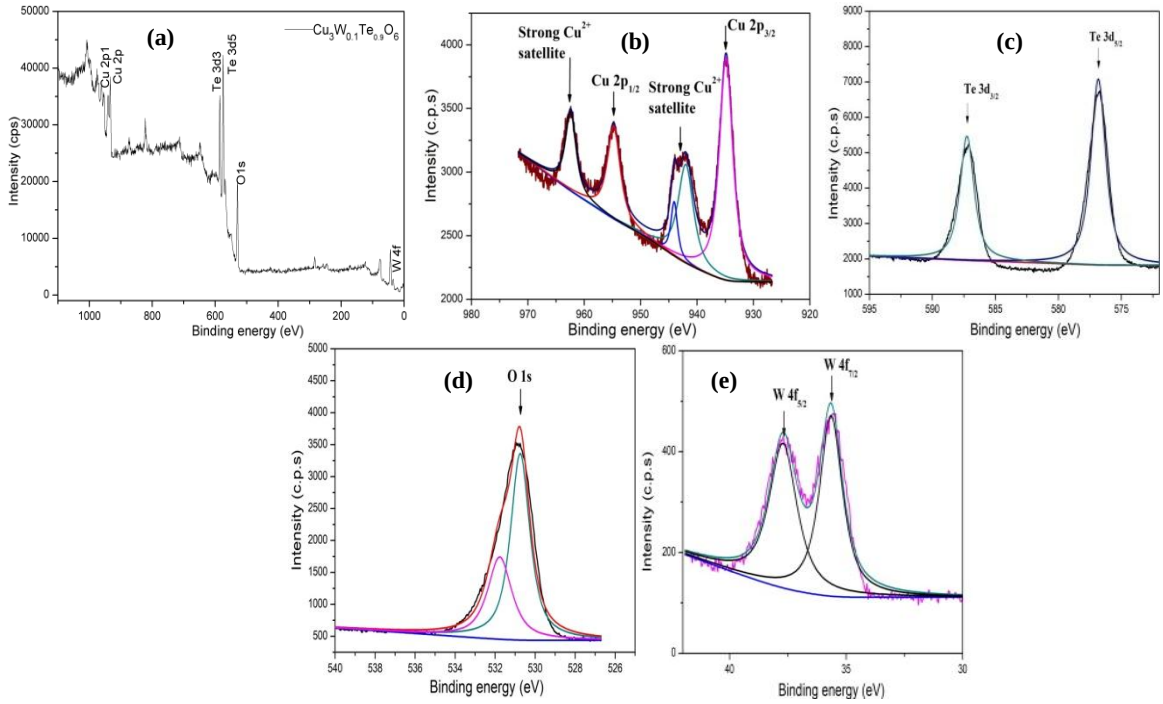

Fig. 4.49 XPS scan for $Cu_3W_{0.1}Te_{0.9}O_6$ *showing (a) full scan (b) Cu 2p (c) Te 3d (d) O 1s (e) W 4f peaks*

4.8.7 Molybdenum doped Cu_3TeO_6

The XPS analysis of $Cu_3Mo_{0.1}Te_{0.9}O_6$ compound confirms the presence of Cu, Mo, Te and O in the full scan spectrum as depicted in Fig. 4.50. Cu $2p_{3/2}$ peak for copper is observed at 934.4 along with its satellites at 943 eV, which affirms its 2+ valency. The peaks for molybdenum are observed at 232.3 eV and 235.4 eV for Mo $3d_{5/2}$ and Mo $3d_{3/2}$ respectively, which are characteristic peaks for Mo^{6+} [186,187] The Te 3d core spectrum shows two distinct peaks at 576.6 eV and 587 eV for Te $3d_{5/2}$ and Te $3d_{3/2}$ respectively for Te^{6+}. The O 1s spectra show the presence of peak for lattice oxygen and defect oxygen.

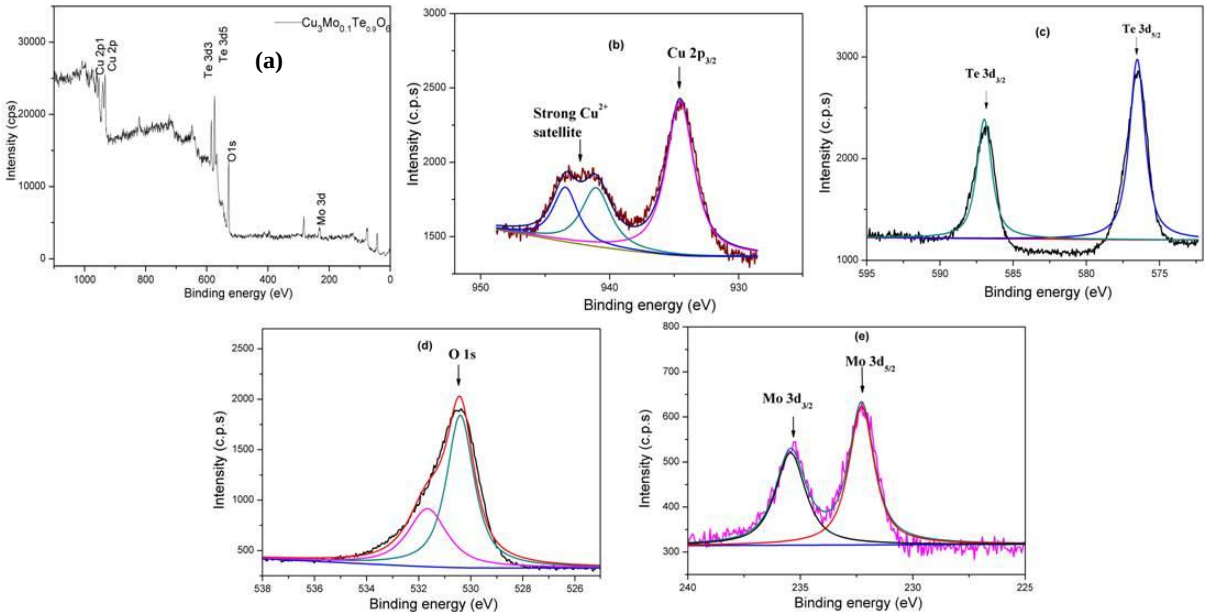

Fig. 4.50 XPS scan for $Cu_3Mo_{0.1}Te_{0.9}O_6$ *showing (a) full scan (b) Cu 2p (c) Te 3d (d) O 1s (e) Mo 3d peaks*

4.8.8 Silver doped Cu_3TeO_6

Properties of materials are dependent on the presence of electrons in a system which is decided by the valency of a particular ion. Hence, XPS of synthesized compounds is a necessary step in order to obtain the oxidation states in a material. XPS analysis was carried out on the $Cu_{2.9}Ag_{0.1}TeO_6$ compound as shown in Fig. 4.51 which exposed the elemental information in the compound through a full scan spectrum. The individual spectrum for Cu showed the presence of Cu as Cu^{2+} as a result of peaks at 934.7 eV and 954.6 eV respectively for Cu $2p_{3/2}$ and Cu $2p_{1/2}$ and their respective satellites at 942.5 eV and 962.3 eV. The 3d core spectrum for silver shows two individual peaks at 366.5 eV and 372.5 eV for $3d_{5/2}$ and $3d_{3/2}$ respectively. These values are observed to shift to a lower binding energy, compared to that for metallic silver [188,189] which suggest that Ag is present in +1 oxidation state. The Te 3d core spectrum shows two distinct peaks for Te $3d_{5/2}$ and Te $3d_{3/2}$ for Te^{6+}. The O 1s spectra as usual hold one peak for lattice oxygen at 530.9 eV accompanied with a bigger hump for defect oxygen at 532.7 eV suggesting presence of surface oxygen to a higher extent.

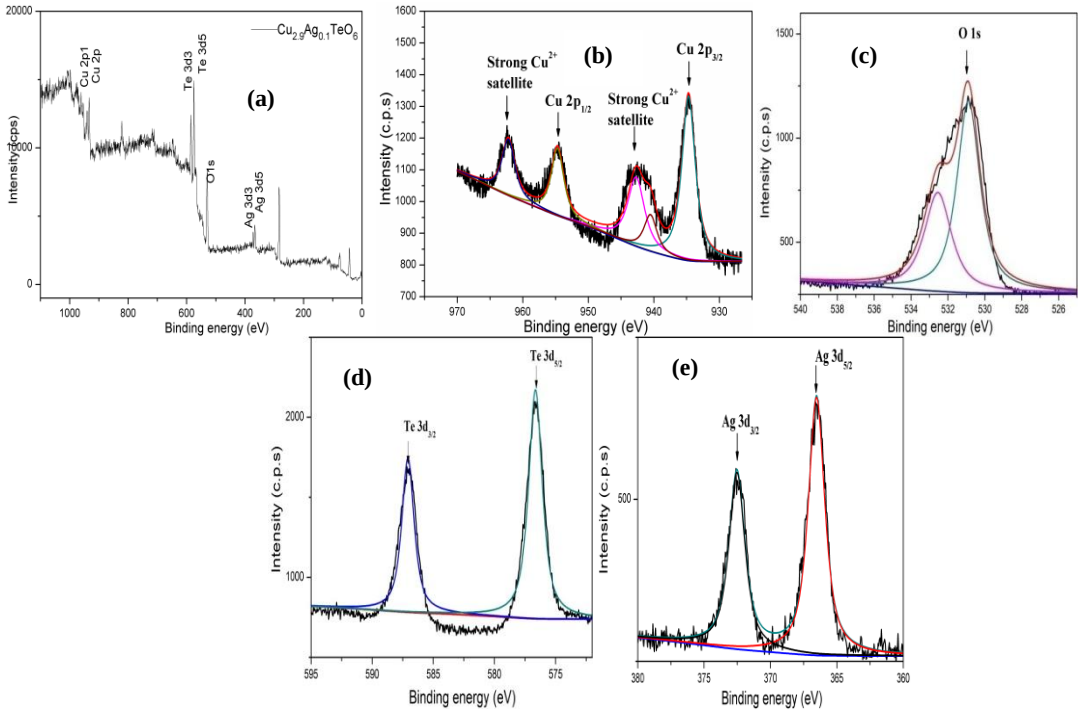

Fig. 4.51 XPS scan for $Cu_{2.9}Ag_{0.1}TeO_6$ *showing (a) full scan (b) Cu 2p (c) Te 3d (d) O 1s (e) Ag 3d peaks.*

4.8.9 Pristine Ni_3TeO_6

Fig. 4.52 represents XPS spectra for pristine Ni_3TeO_6 along with a full scan of sample showing of Ni (2p), O (1s) and Te (3d) elements. XPS spectrum of nickel for pristine nickel tellurate is shown to present two signals for Ni ($2p_{3/2}$) and Ni ($2p_{1/2}$) at 855.4 eV and 873.5 eV respectively along with a strong Ni^{2+} satellite at ~ 861.5 eV and 879.7 eV respectively. These are the characteristic features of Ni^{2+}. Te (3d) spectra of Ni_3TeO_6 (Fig. 4.52) shows the presence of two peaks at 576.2 eV (Te $3d_{5/2}$) and 586.6 eV (Te $3d_{3/2}$) which approach in between valence states of tellurium (Te^{6+} and Te^{4+}) perhaps in 1:1 ratio. XPS spectra of O (1s) shows a characteristic peak at 530.2 eV for lattice oxygen along with a shoulder peak at ~ 531.2 eV which is

observed due to surface oxygen or defect oxygen [170,171] (Fig. 4.52). No other impurity peak was observed, which confirmed the purity of pristine nickel tellurate.

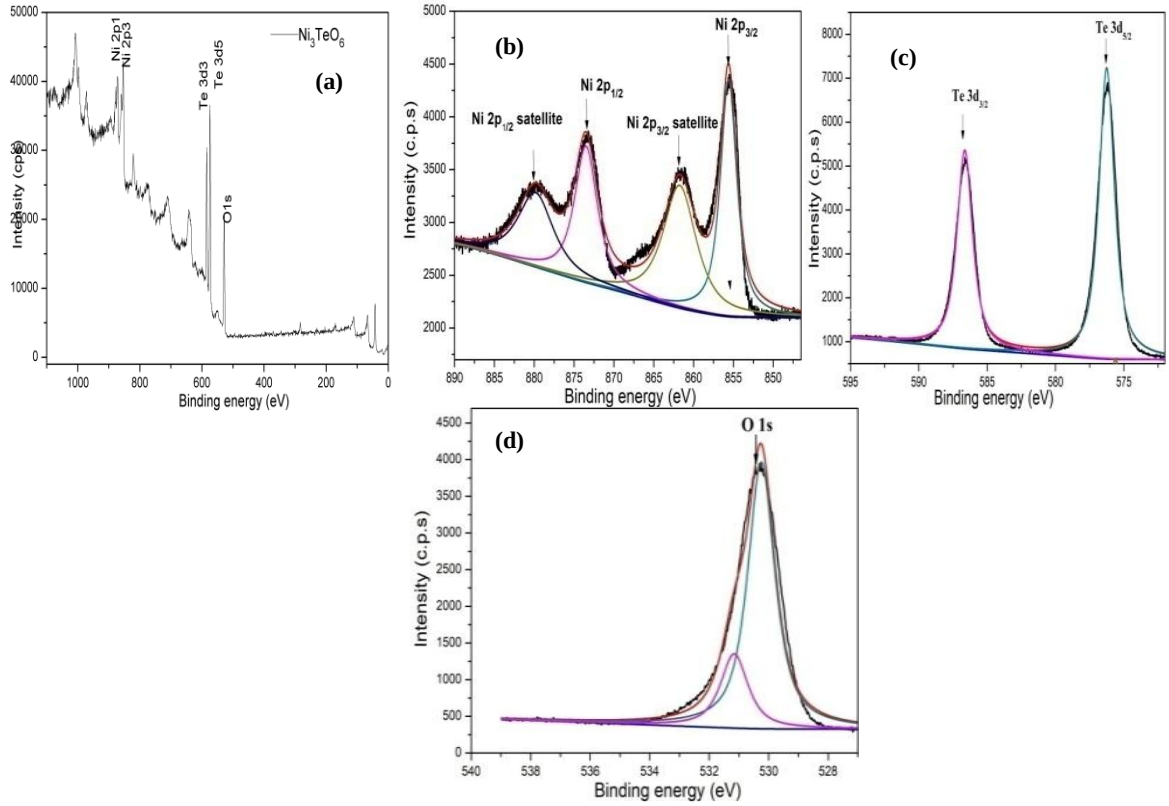

Fig. 4.52 XPS scan for pristine Ni_3TeO_6 showing (a) full scan (b) Ni 2p (c) Te 3d (d) O 1s peaks.

4.8.10 Pristine Fe_2TeO_6

The high-resolution XPS spectra for pristine iron tellurate are depicted in Fig. 4.53. The full scan spectrum shows the presence of all three elements and no other species indicating purity on the prepared material. The spectrum for Fe 2p shows the presence of two peaks at 711.3 eV for Fe $2p_{3/2}$ and at 725.2 eV for Fe $2p_{1/2}$ in presence of their respective satellites as shown in the figure. This conveys that Fe is present as Fe^{3+} [190–192]. The fitting of Te 3d spectrum shows two distinct peaks at 576.2 eV and 586.6 eV for Te $3d_{5/2}$ and Te $3d_{3/2}$ accountable for Te^{6+}. The O 1s spectra as usual hold one peak for lattice oxygen at 530.1 eV accompanied with a hump for defect oxygen at 531.2 eV.

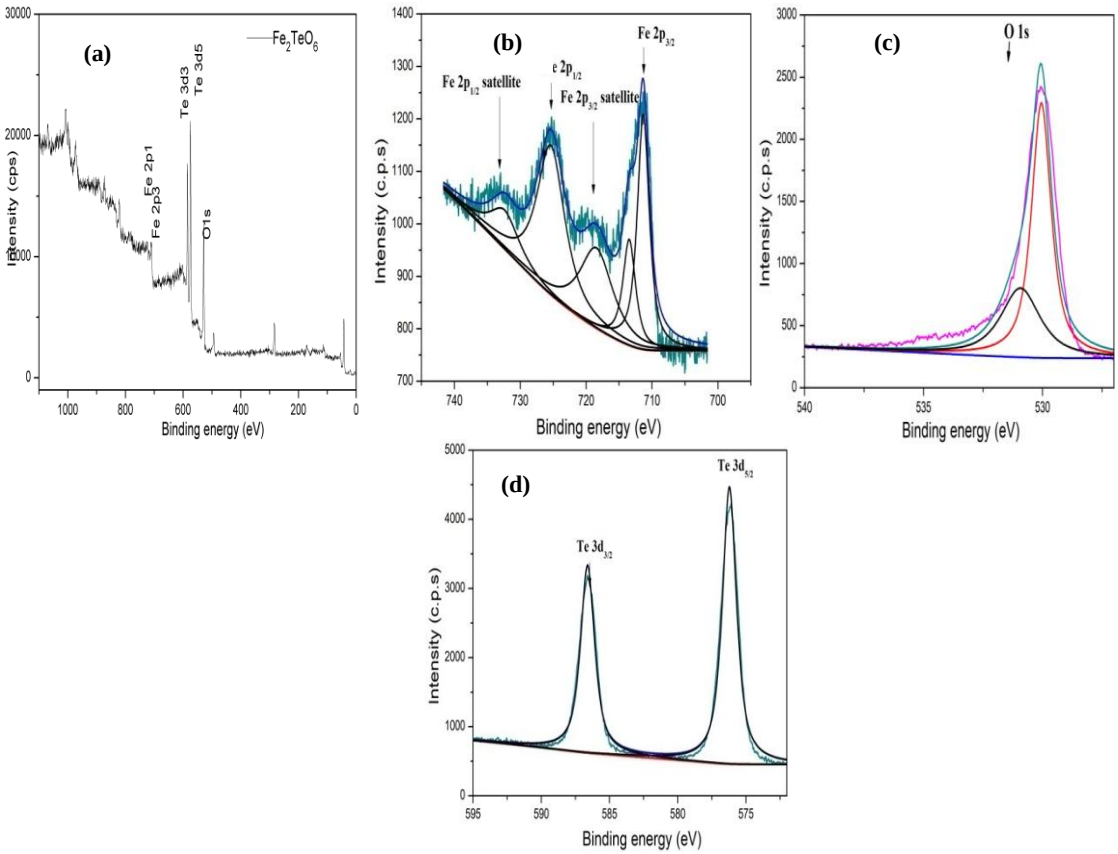

Fig. 4.53 XPS scan for pristine Fe_2TeO_6 showing (a) full scan (b) Fe 2p (c) Te 3d (d) O 1s peaks

4.8.11 Pristine Al_2TeO_6

The high-resolution XPS spectra for pure aluminium tellurate are displayed in Fig. 4.54 which discloses the presence of elements in the sample as evident from the full scan spectrum. The Al 2p peak at 74 eV substantiates its +3 oxidation state [178,193]. The prominent Te peaks at 576.6 eV and 587.0 eV represent Te^{6+}. XPS spectra of O (1s) shows a characteristic peak at 531.2 eV for lattice oxygen along with a shoulder peak at ~ 532.4 eV which is observed due to surface oxygen or defect oxygen which are observed to a larger extent.

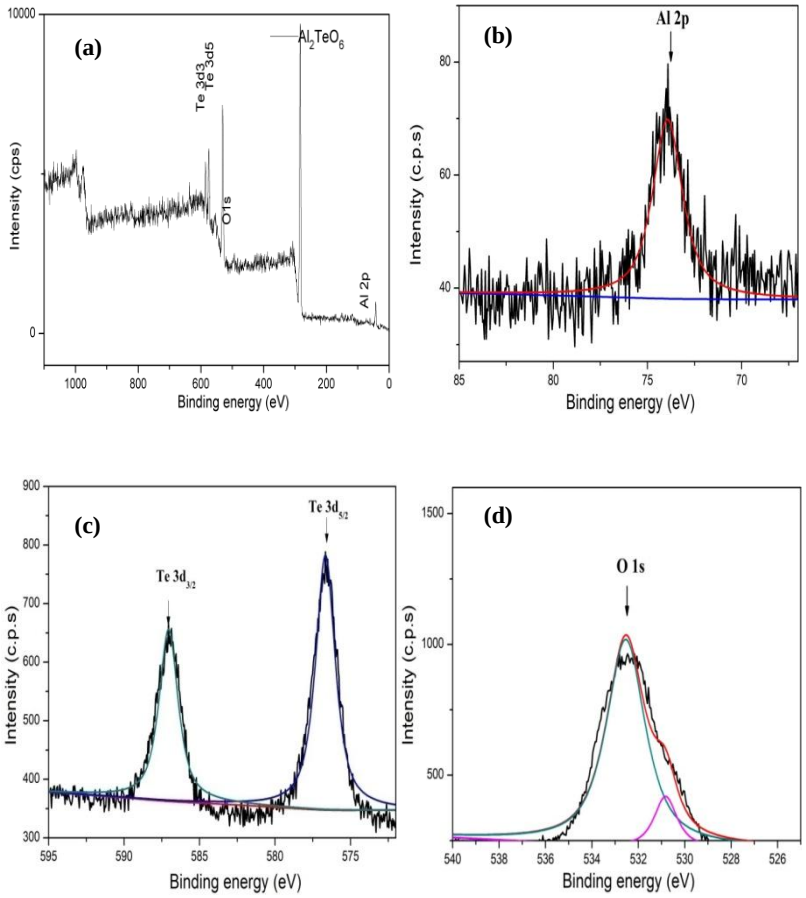

Fig. 4.54 XPS scan for pristine Al_2TeO_6 showing (a) full scan (b) Al 2p (c) Te 3d (d) O 1s peaks

Chapter 5

Material studies and other investigations

Tellurates are accounted to possess distinct properties which depend on various factors such as method of preparation, particle size, structure etc. causing modification of the compound. It is thus, interesting to study the properties in detail and understand more about compounds containing tellurium.

5.1 Electrical resistivity (ρ)

By co-precipitation method

5.1.1 $Cu_{3-x}Co_xTeO_6$ (x=0.1 – 0.5)

Compounds with resistivity properties are significantly important in the fields of electronics and electrical devices. All the prepared tellurate compounds are found to exhibit the property of electronic conduction on thermal application. The set-up for electrical resistivity measurement includes a resistivity cell comprising of electrodes in the form of two plates for electrical conduction, between which is placed a sample in the form of a round cylindrical pellet pressed under pressure of 3 tons and sintered. This sample is placed between the electrodes and is applied to a fix voltage value. This provides us with the current which is obtained with the help Keithley meter and the cell is subjected to temperature controlled furnace at a constant rate of 2 ° per minute, up to 450 °C. The current is recorded for every 5-degree rise in temperature. Current measurements are carried out during the cooling cycle as well. All measurements were carried out in the air. As observed in Fig. 5.1, the results present two distinct regions of conduction. A temperature stable resistivity region at the lower side, whereas at a higher temperature, we find that the conductivity increase rapidly. The temperature stable region could be due to the insulator type conduction since; there is no much flow of current with the rise in temperature which suggests that the wide band gap of tellurates responsible for this behavior. A transition from insulator to semiconductor type conduction is then observed as we move to a higher temperature. The

thermal conduction of electrons is observed with the rise in temperature with a sudden increase in conduction at a certain temperature point. The cooling cycle for all the compounds also shows similar behavior. This suggests that tellurates are a high-temperature semiconductor. All the compounds show similar behavior for resistivity plot, whereas the values differ in the semiconductor region and are found to increase on doping.

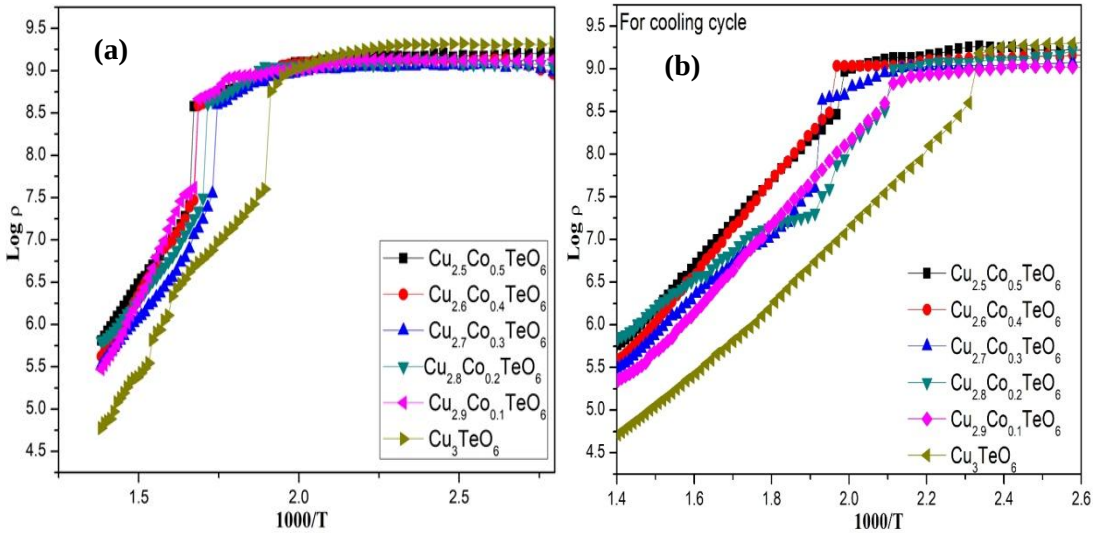

Fig. 5.1 Plot of log resistivity v/s 1000/T for $Cu_{3-x}Co_xTeO_6$ (x=0.1 – 0.5) in air for (a) heating and (b) cooling cycles.

Same studies were carried out in a N_2 atmosphere to check the interference of air if any. Fig. 5.2 shows the result of this analysis, both heating as well as cooling cycle displayed similar behaviour to that obtained in the air which reflected their natural phenomena happening as a material property, irrespective of the atmosphere around it.

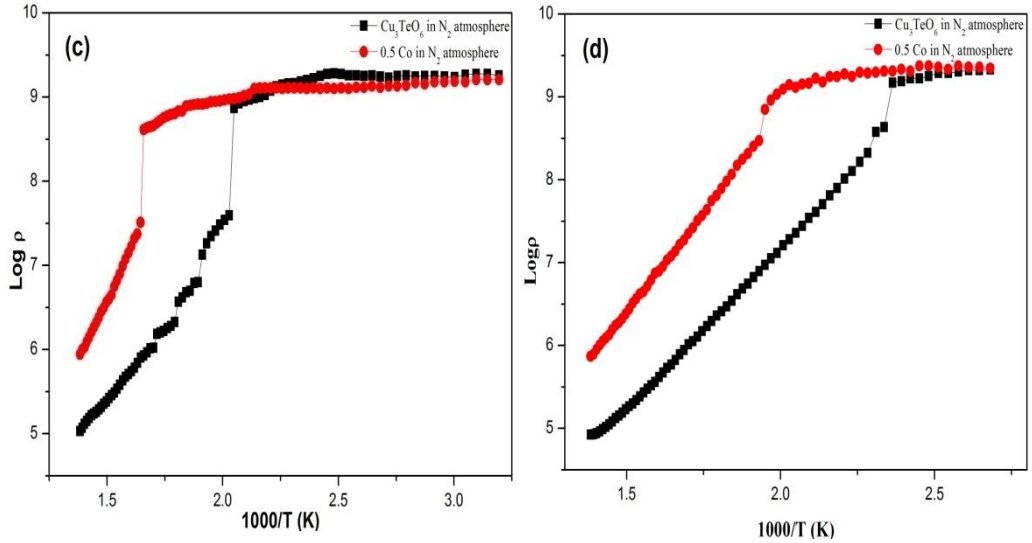

Fig. 5.2 Plot of log resistivity v/s 1000/T for representative samples of $Cu_{3-x}Co_xTeO_6$ (x=0 and 0.5) in N_2 for (c) heating and (d) cooling cycles.

5.1.2 $Cu_{3-x}Ni_xTeO_6$ (x=0.1 – 0.5)

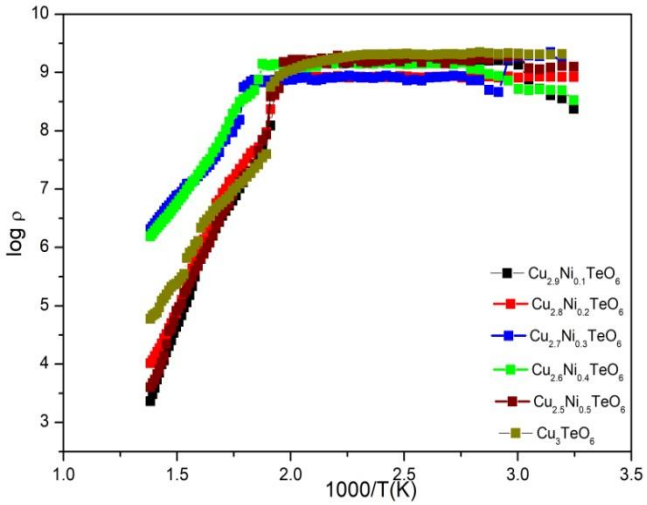

Fig. 5.3 Plot of log resistivity v/s 1000/T for $Cu_{3-x}Ni_xTeO_6$ (x=0.0 – 0.5) in air.

Fig. 5.3 presents a series of resistivity plots for nickel doped copper tellurate compounds carried out in air from room temperature to 450 °C. There appear two distinct regions; one towards the lower side of temperature which behaves like an insulator and the other semiconductor which lies at a higher temperature. The resistivity of a material remains stable

up to around 250 °C and then increases sharply at high temperature. It is also noticed here that, in the insulator type region, the value of resistivity is almost same for all the compositions of tellurates. Whereas the semiconductor region show varied resistivity values as they approach higher temperature. $Cu_{2.7}Ni_{0.3}TeO_6$ and $Cu_{2.6}Ni_{0.4}TeO_6$ show the highest values of resistivity among all others, followed by the pristine copper tellurate. Rest of the compositions are found to lie at lower values of resistivities. In other words, $Cu_{2.7}Ni_{0.3}TeO_6$ and $Cu_{2.6}Ni_{0.4}TeO_6$ serve as the optimum concentrations for high resistivity.

5.1.3 $Cu_{3-x}Zn_xTeO_6$ (x=0.2 and 0.5)

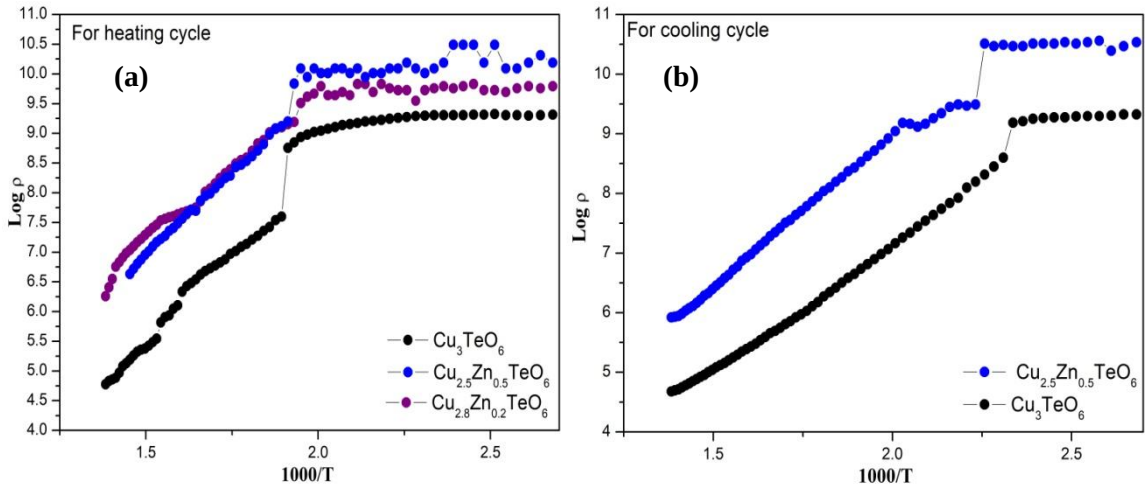

Fig. 5.4Plot of log resistivity v/s 1000/T for $Cu_{3-x}Zn_xTeO_6$ (x=0.2 and 0.5) in air (a) heating and (b) cooling cycles.

The electrical resistivity of zinc doped copper tellurate is displayed in the above Fig. 5.4 for heating as well as cooling cycles. It is very interesting to know that this series also present a similar pattern for resistivity as observed for other compounds mentioned above. Initially, there is an insulator type behavior seen with respect to temperature till a certain temperature, which suddenly changes to semiconductor type on heating. Both heating, as well as cooling studies, showed similar behavior in these compounds. However, we see that there is an

increase in the resistivity values on doping Zn in copper tellurate. This could probably be due to the defect caused on doping Zn [194].

5.1.4 $Cu_{3-x}Ag_xTeO_6$ (x=0.1) *by co-precipitation method*

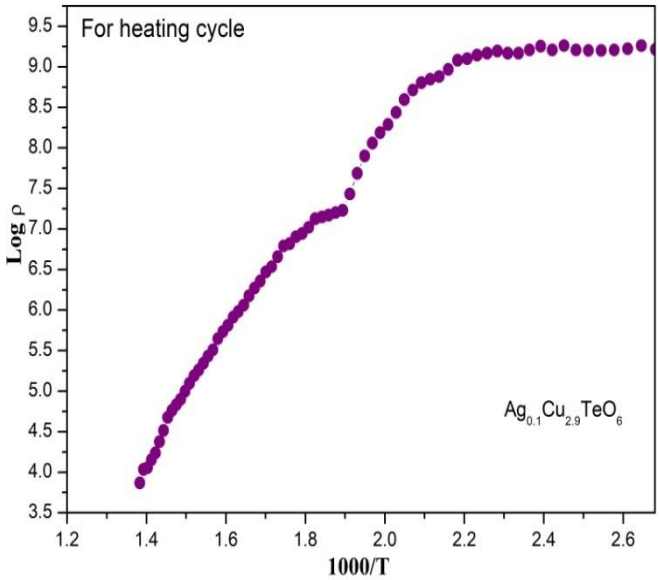

Fig. 5.5 Plot of log resistivity v/s 1000/T for $Cu_{3-x}Ag_xTeO_6$ (x=0.1) sintered in air.

Silver doped copper tellurate compound has been studied for resistivity in air from room temperature to 450 °C, as shown in Fig. 5.5. It shows a constant value of resistivity with an increase in temperature up to a certain value, indicating insulator type behavior which changes soon to semiconductor type indicated by a slow decrease in resistivity with a further rise in temperature unlike pristine sample of copper tellurate. This compound shows more of a semiconductor like nature and less of an insulator like property at the initial temperature.

5.1.5 $Cu_3Mo_xTe_{1-x}O_6$ (x=0.1, 0.2) *by co-precipitation method*

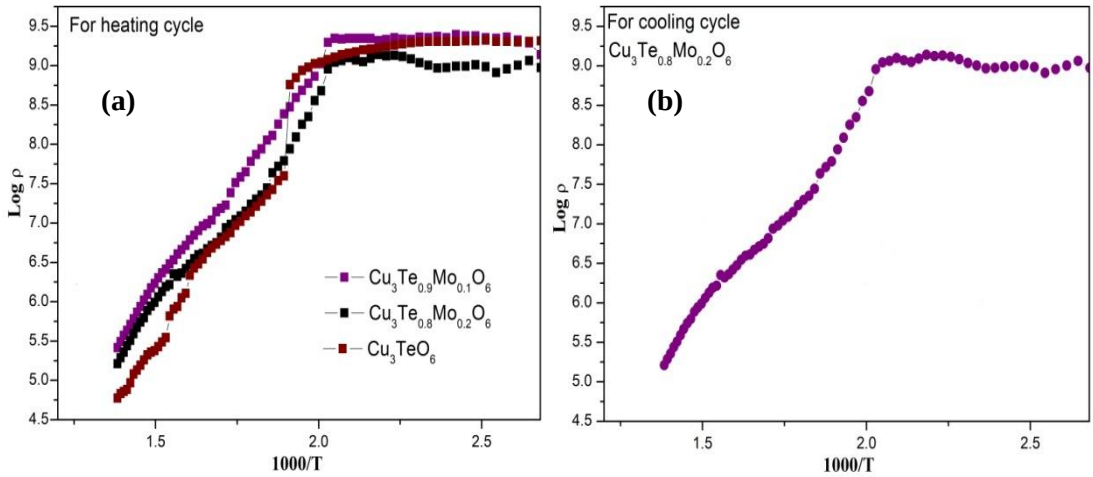

Fig. 5.6 Plot of log resistivity v/s 1000/T for $Cu_3Mo_xTe_{1-x}O_6$ (x=0.1, 0.2) in air for (a) heating and (b) cooling cycle.

Tellurates, with tellurium substitution by molybdenum, has been studied for electrical properties from room temperature to 450 °C in air. Fig 5.6 shows the electrical behaviors of Mo-doped copper tellurates with similar patterns matching with those of other copper doped tellurates. There is no effect of temperature observed on the resistivity of samples, initially at low temperature displaying insulator character with resistivity values lying in the almost the same range. The pristine sample is found to hold the insulator form for slightly longer temperature than the other compounds. Sudden diversion from an insulator to semiconductor form is observed as the temperature increased with faintly higher resistivity values for molybdenum doped than pristine at a higher temperature. The cooling process for electrical resistivity study also shows similar results.

5.1.6 Ni_3TeO_6 *by co – precipitation method*

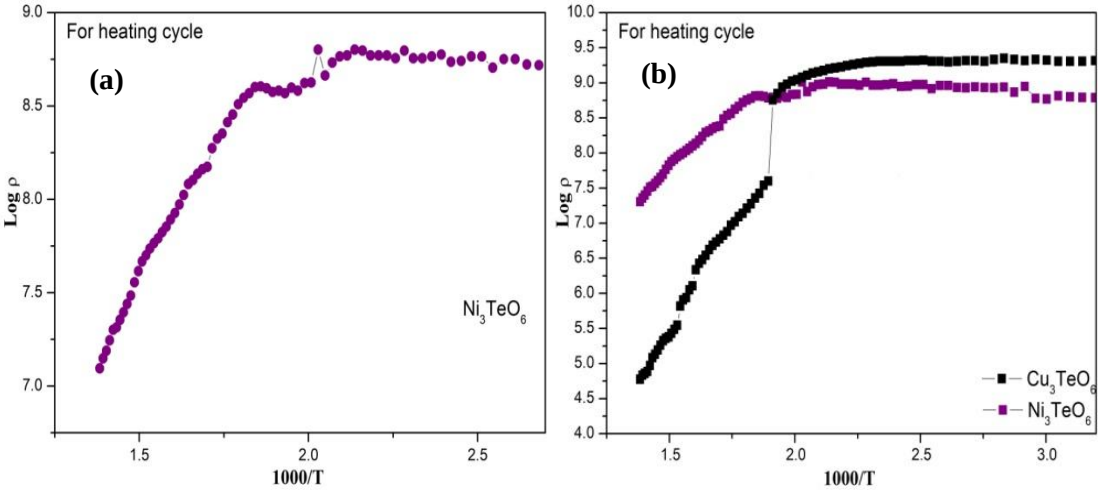

Fig. 5.7 Plot of log resistivity v/s 1000/T for (a) Ni_3TeO_6 and (b) comparison between Ni_3TeO_6 and Cu_3TeO_6.

Pristine nickel tellurate prepared by simple co-precipitation method was studied for its electrical properties and was found to show an insulating type pattern at lower values of temperature which changed to semiconductor type at a higher temperature as usual (Fig. 5.7 a). The study was carried out from room temperature to 450 °C in air. When compared with copper tellurate (Fig. 5.7 b), it is seen that the temperature dependent resistivity at higher temperature rolls down in a smooth fashion than that of copper tellurate, which abruptly falls down presenting its high conductivity at high temperature.

5.1.7 $Ni_3Te_{1-x}M_xO_6$ (x= 0.0, 0.2 and M = W, Mo) *by co – precipitation method*

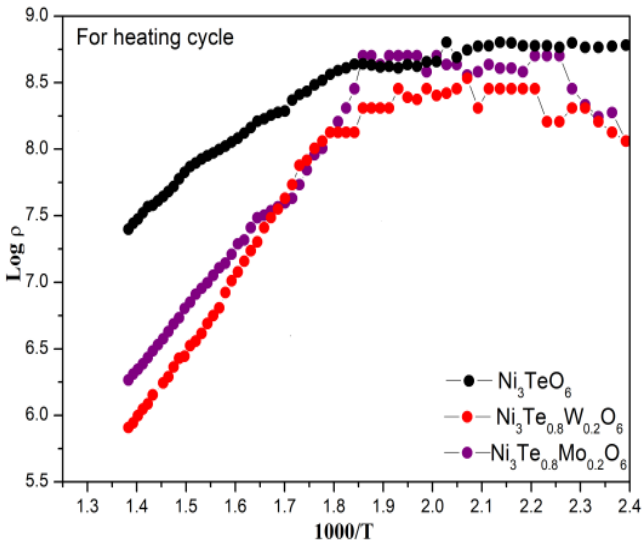

Fig. 5.8 Plot of log resistivity v/s 1000/T for $Ni_{3-x}M_xTeO_6$ (M=W and Mo, x=0.2) in air.

Tungsten and molybdenum doped nickel tellurate compounds were studied for their resistivity property as depicted in Fig. 5.8. All presented plots show a similar pattern for their electrical property, i.e. insulator at lower temperature and semiconductor at higher. Amongst all, pristine nickel tellurate possesses higher resistivity followed by Mo-doped nickel tellurate. W doped nickel tellurate show resistivity slightly lower than the Mo-doped compound. W and Mo-doped nickel tellurate at initial temperatures show an increase in resistivity with the rise in temperature, which could be due to the presence of moisture on the sample surface.

5.1.8 $Ni_{3-x}Zn_xTeO_6$ (x = 0.0, 0.2, 0.3 and 0.5) *by co – precipitation method*

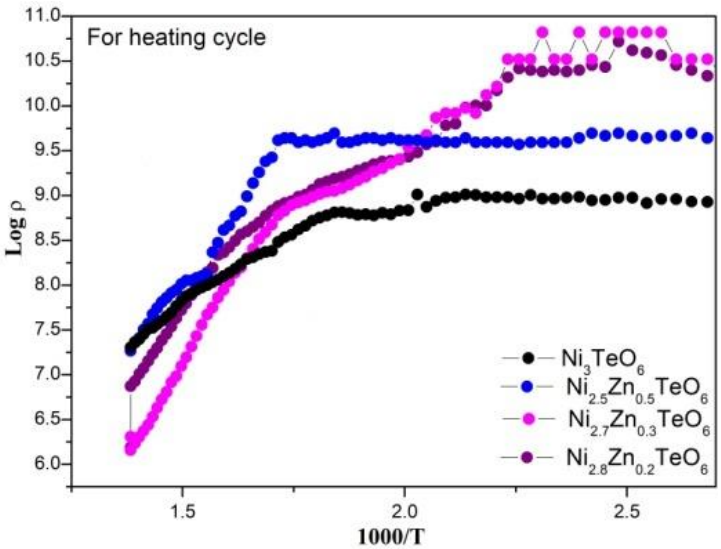

Fig. 5.9 Plot of log resistivity v/s 1000/T for $Ni_{3-x}Zn_xTeO_6$ (x=0.2, 0.3, 0.5) sintered in air.

Zinc-doped nickel tellurates are investigated for electrical properties as shown in Fig. 5.9. Towards lower dopant concentration, the pattern is slightly deviated, with more of the semiconductor region whereas, the highest doped compound along with the pristine show typical insulator to the semiconductor region. All the doped compositions are found to show higher resistivity than the pristine nickel tellurate.

5.1.9 $Ni_{3-x}Co_xTeO_6$ (x = 0.3) *by co-precipitation method*

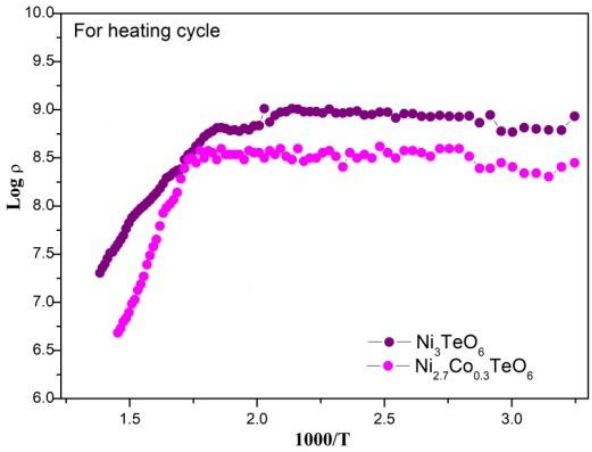

Fig. 5.10 Plot of log resistivity v/s 1000/T for $Ni_{3-x}Co_xTeO_6$ (x=0.3) in air.

Log of resistivity v/s temperature study for $Ni_{2.7}Co_{0.3}TeO_6$ is shown in Fig. 5.10 which is clearly found to show insulator – semiconductor behavior. It is obvious from the figure that pristine nickel tellurate possesses a slightly higher resistivity value than the doped compound.

5.1.10 Fe_2TeO_6 and Al_2TeO_6

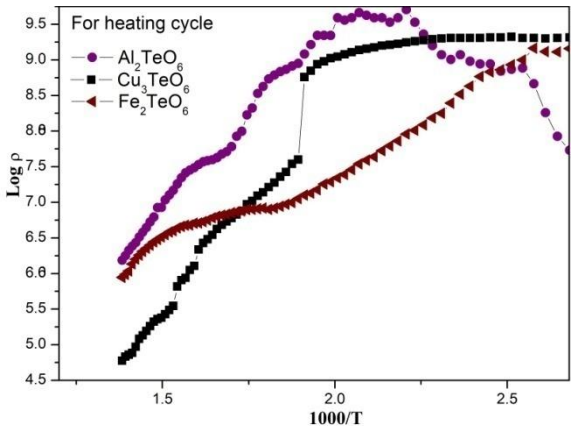

Fig. 5.11 Plot of log resistivity v/s 1000/T for Fe_2TeO_6 and Al_2TeO_6 in air.

Fig. 5.11 presents resistivity plot for Fe_2TeO_6 and Al_2TeO_6 tellurates. Two distinct patterns of resistivity are observed for both. The plot for Fe_2TeO_6 represents typical semiconductor behavior, from room temperature to 450 °C. Whereas, Al_2TeO_6 shows an increase in resistivity up to a certain point of temperature which then decreases till 450 °C showing semiconductor nature. This small increase in resistivity could be attributed to the presence of moisture on the sample surface.

Tellurates prepared by sol – gel method were also studied for their electrical properties. Results obtained are as below:

5.1.11 $Cu_{3-x}Zn_xTeO_6$ (x = 0.1 – 0.4) *by sol – gel method*

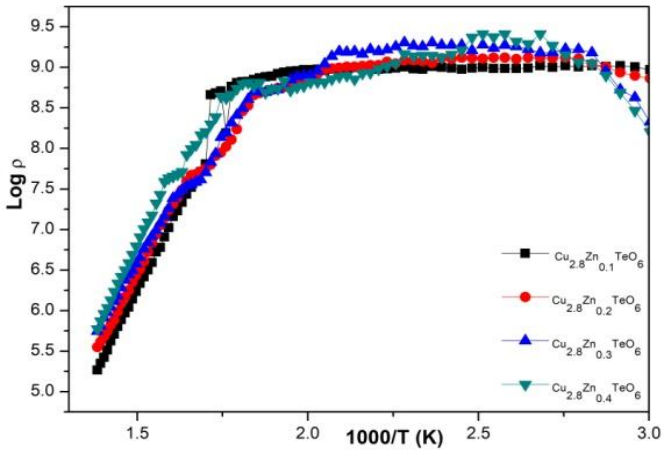

Fig. 5.12 Plot of log resistivity v/s 1000/T for $Cu_{3-x}Zn_xTeO_6$ (x=0.1 - 0.4) in air.

Fig. 5.12 shows zinc doped copper tellurate possessing electrical property. All the compounds show typical insulator to semiconductor nature. The decrease in resistivity with an increase in temperature is observed up to 450 °C showing semiconductor nature of compounds at a higher temperature.

5.1.8 $Cu_{3-x}Ni_xTeO_6$ (x=0.1 – 0.5) *by sol – gel method*

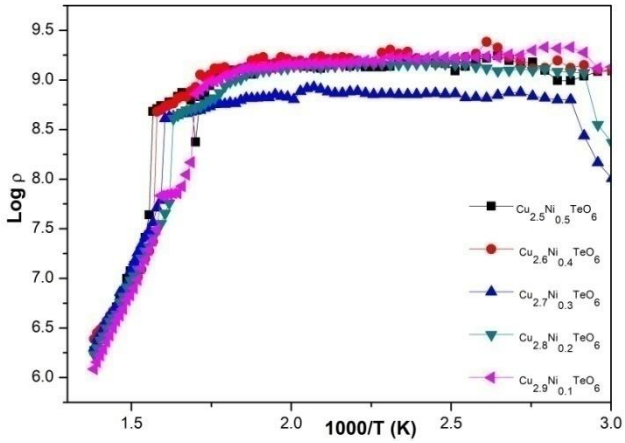

Fig. 5.13 Plot of log resistivity v/s 1000/T for $Cu_{3-x}Ni_xTeO_6$ (x=0.1 – 0.5) sintered in air by co – precipitation method.

The plot of resistivity v/s temperature for nickel doped copper tellurate prepared by the sol-gel method is shown above in Fig. 5.13. At initial temperatures, it is observed to show no change in resistivity with temperature indicating insulator type conduction mechanism, but at a point, a sudden fall in resistivity is observed, from which it starts behaving like semiconductor till 450 °C. This point of sharp change in the conduction mechanism is found to increase with the dopant concentration and could be considered as material's T_c point.

5.2 Vibrating sample magnetometer (VSM)

Tellurates are found to exhibit magnetic domains in their structure and possess antiferromagnetic spin, well below room temperature.

5.2.1 Cu_3TeO_6 (x=0.1 – 0.5) *by co-precipitation method*

Magnetic studies were carried out on Co-doped copper tellurates to understand their magnetic nature under the influence of temperature and magnetic field. Magnetization v/s temperature plot for pristine Cu_3TeO_6 was obtained at 250 Oe magnetic field with varying temperature from 50 to 120 K and was encountered to show antiferromagnetic spins below T_N of around 64 K. The anti-ferromagnetic spin alignment in Cu_3TeO_6 below T_N is supposed to induce a magneto-elastic strain of the lattice wherein, planar neighboring Cu^{2+} hexagons share one common corner and by folding in space, form a complex three-dimensional network [30,45,133]. As shown in Fig. 5.14, magnetization as a function of magnetic field, at room temperature as well as 50 K present a diagonal nature of plot which suggests that the ground state of Cu_3TeO_6 is likely to posses an anti-ferromagnetic ordering at low temperature [46,175]. There is no saturation magnetization observed up to 30000 Oe.

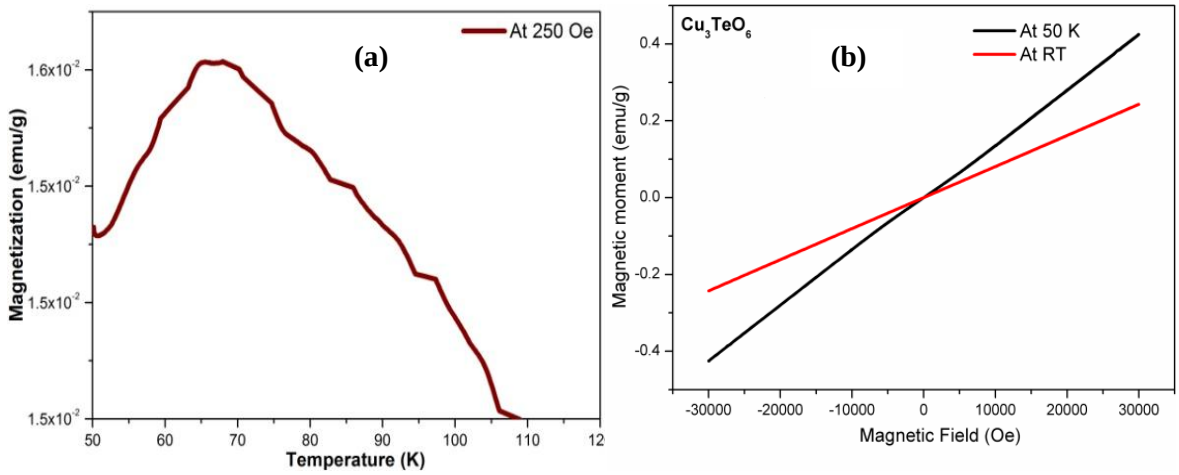

Fig. 5.14 Magnetization versus temperature study on Cu_3TeO_6 sample showing (a) anti-ferromagnetic behaviour below 64 K (Neel Temperature) and (b) Magnetic field versus magnetization study on Cu_3TeO_6 at RT and at 50 K.

5.2.2. $Cu_{3-x}Co_xTeO_6$ (x=0.1 – 0.5) *by co-precipitation method*

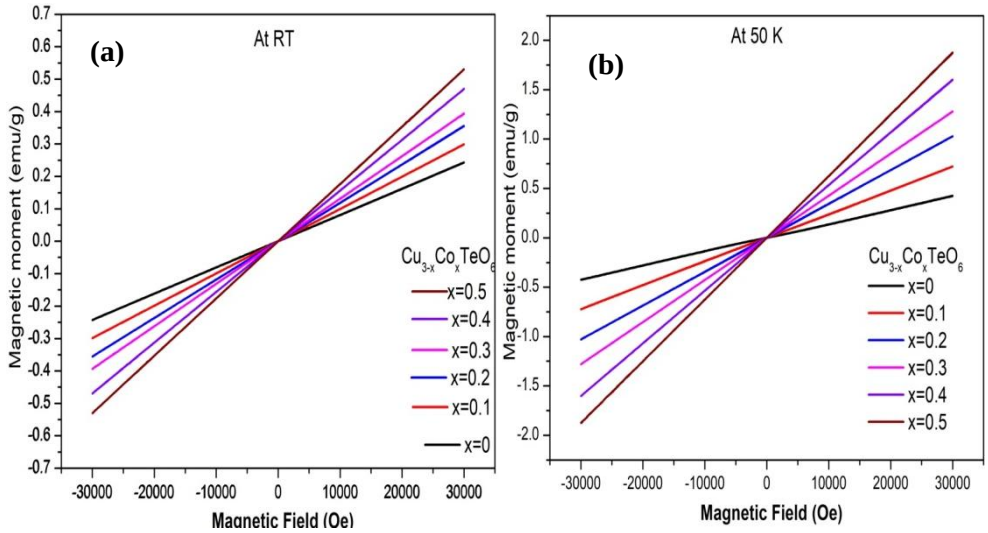

Fig. 5.15 shows magnetization v/s applied magnetic field plots for cobalt doped copper tellurate compounds at (a) room temperature and (b) 50 K.

Fig. 5.15 shows magnetization v/s applied magnetic field plots for cobalt doped copper tellurate compounds at room temperature and 50 K. Observation drawn from the plot suggests that there is no saturation magnetization in the applied magnetic field with the diagonal nature of line implying occurrence of antiferromagnetic spin at low temperature.

Also, it is noticed in both the plots that on doping with cobalt, magnetization increases at extreme sides of the magnetic field as the concentration of Co increases. This is expected to occur as cobalt is a ferromagnetic ion which thus contributes to the magnetization to a certain level in presented series of compounds. It is also noticed that temperature has an effect over the magnetic property of compounds as the values are slightly higher at 50 K than at room temperature.

5.2.3. $Cu_{3-x}Ni_xTeO_6$ (x=0.0, 0.1, 0.3, 0.5, 3.0) *by co – precipitation method*

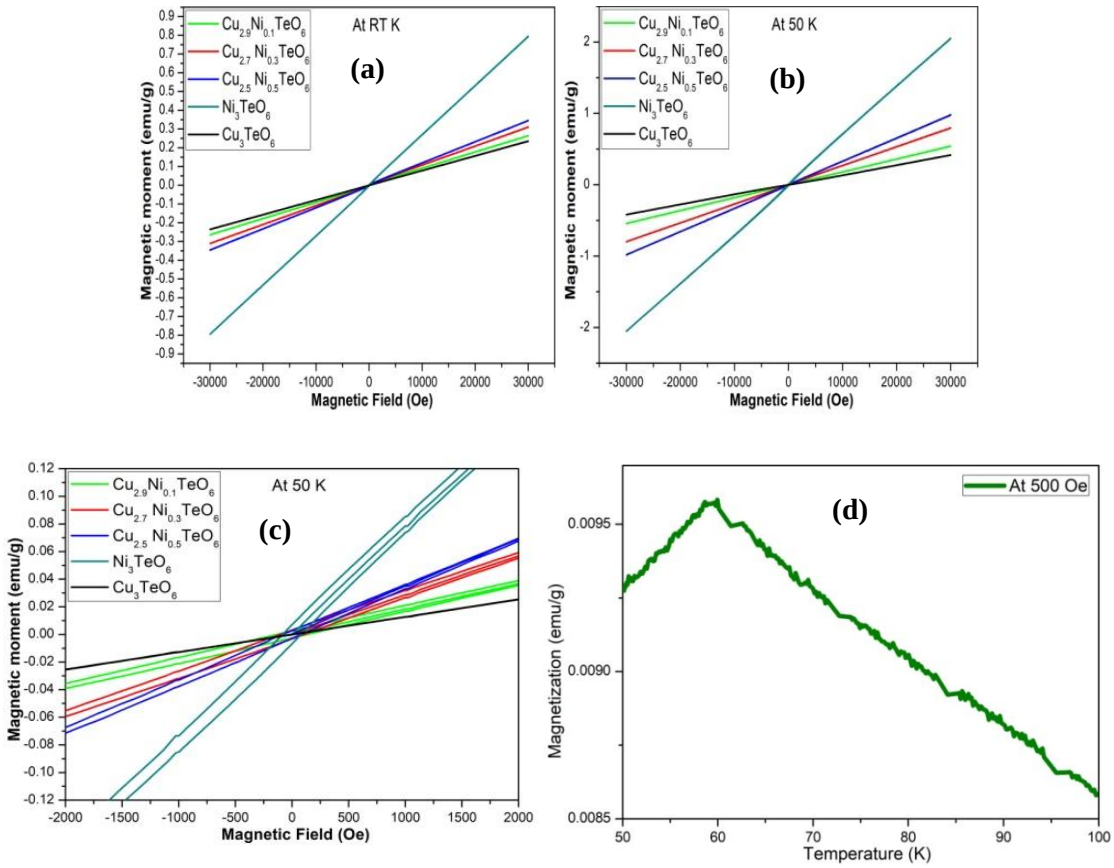

Fig. 5.16 shows magnetization v/s applied magnetic field plots for nickel doped copper tellurate with pristine copper tellurate and nickel tellurate compounds at (a) room temperature and (b) 50 K. The magnified plot for samples at 50 K is presented in (c) whereas (d) shows anti-ferromagnetic behaviour below Neel Temperature.

$Cu_{3-x}Ni_xTeO_6$ (x = 0, 0.1, 0.3, 0.5 and 3) prepared by co-precipitation method were analysed for their magnetic property. Pristine copper tellurate along with nickel tellurate and nickel doped copper tellurate as shown in Fig. 5.16 were found to exhibit a linear variation of M-H curve revealing usual anti-ferromagnetic/paramagnetic spins favorable at low temperature. Saturation magnetization is not observed in the entire range of magnetic field in all compounds. There is an increasing trend in magnetization observed on doping nickel ion in pristine copper tellurate with the highest magnetization for pure nickel tellurate. Since Ni is a ferromagnetic ion, it is supposed to show increment in magnetization as it does. Analyses carried out at 50 K comparatively show higher values than the analyses carried out at room temperature. The enlarged view of the plots at 50 K is presented in Fig. 5.16 c, which exposes prominent hysteresis loop for pure nickel tellurate which is reduced with Ni substitution by copper.

Magnetization with respect to temperature was studied at 500 Oe and the plot represents antiferromagnetic to paramagnetic transition at around 60 K as shown in Fig. 5.16 d.

5.2.4. Fe_2TeO_6 and $Fe_{1.9}Eu_{0.1}TeO_6$

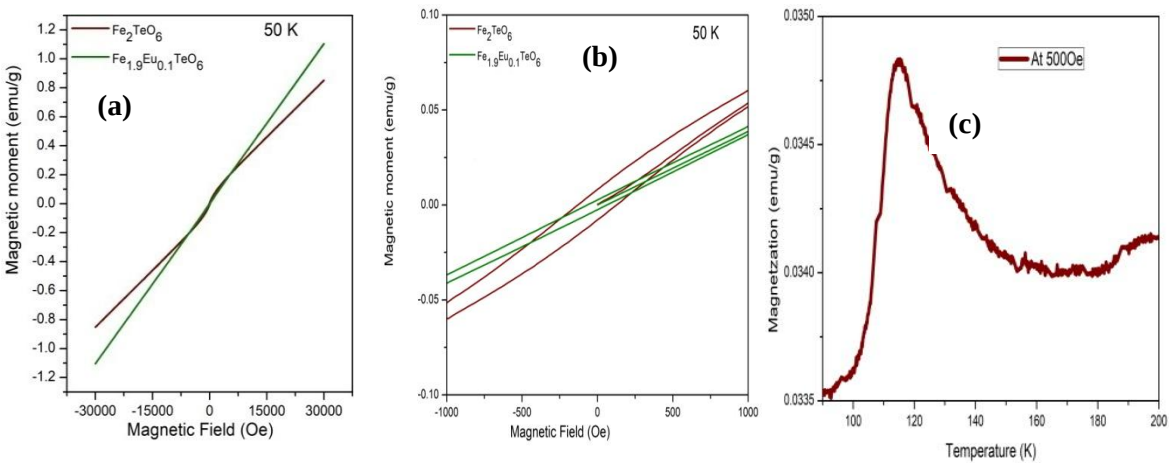

Fig. 5.17 (a) Magnetic field versus magnetization study on pristine and Eu doped Fe_2TeO_6 sample at 50 K (b) magnified plot at 50 K (c) anti-ferromagnetic behaviour below Neel temperature.

Fig. 5.17 represents magnetization v/s magnetic field plots for pure Fe_2TeO_6 and $Fe_{1.9}Eu_{0.1}TeO_6$ at 50 K showing their dependence on the magnetic field. Pristine iron tellurate possesses weak ferromagnetism which is magnified and shown in Fig. 5.17 b, in the lower region of the magnetic field, whereas Eu doped compound present linear pattern of magnetization indicating paramagnetic spins. Weak ferromagnetic nature of iron tellurate sample is lost on doping Eu in its lattice. There is no saturation magnetization observed at the higher side of the field.

Fig. 5.17 c represents magnetization with respect to temperature study at 500 Oe with antiferromagnetic to paramagnetic transition at around 115 K for pristine iron tellurate.

5.2.5. $Cu_{2.9}Fe_{0.1}TeO_6$

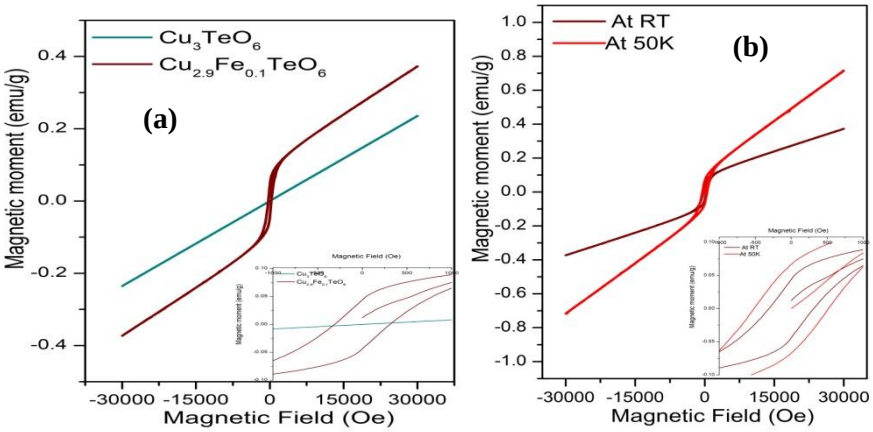

Fig. 5.18 (a) Magnetic field versus magnetization study on pristine Fe doped Cu_3TeO_6 sample at RT with inset showing magnified view of the hysteresis loop (b) M-H plot for Fe doped Cu_3TeO_6 sample at RT and 50 K.

Iron-doped copper tellurate was introduced to induce some magnetism in the pristine copper tellurate which is likely to present a paramagnetic behavior and the results of this are shown above in Fig. 5.19 (a). This figure shows a diagonal pattern of the line for

magnetization v/s magnetic field for pristine copper tellurate, revealing its magnetic behaviour. Whereas, the Fe doped compound present a hysteresis loop possessing weak ferromagnetic behavior which appears prominently in the enlarged view shown in the inset figure. Fig. 5.19 (b) shows magnetization by iron doped copper tellurate, at room temperature, and at 50 K. It is observed that the magnetization is raised at 50 K than at room temperature with wider hysteresis shown at 50 K than at room temperature.

5.2.6. $Cu_{3-x}Mn_xTeO_6$

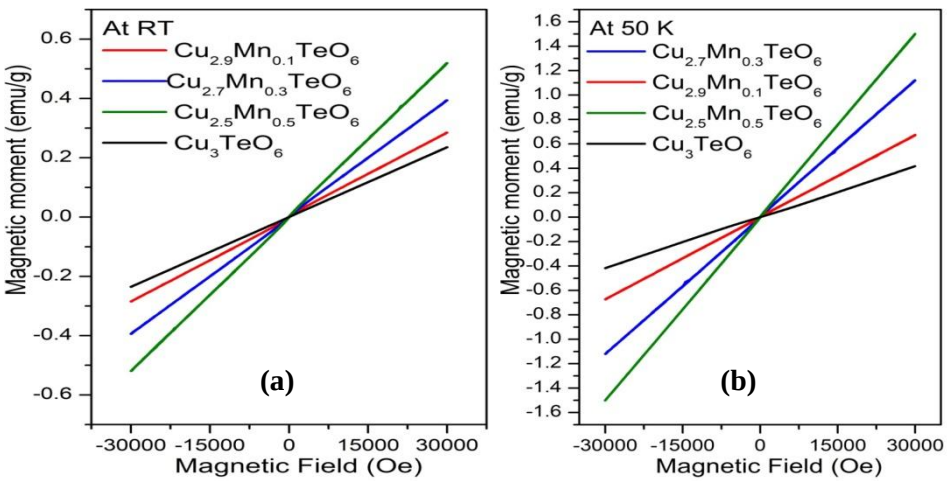

Fig. 5.20 Magnetic field versus magnetization study on pristine Mn doped Cu_3TeO_6 sample at (a) RT and (b) at 50K for Fe doped Cu_3TeO_6 sample.

Manganese doping in the copper tellurate induces magnetization in the doped series, at both room as well as at 50 K as shown in Fig. 5.20. Similar conclusions could be drawn from the above figure. With Mn doping, the magnetization is found to increase linearly with no saturation up to 3 T. M-H studies at 50 K showed a similar trend but a considerable rise in magnetization was observed.

5.2.7. Al_2TeO_6

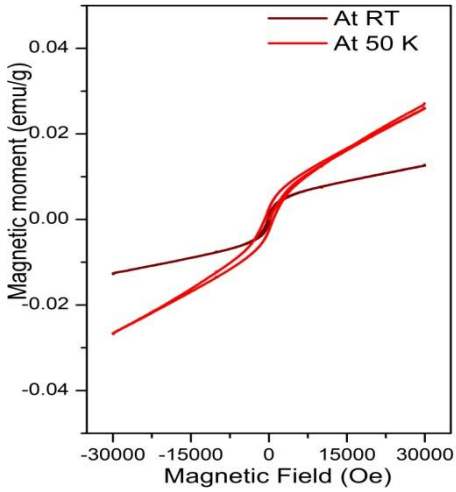

Fig. 5.21 Magnetic field versus magnetization study on pristine Al_2TeO_6 sample at RT and 50 K.

Fig. 5.21 presents magnetism by Al_2TeO_6 compound at 50 K and room temperature. Interestingly, this particular compound show hysteretic behavior to a larger extent at 50 K than at room temperature, with no saturation magnetization up to 3 T. This behavior could be possibly due to the exchange of unpaired electron spins from the oxygen vacancies at the compound surface [195].

5.3 Thermoelectric power (TEP)

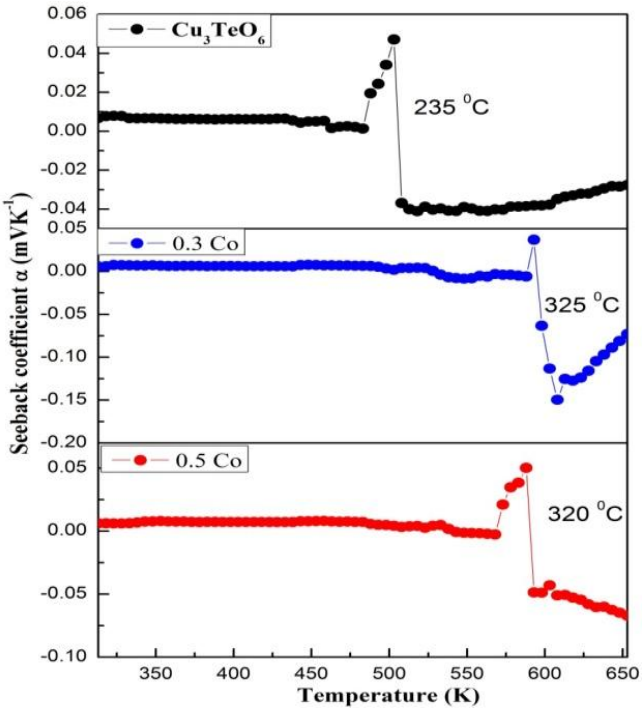

Fig.5.22. Variation of Seebeck coefficient with temperature for $Cu_{3-x}Co_xTeO_6$ (x=0, 0.3 and 0.5) samples showing insulator to n-type transition at a critical temperature.

Thermoelectric power measurements were carried out in order to measure the conduction phenomena on the prepared samples, which displayed semiconductor behavior at a higher temperature. Fig. 5.22 represents the plot of Seebeck coefficient versus temperature from 40 - 400 °C for $Cu_{3-x}Co_xTeO_6$ (x = 0, 0.3 and 0.5) compounds in a two probe TEP measurement set up. A sudden change in "α" is observed at 235 °C for pristine which immediately drops down to the negative region signifying a conduction mechanism/phase change. Similar observations could be drawn from the doped compounds around 300 - 320 °C temperature showing p-type to n-type transition. The dropped down values closely resemble the values obtained by DC resistivity measurements.

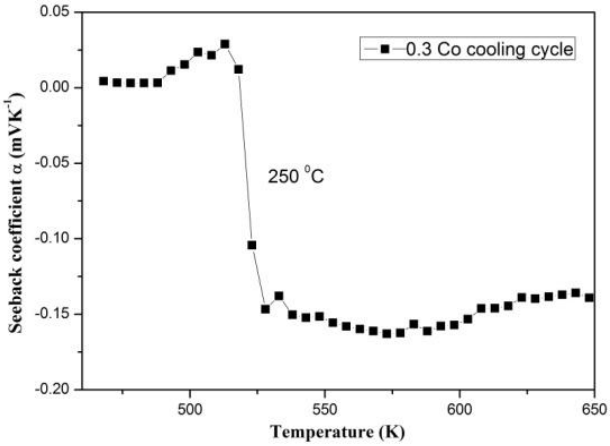

Fig. 5.23. Variation of Seebeck coefficient with temperature for $Cu_{3-x}Co_xTeO_6$ (0.3) sample for the cooling process.

TEP analysis of $Cu_{2.7}Co_{0.3}TeO_6$ for cooling cycle also shows a similar behavior with a change in the property at a lower temperature than that obtained for heating cycle (Fig. 5.23). All the samples show a very negligible value of Seebeck coefficient which restates their insulating property in the lower temperature region, already deduced through resistivity studies.

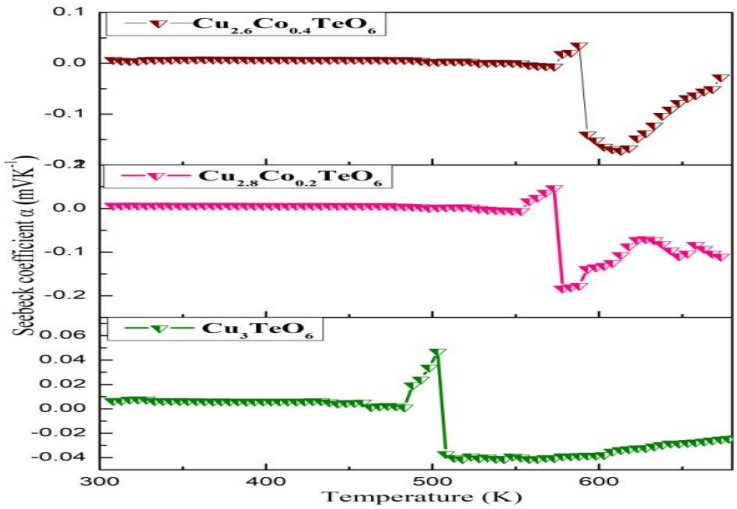

Fig. 5.24 Variation of Seebeck coefficient with temperature for $Cu_{3-x}Co_xTeO_6$ (x=0, 0.2 and 0.4) samples showing insulator to n-type transition at a critical temperature.

Thermoelectric power measurements were studied for other concentrations of cobalt doped copper tellurate which present similar results Fig. 5.24. The insulator type behavior is seen clearly in the lower temperature region as observed from the resistivity plots. It gives a very negligible value of the Seebeck coefficient. An abrupt change in mechanism is observed from positive to a negative value for "α" indicating their high-temperature semiconductor behavior.

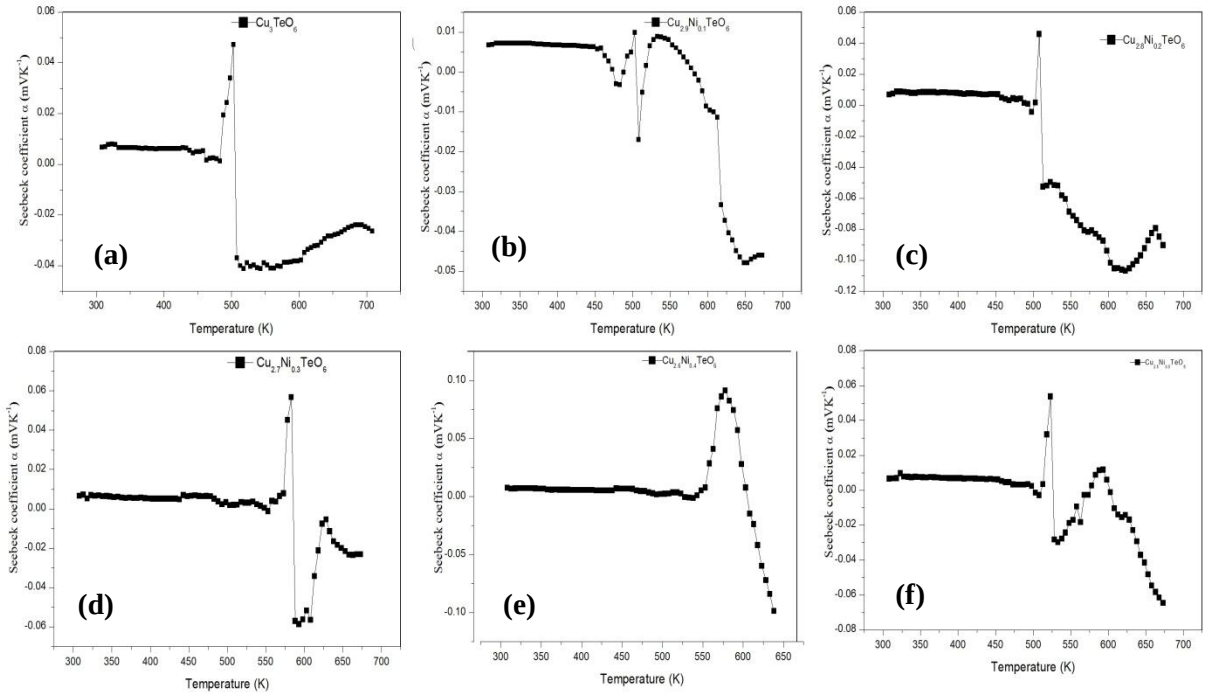

Fig. 5.25 Variation of Seebeck coefficient with temperature for $Cu_{3-x}Ni_xTeO_6$ (x=0 - 0.5) samples showing insulator to n-type transition at a critical temperature.

Fig. 5.25 represents thermoelectric power studies on nickel doped copper tellurates which display similar plot like that of cobalt doped series. Initial negligible value of Seebeck coefficient which remains constant till T_N could be assigned to the insulating property of compounds at low temperatures. A sudden drop in these TEP plots could be correlated to the semiconducting nature of compounds as observed from their resistivity plots.

5.4 Dielectric studies

Frequency dependent dielectric constant and dielectric loss:

A variety of compounds including tellurates possess great insulating properties which empower their electrical properties, useful in various multifunctional devices. Frequency dependent dielectric permittivity plot for pristine copper tellurate and cobalt doped copper tellurate is presented in Fig. 5.26.

The dielectric constant for all samples is found to decrease with increasing frequency. It is observed due to a reduction in an effective number of dipoles. Dipoles may follow the direction of ac electrical field at a lower frequency but, with increasing frequency, dipoles start to lag behind the frequency of the electric field, leading to a decrease in the dielectric value. At a characteristic value of frequency, the dielectric constant shows relaxation. This is due to the fact that, at very high frequency, the dipoles are not able to align with the field [196,197]. The polarization decreases with increase in frequency and reaches a constant value as, beyond a certain frequency of external field, the electron exchange cannot follow the alternating field. The dielectric loss also decreases with increase in frequency as expected. Dielectric loss is high around the relaxation or resonance frequencies, since polarization lags behind the applied field, causing an interaction between the field and the dielectric's polarization, thus causing heating.

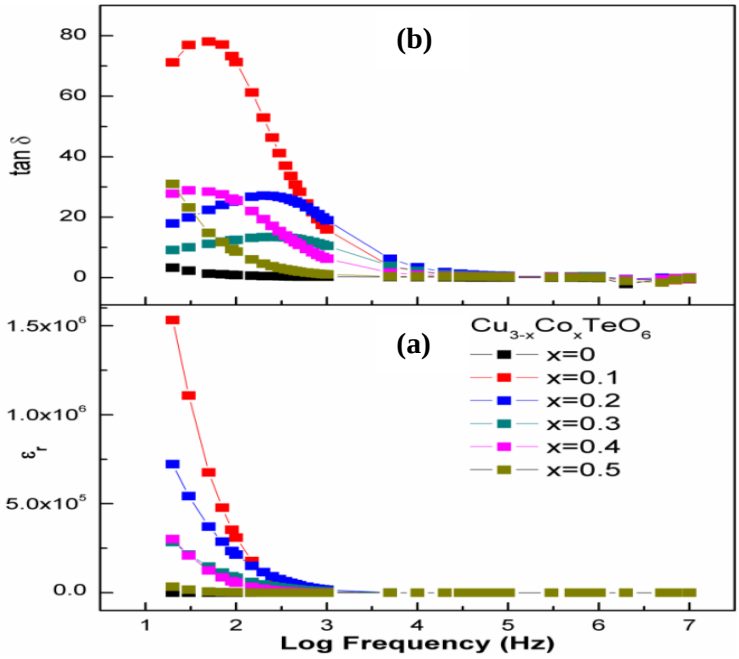

Fig. 5.26. Frequency-dependent relative permittivity and dielectric loss for Co-doped Cu_3TeO_6 (a, b) at room temperature.

The doped compositions are found to show the higher value of dielectric constant and accordingly, dielectric loss compared to Cu_3TeO_6 Fig. 5.26. However, dielectric constant as well as dielectric loss of $Cu_{3-x}Co_xTeO_6$ (x = 0, 0.1, 0.3 and 0.5) is observed to decrease with increase in Co concentration. On doping a significant quantity of cobalt, dielectric constant attains value to an extent of, $\varepsilon_r \sim 10^6$ Fig. 5.26 (a). Such a high value of permittivity is observed at lower frequencies (up to 1 kHz), beyond which, there is relaxation in permittivity in all samples. Among all the samples, $Cu_{2.9}Co_{0.1}TeO_6$ exhibits the highest value of dielectric constant under frequency domain.

Frequency dependent dielectric loss of all the compositions is shown in Fig. 5.26 (b). From the plot, it is observed that the relaxation frequency shifts to higher frequencies on increasing the dopant concentration up to $Cu_{2.7}Co_{0.3}TeO_6$. For higher concentration that is $Cu_{2.5}Co_{0.5}TeO_6$, relaxation frequency moves towards the lower side of frequency. It is reported in the literature that, at low frequency the loss

increases which could be due to the dominant conduction process.[36] However, the dielectric loss decreases with increase in dopant concentration. The incorporation of cobalt in low amounts must be favorable for polarization, as $Cu_{2.9}Co_{0.1}TeO_6$ shows the highest value for dielectric constant. To understand this trend in detail, one can perform charge density analysis, in order to get an idea of how the electronic polarization in the Co-doped Cu_3TeO_6 system changes on application of electric field [198].

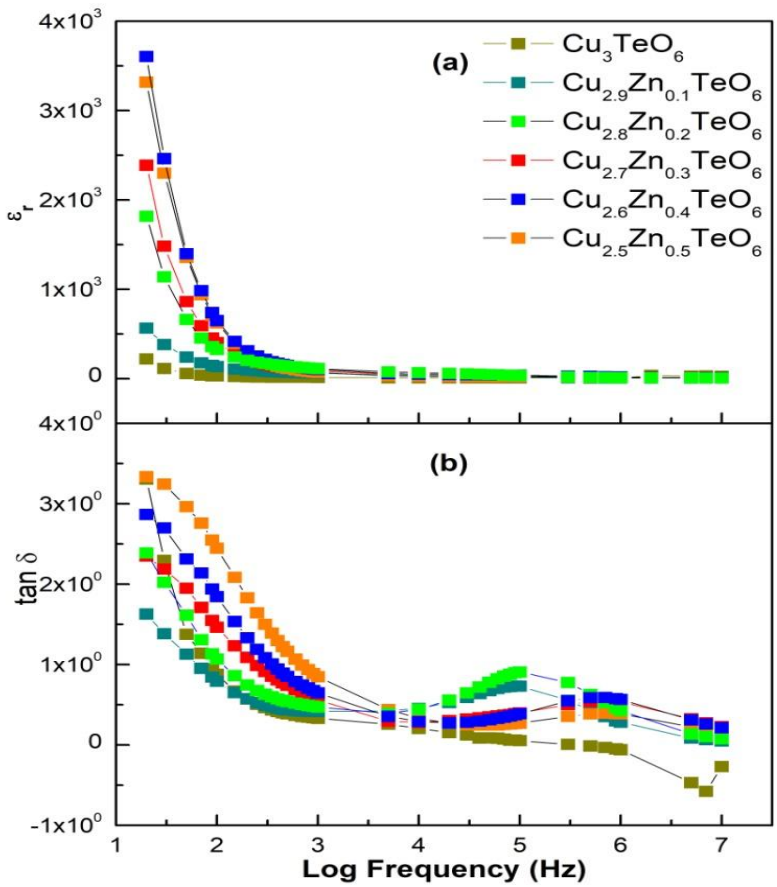

Fig. 5.27 Frequency dependent relative permittivity and dielectric loss for Zn doped Cu_3TeO_6 (a, b) at room temperature.

A series of zinc doped copper tellurates were accounted for their dielectric property with respect to the frequency as shown in Fig. 5.27. Dielectric constant, as well as dielectric

loss, is found to decrease with increase in the dopant concentration. Also, both dielectric constant and dielectric loss is found to decrease with increase in frequency, as, beyond a certain frequency of external field, the electron exchange cannot follow the alternating field. The dielectric loss also decreases with increase in frequency as expected. Dielectric loss is high around the relaxation or resonance frequencies, since polarization lags behind the applied field, causing an interaction between the field and the dielectric's polarization, thus causing heating.

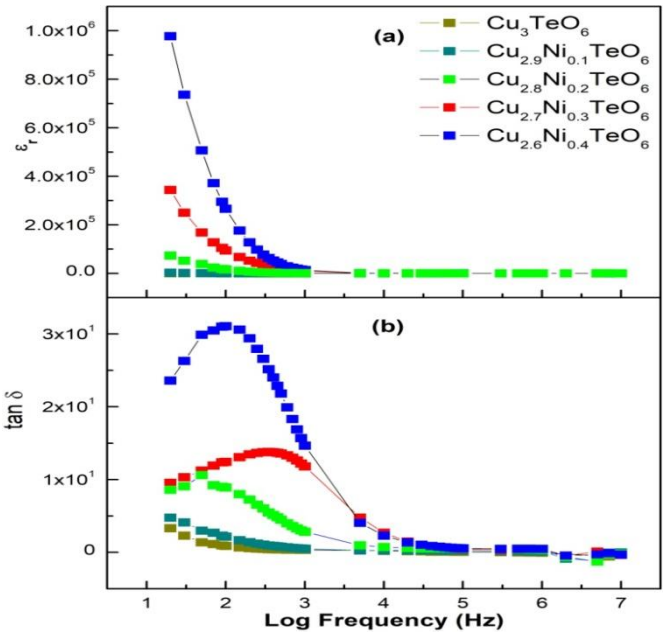

Fig. 5.28. Frequency-dependent relative permittivity and dielectric loss for Ni-doped Cu_3TeO_6 (a, b) at room temperature.

Similar trends of dielectric constant and dielectric loss with a log of frequency were observed for nickel doped copper tellurates (Fig. 5.28). This series of compounds were found to show a rise in their dielectric properties on doping with nickel. Dielectric constant and dielectric loss are high at a lower frequency as at lower energies, the dipoles lie separated, thus producing high permittivity, further loses it, as polarization occurs at the higher side of frequency.

Fig. 5.29 and 5.30 present similar pattern for dielectric permittivity and dielectric loss, that is, it decreases with increase in frequency. It is observed as the effective number of dipoles is reduced. With increasing frequency, dipoles hinder behind the frequency of the electric field, leading to a decrease in the dielectric value. Dielectric loss is high around the relaxation or resonance frequencies, since polarization lags behind the applied field, causing heating due to the interaction between the field and the polarization. In Fig. 5.30, we observe that the properties are raised considerably on replacing the Te ion by W in small concentration.

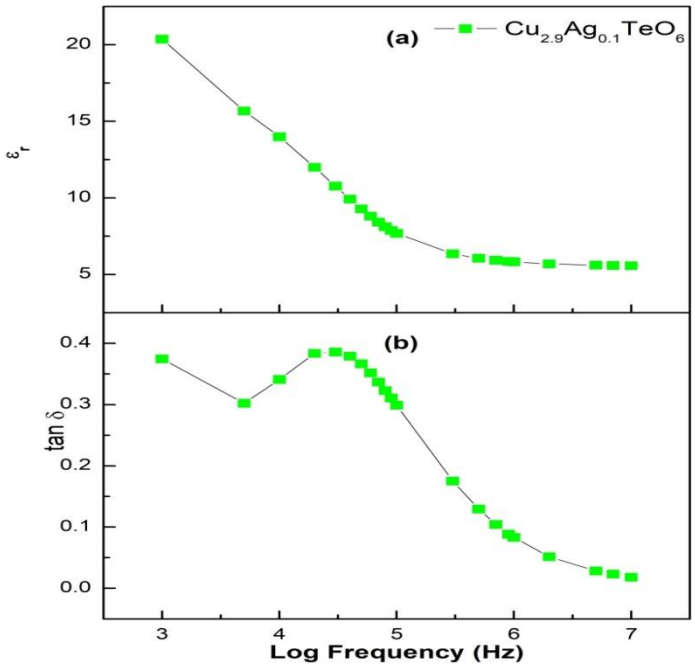

Fig. 5.29. Frequency-dependent relative permittivity and dielectric loss for Ag-doped Cu_3TeO_6 (a, b) at room temperature.

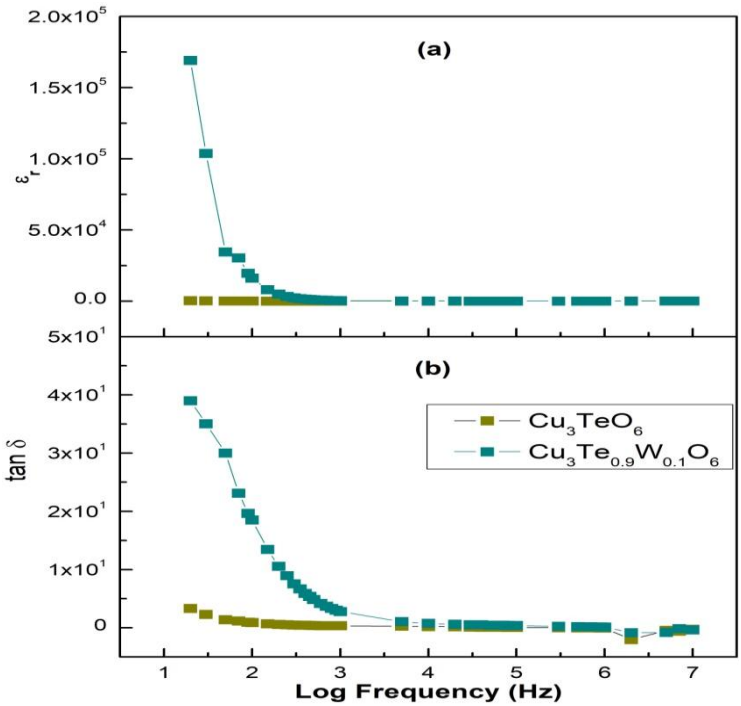

Fig. 5.30 Frequency dependent relative permittivity and dielectric loss for W doped Cu_3TeO_6 (a, b) at room temperature.

A comparative dielectric study has been performed between two tellurates with a metal ion in 3+ oxidation state. Iron on being replaced by Aluminium in the tellurate system show a slight variation in the dielectric values. The dielectric constant or relative permittivity (ε_r) and dielectric loss (tan δ) as a function of frequency at room temperature for the pristine iron tellurate is presented in Fig. 5.31. There is a decreasing trend observed in the dielectric constant and dielectric loss with an increase in frequency at room temperature. This is because; the induced electric dipoles are unable to respond to the change in the AC electric field. From both the figures, we observe that the aluminium tellurate (Fig. 5.32) show significantly higher dielectric values compared to the iron tellurate.

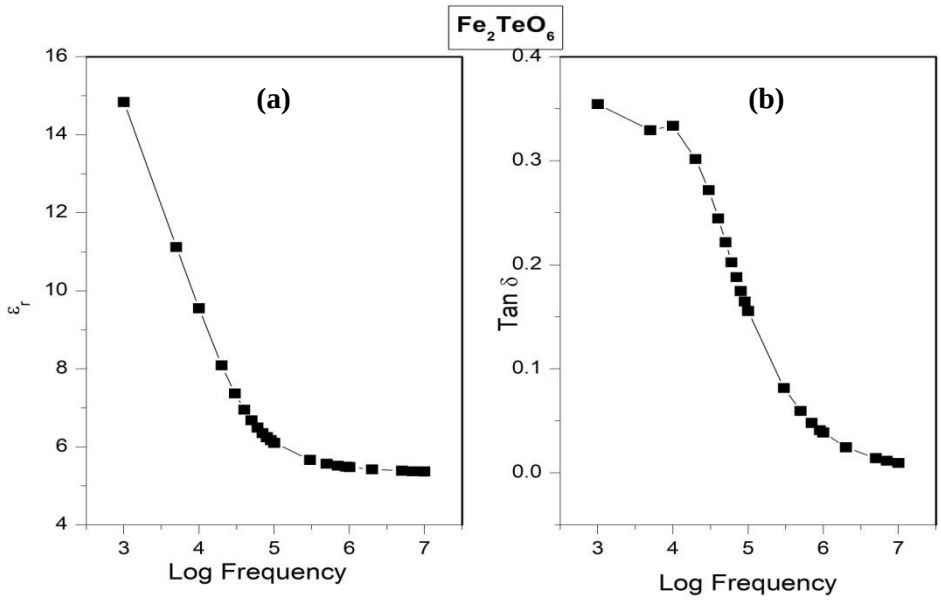

Fig. 5.31. Frequency-dependent relative permittivity and dielectric loss for Fe_2TeO_6 (a, b) at room temperature.

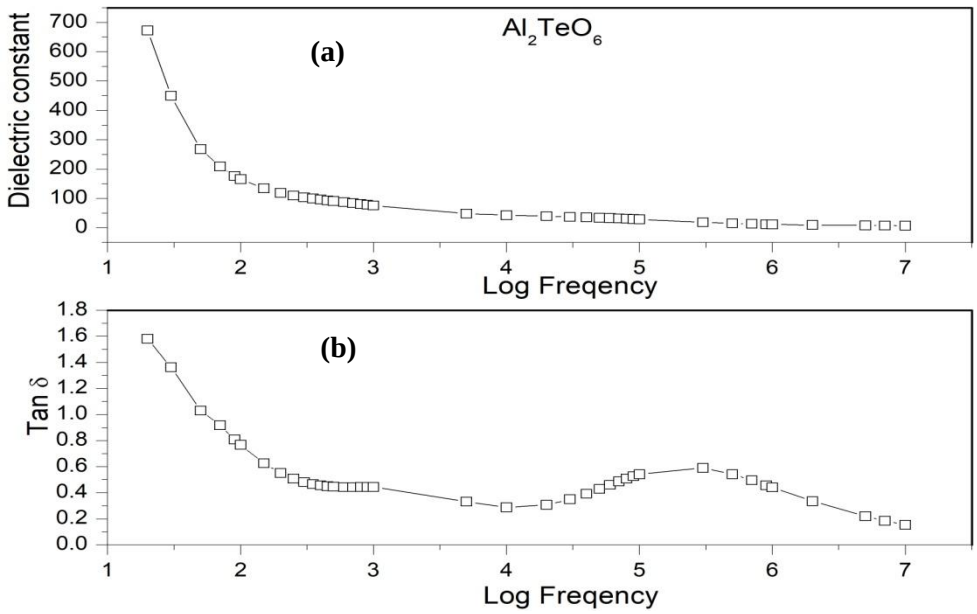

Fig. 5.32 Frequency dependent relative permittivity and dielectric loss for Al_2TeO_6 (a, b) at room temperature.

Temperature-dependent dielectric constant and dielectric loss:

Fig. 5.33 illustrates the relative dielectric constant (ε_r) and dielectric loss (tan δ) as a function of temperature over a range of selected frequencies for the

$Cu_{2.9}Co_{0.1}TeO_6$ compound. The dielectric constant of $Cu_{2.9}Co_{0.1}TeO_6$ material is found to be stable up to a certain temperature of ~ 650 K and then starts increasing with the further rise in temperature. The maximum value of the dielectric constant observed at high temperature is found to decrease with increasing frequency, presenting strong frequency dependence at high temperature (Fig. 5.33a).

Rise in permittivity at higher temperature is expected as polarization increases due to increase in charge carrier with temperature [199]. In general the high dielectric constant at low frequencies and high temperature is due to the existence of permanent dipole moments which construct a small effective charge separation, possibly due to the asymmetric fields experienced by either oxygen or metallic ions. In most cases, the atoms or molecules cannot orient themselves in low-temperature region since thermal energy is not sufficient. When the temperature rises, the orientation of these dipoles is facilitated which leads to an increase in the dielectric polarization [200]. At higher frequencies, the dipoles are not free to orient and hence the orientation polarization becomes less. Thus the total increase in polarization tends to grow less, with the rise in temperature at higher frequencies.

Increase in dielectric constant is accompanied by a dielectric loss peak which is observed to shift with the rise in temperature towards the higher side (Fig. 5.33b). Dielectric loss shows a similar rise with increasing temperature at all the selected frequencies and is found to display the highest value for the lowest frequency. This means that, with the rise in frequency, dielectric loss decreases. With the increase in temperature, dielectric loss increases since polarization take place, concurrently, the flow of charge through the material cause energy dissipation. The high dielectric loss at low frequencies and high-temperature results, as polarization becomes lofty at low

frequencies as compared to that at high frequencies. Other doped samples present a similar behavior with temperature and frequency.

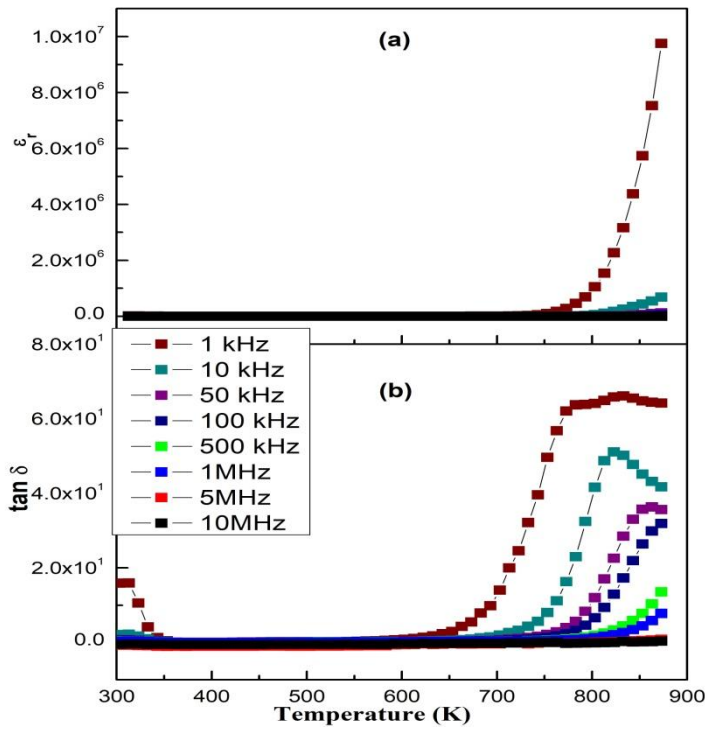

Fig. 5.33. Temperature-dependent relative permittivity and dielectric loss for Co-doped Cu_3TeO_6 (a, b) at variable frequencies.

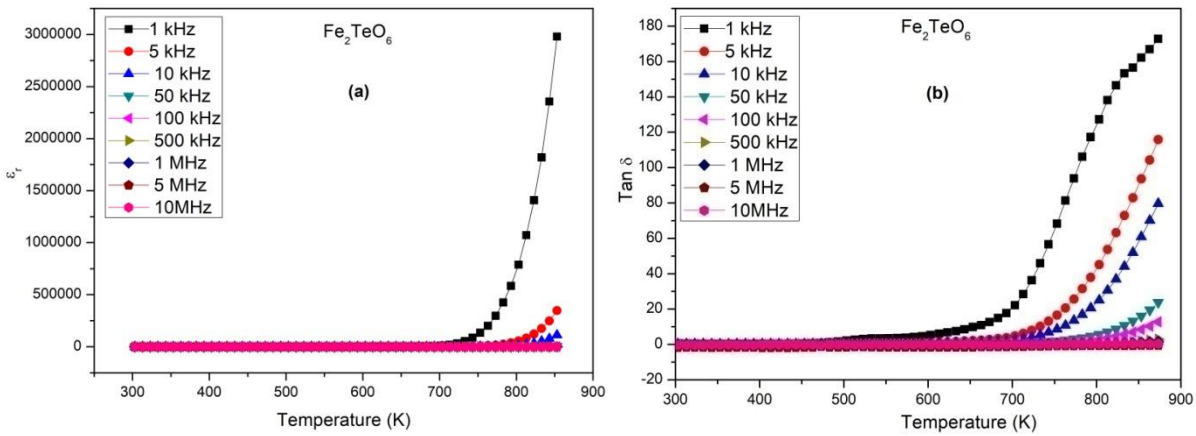

Fig. 5.34 Temperature dependent relative permittivity and dielectric loss for pristine Fe_2TeO_6 (a, b) at variable frequencies.

An increase in έ and tan δ is observed with an increase in temperature because the orientation of dipoles is facilitated at a higher temperature. Rise in permittivity at higher temperature is expected as polarization increases due to increase in charge carrier with temperature [199]. Usually, the high dielectric constant at low frequencies and high temperature is as a result of permanent dipole moments which create a small effective charge separation, possibly due to the asymmetric fields experienced by either oxygen or metallic ions. When the temperature rises, the orientation of these dipoles is facilitated which leads to an increase in the dielectric polarization [200]. But at higher frequencies, the dipoles are not free to orient causing the orientation polarization to become less. Thus the total increase in polarization tends to grow less, with the rise in temperature at higher frequencies.

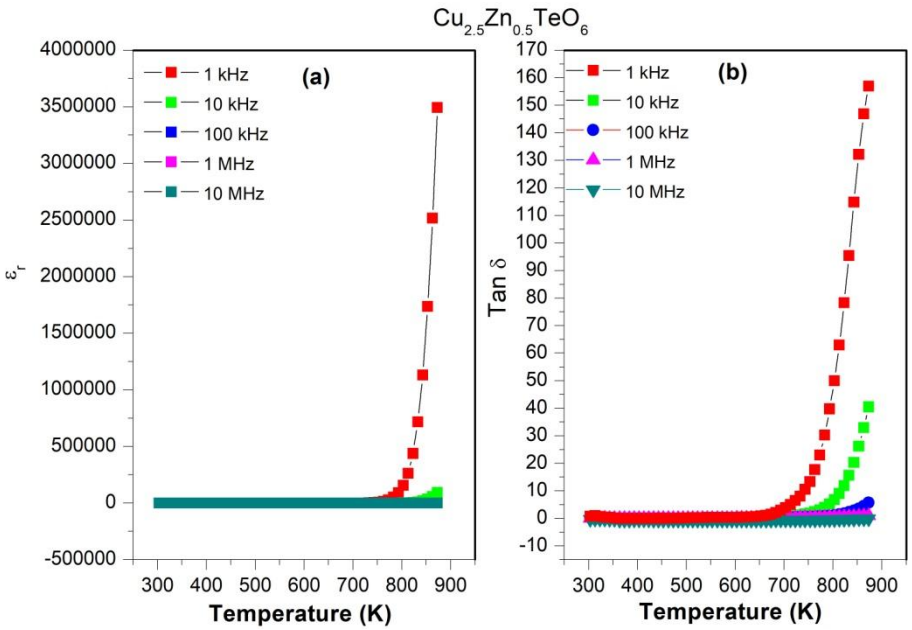

Fig. 5.35 Temperature dependent relative permittivity and dielectric loss for Zn doped Cu_3TeO_6 (a, b) at variable frequencies.

The highest concentration of zinc doped copper tellurate presents similar patterns for dielectric v/s temperature studies as above. An increase in έ and tan δ is observed with an increase in temperature because the orientation of dipoles is facilitated at a higher temperature. A drop in έ and tan δ is observed with increasing frequency as the dipoles are unable to reciprocate to the change in AC electric field (Fig. 5.35).

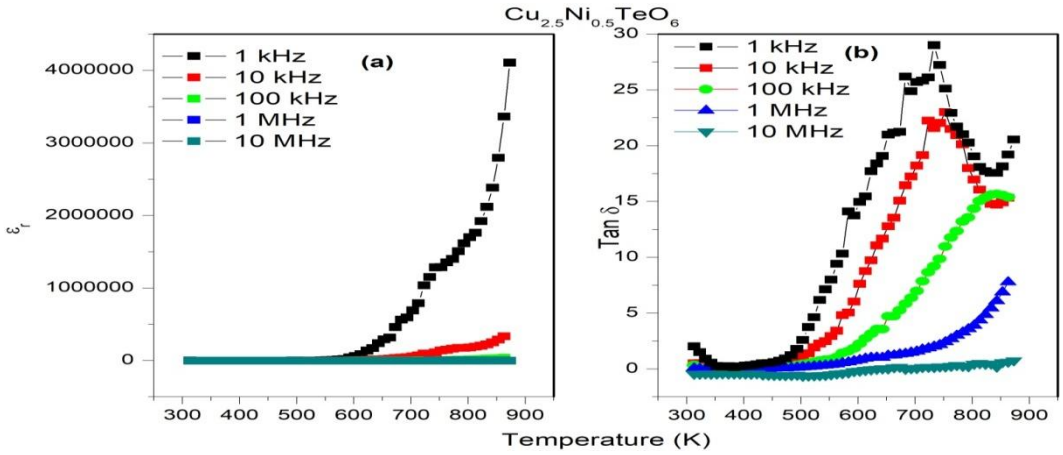

Fig. 5.36 Temperature dependent relative permittivity and dielectric loss for Ni-doped Cu_3TeO_6 (a, b) at variable frequencies.

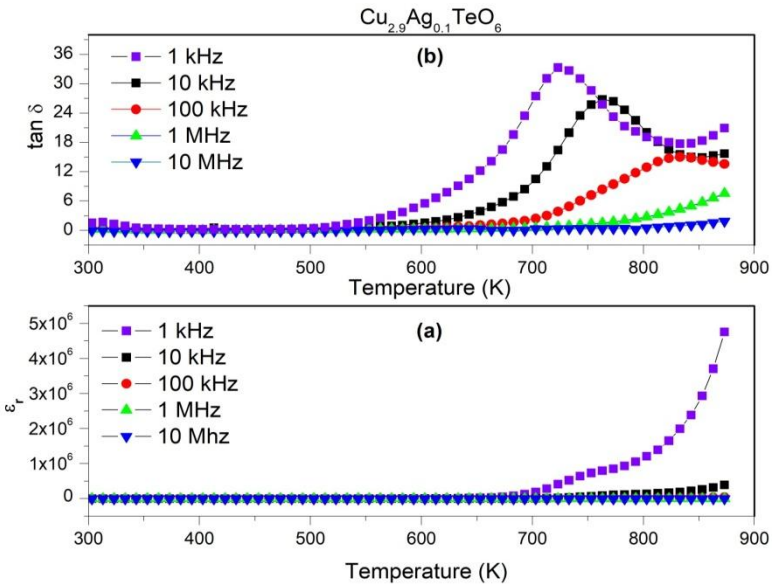

Fig. 5.37 Temperature dependent relative permittivity and dielectric loss for Ag-doped Cu_3TeO_6 (a, b) at variable frequencies.

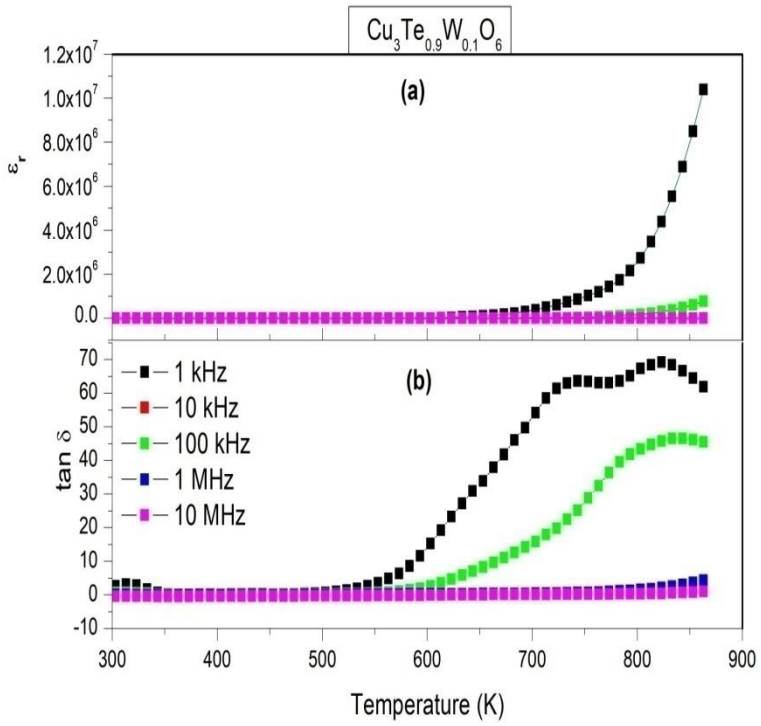

Fig. 5.38 Temperature dependent relative permittivity and dielectric loss for W doped Cu_3TeO_6 (a, b) at variable frequencies.

Temperature-dependent dielectric permittivity and dielectric loss at variable frequencies for Fig. 5.36, 5.37 and 5.38 present similar results. Increase in dielectric permittivity and dielectric loss with temperature is observed due to the fact that thermal energy leads to orientation of dipoles at high temperature. Also, ε` and tan δ show decrease in their values with increasing frequencies as the dipoles are unable to respond to the change in AC electric field.

5.5 Photoluminescence Studies

Tellurium-containing compounds are well known to show good optical properties, hence tellurates were studied for photoluminescence property in the present work. PL occurs when the material is excited by photon (often ultra-violet), leading to emission that is a release of energy in the form of photon [201].

A very few tellurate compositions were accounted for their photoluminescence property. Fig 5.39 shows PL of a pristine Cu_3TeO_6 along with Co-doped copper tellurate compound at room temperature. Excitation in UV region of 260 nm produces an emission in the visible region at ~ 485 nm with blue-cyan color radiation. The PL spectrum of undoped copper tellurate is dominated by a strong/intense band. The luminescence intensity was observed to drop down drastically on cobalt doping, probably due to the decrease in their grain sizes on doping, as seen from the TEM images. Doped ones show reduced particle sizes than the un-doped. Consequently, replacing Cu with Co cause significant tuning of the PL strength hence, finding its application in fields of optoelectronics.

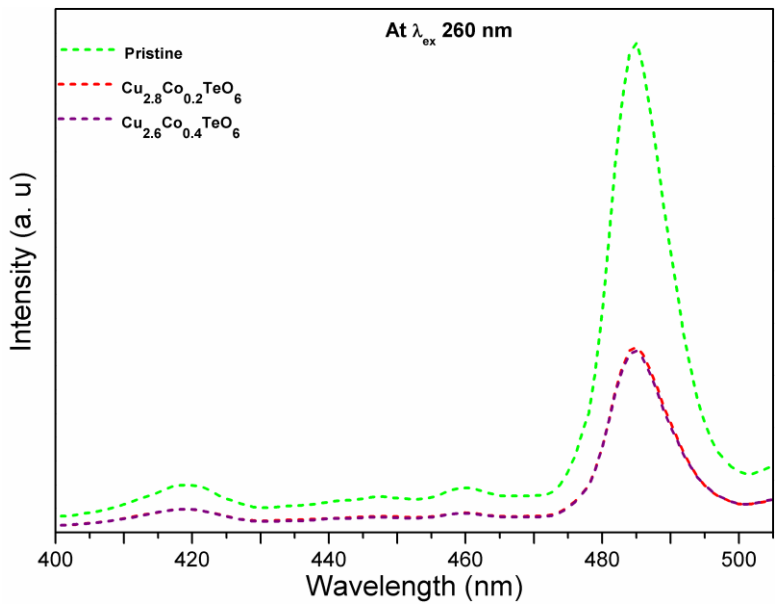

Fig. 5.39 Photoluminescence spectrum of Co-doped copper tellurate.

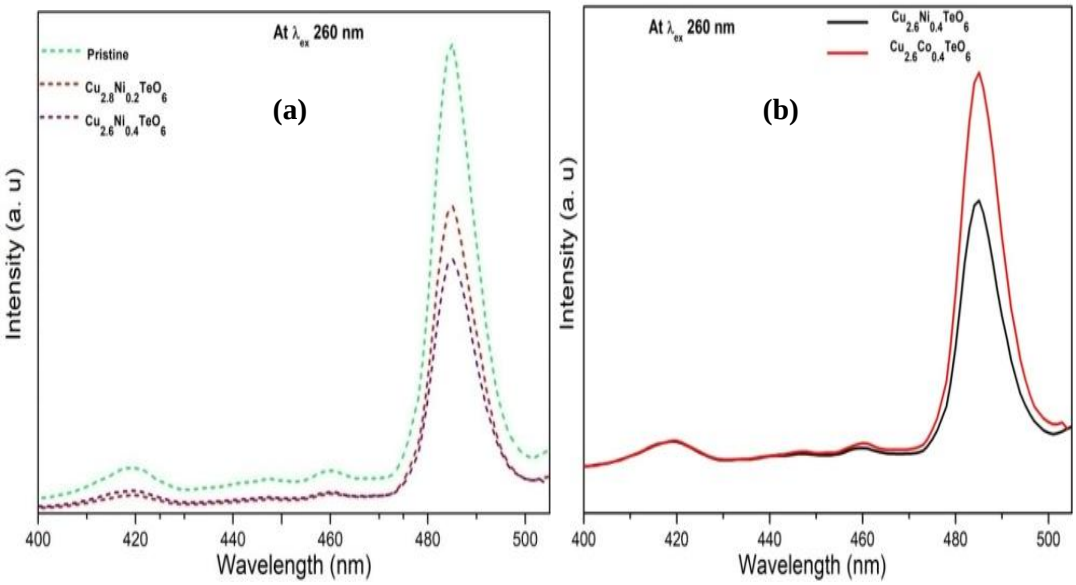

Fig.5.40 Photoluminescence spectra for Cu_3TeO_6 and Ni-doped Cu_3TeO_6.

As seen in Fig. 5.40. with an increase in dopant concentration, there is a decrease in the PL intensity, suggesting that the degree of recombination of electron-hole pair shrink as the dopant develop an impurity level close to valence band thereby preventing diffusion of electron and hole causing lowering of PL intensity, thus leading to reduced band gap energy [202,203]. Amongst the doped compositions, cobalt doped copper tellurate possesses PL to a lower extent than the nickel composition as expected, since the band gap value for cobalt doped compound is lower than that for nickel doped compound.

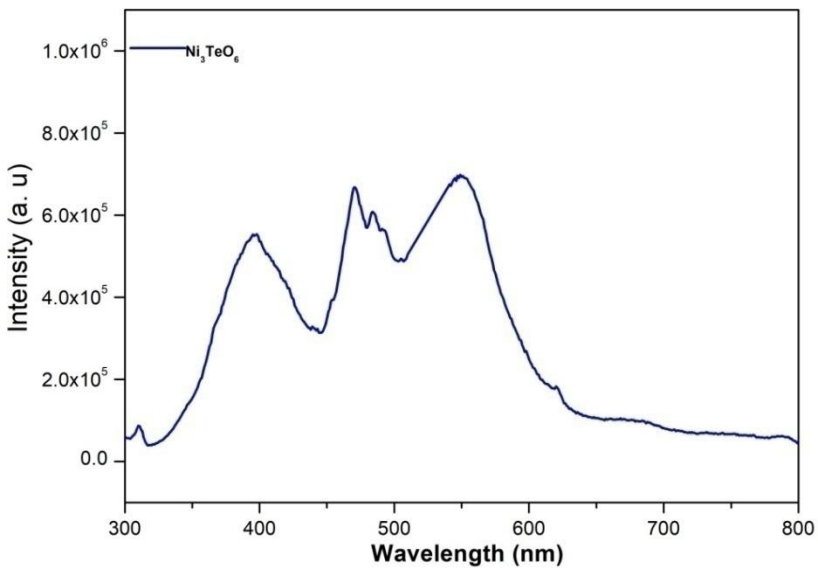

Fig.5.41 Photoluminescence spectra for Ni_3TeO_6.

Fig. 5.41 shows PL spectrum for pristine Ni_3TeO_6 sample and is found to be PL active with emission in the blue-green region at an excitation wavelength of 260 nm. The emission observed here is consisting of broad blue-green radiation with a tint of yellow emission.

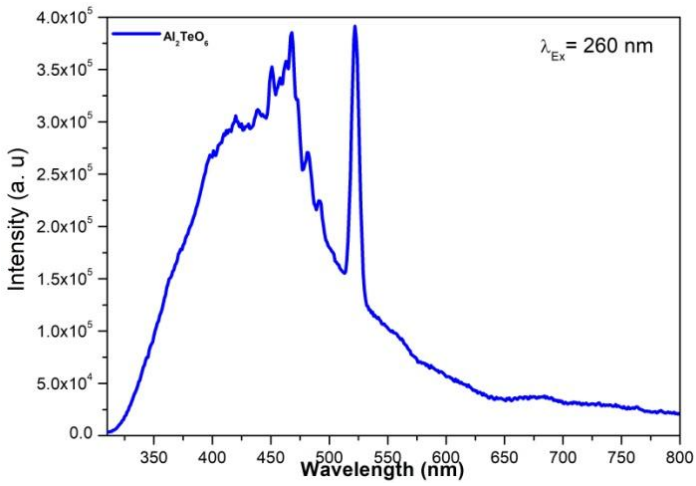

Fig.5.42 Photoluminescence spectra for Al_2TeO_6.

A very intense and broad emission is observed for pristine Al_2TeO_6 as shown in Fig. 5.42. The emission spectra consisted of major of the blue component at around 480 nm with

the highest PL intensity accompanied by green emissions. The spectrum was obtained at an excitation of 260 nm which is in UV region [204].

5.6 Other Miscellaneous Properties

5.6.1 Photocatalytic degradation of an organic dye:

Methylene blue, an organic dye was degraded over some metal tellurate catalyst, out of which only nickel tellurate could show complete degradation of the dye after 3 hours in presence of sunlight.

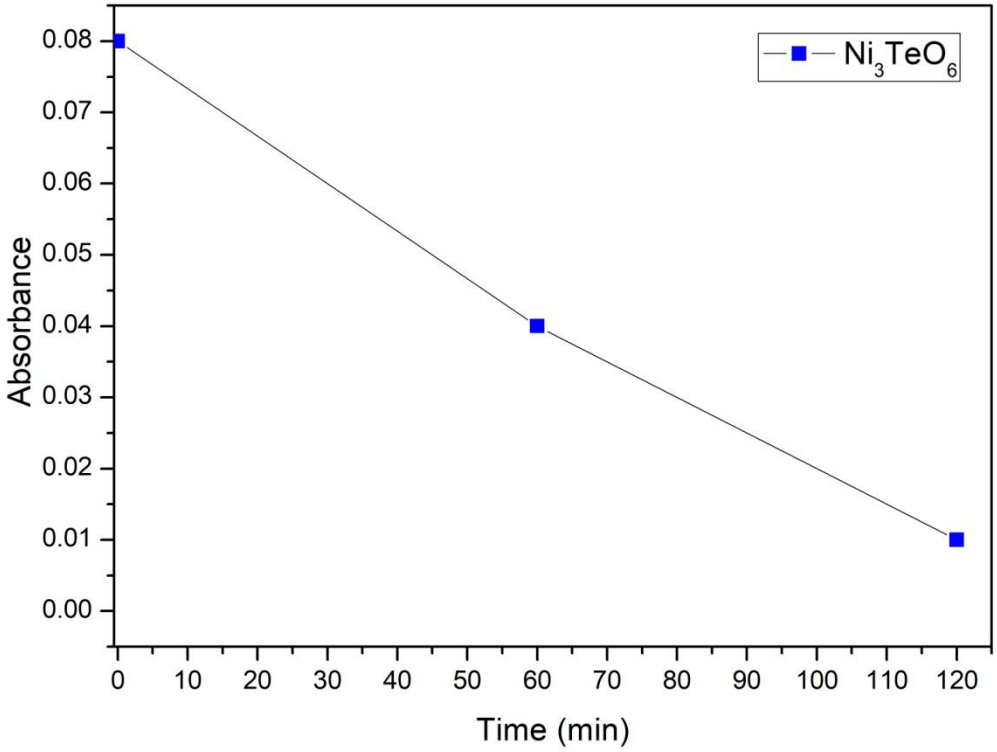

Fig.5.43 Photodegradation by Ni_3TeO_6.

It was only nickel tellurate which could degrade methylene blue completely among others. Around 500 mg sample of Ni_3TeO_6 was sufficient for the degradation of 100 ml of 15 ppm solution of MB dye.

5.6.2 Partial propylene oxidation:

Some prepared metal tellurates were tested as catalysts for partial oxidation of propylene to acrolein. The reaction was carried out in a fixed bed glass reactor as a function of the temperature of the catalyst. Among the selected metal tellurates, Mo and W doped Copper tellurates were found to show conversion to acrolein at higher temperature whereas others showed low activity. Since Te-containing compounds are found to show various catalytic conversions as mentioned in the literature, selected tellurates were investigated for partial oxidation study of propylene to acrolein. Fig. 5.44 below shows partial propylene oxidation over prepared catalysts. It is observed that amongst all four compounds, Mo-doped copper tellurate presents comparatively better results than the rest. Iron tellurate shows no activity at al up to 450 °C, although some reports are available on it [53]. Followed by this was copper tellurate with no significant output. Tungsten doped copper tellurate showed very moderate activity at lower temperatures whereas, Mo-doped copper tellurate show activity with the rise in temperature. The activity appeared not so advanced on these compounds.

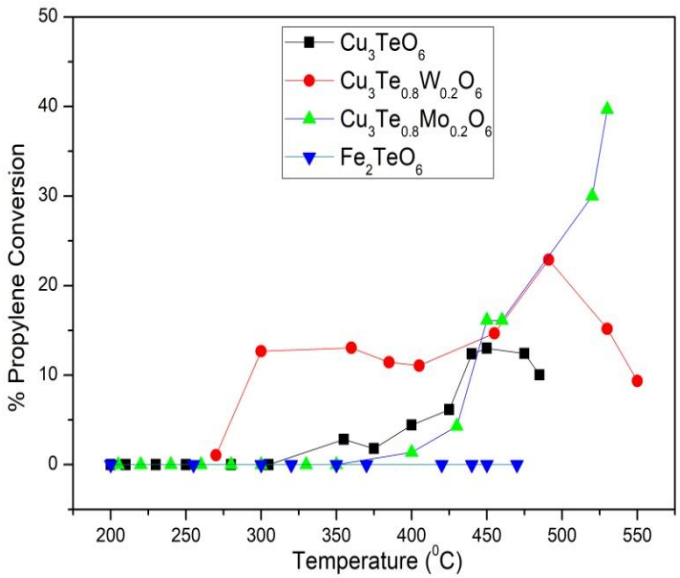

Fig.5.44 Partial propylene oxidation over prepared catalysts.

5.6.3 Antibacterial Activity:

Doped and pristine metal tellurates were tested against two different emerging opportunistic bacterial pathogens Viz. Gram-negative *Escherichia coli* and Gram-positive *Staphylococcus aureus* using agar well diffusion method [205].

A stock solution of (20 mg/ml) of all the four compounds was prepared in DMSO separately and used for the assay. The overnight grown pathogens were platted on nutrient agar. Sterile cork borer (6 mm) was used to bore wells and different concentrations of nanoparticle suspension were loaded on to the wells. The plates were incubated at 37 °C for 24 h and were checked for the zone of inhibition around the colony. It was observed that Ag-doped copper tellurate demonstrated excellent antimicrobial activity amongst all the tellurate compounds.

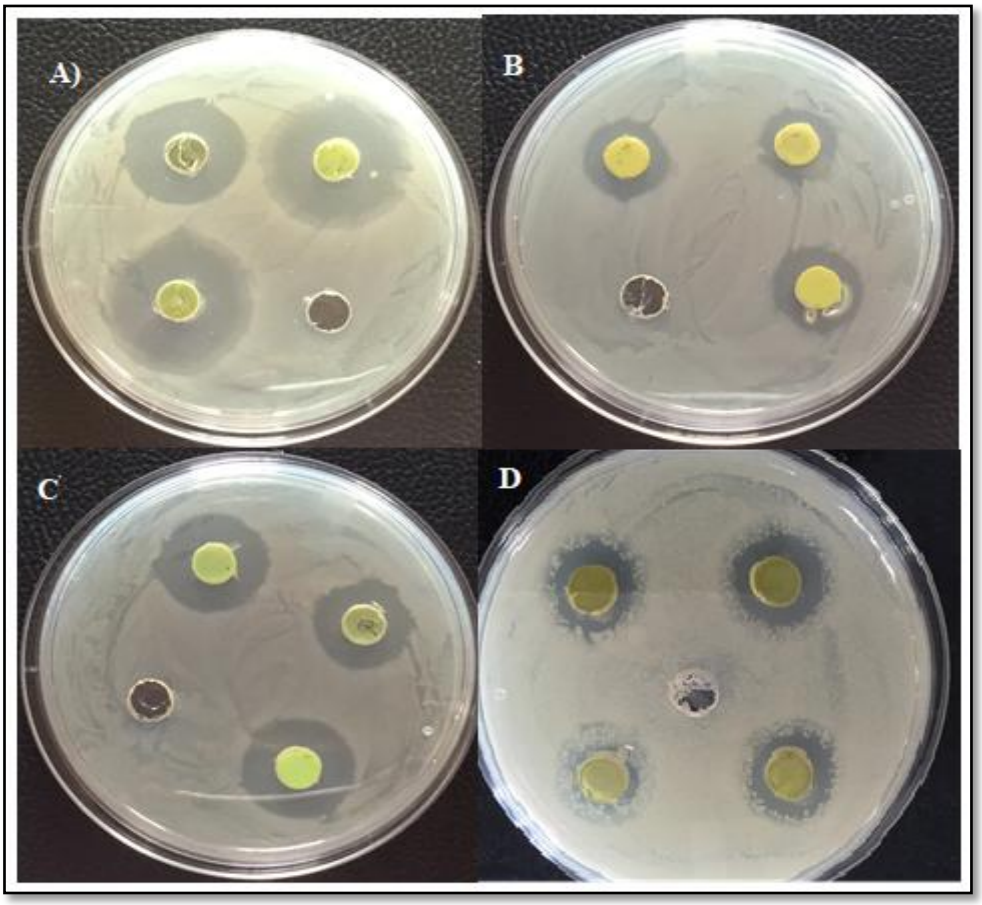

Fig. 5.45 Effect on growth of pathogens by: A) $Cu_{2.9}Ag_{0.1}TeO_6$, B) Cu_3TeO_6, C) Ni_3TeO_6 and D) $Cu_{2.9}Zn_{0.1}TeO_6$.

The effect of tellurate compounds on the growth of pathogens is depicted in Fig. 5.45 and 5.46. The area around the well showing no growth was measured as the zone of inhibition for the respective pathogen. It was observed that Ag-doped Cu tellurate demonstrated excellent antimicrobial activity followed Zn and Ni-doped Cu tellurate compounds. However, Cu tellurate without any dopant showed the least activity moreover, the activity was found to be dose dependent and metal specific. Thus, the synergistic effect of Ag, Ni and Zn doped Cu tellurate compounds is very well evident. Gram-negative *E.coli* was found to be considerably more sensitive towards all the tellurate compounds as compared to Gram-positive *S. aureus*. This is mainly due to the differences in the cell structure and compositions of Gram-positive and Gram-negative bacteria. The above findings are evidence of dose-dependent antimicrobial activity of tellurate compounds against broad spectrum, developing hospitalized pathogens.

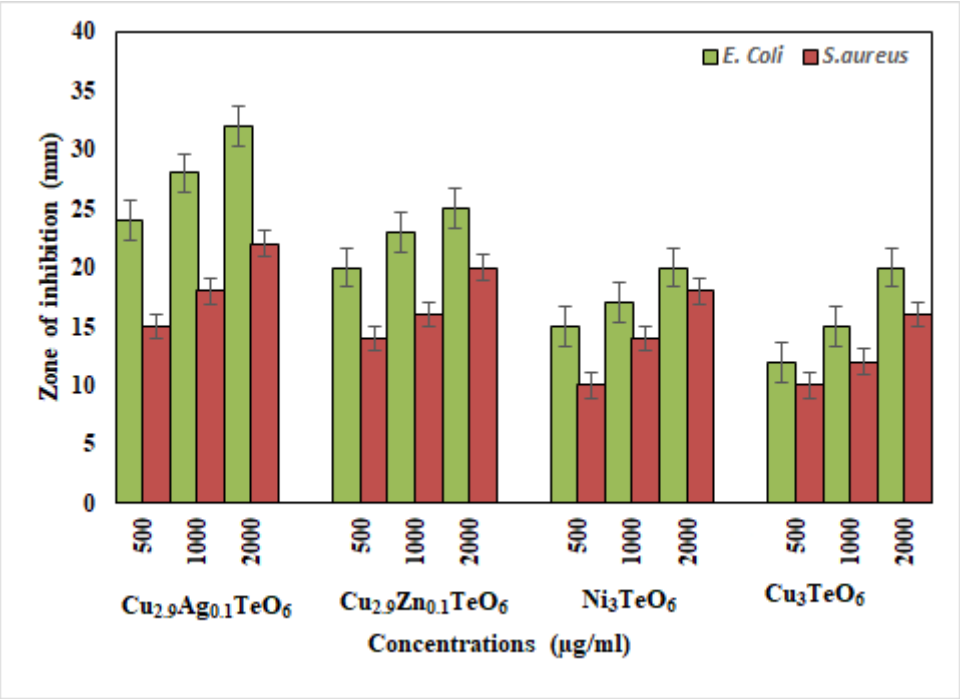

Fig. 5.46 Anti-microbial activity of tellurate compounds against clinically potent pathogenic isolates.

As the pathogens used for the study are known to be causative agents of various life-threatening infections viz. nosocomial infections, endocarditis, gastroenteritis, and urinary tract infections, in host compromised patients. Nanoparticle-based approach for antimicrobial activity is of much more noteworthy since many of these pathogens are developing resistance to many forefront antibiotics.

Chapter 6

Summary and Conclusions

6.1 Summary

The summary of the thesis has been divided into six chapters as mentioned earlier and each of the chapters can be summarised as follows:

Chapter 1

The introduction of the overall work on this thesis has been put forth in chapter 1, which introduces the first brick of the work with material science and its progressing advancements till date. The need for research in material science today is discussed due to the ever growing demands in technology field. Specifically, metal oxide semiconductors are considered the most common materials due to their low cost. The relevance of structural modification on material's property have been disclosed which reveal that the materials depend on structural features for variable properties. It is well known that the compounds containing Te exhibit exceptional properties in electrical, magnetic, thermal, optical and others which are therefore commonly employed in recent technologies and in different multifunctional systems. The significance of doping has been look in to, which is known to modulate the nature of the material in a systematic way. The importance of synthesis as a key role in governing the applications of materials has been discussed as synthesis of a material in a particular way, influences the size or shape of the constituent particles, thus changing its property. Hence reports on various methods of synthesis have been reported in literature which defines their variable properties. Prepared material's ability to show properties other than reported have been explored for the first time has been discussed. This chapter concludes representing the highlights of the thesis which are focused on the main points of the work and how the thesis has been organised to get a brief idea regarding this work.

Chapter 2

One should have knowledge on thorough history in particular area of research before proceeding with any innovative idea. For this purpose a well planned literature survey is conducted in order to get some idea about its past, present and futuristic goals. Here, chapter 2 deals with the literature survey on compounds containing tellurium and their various aspects like synthesis, applications, properties, reactivity etc. It is very well known fact that Te – compounds exhibit a variety of properties like electrical, magnetic, optical etc. which makes them useful for diverse technological applications like potential application in low temperature co-fired ceramics (LTCC) technology due to their low sintering temperatures. All the parameters of synthetic procedures, composition, their arrangement etc play a very important role in deciding the performance of any compound.

A variety of physical and chemical properties are investigated for the synthesis of transition and non transition elements specifically due to their distinct properties. Structure based properties are studied to understand the structural dependencies on the properties of oxides of tellurium. A detailed study on tellurium and its compounds right from its stable valencies to its various reactions, its oxy-anions and oxy-acids and its derivatives are presented in this chapter.

Scientists interest in multi-component tellurates has investigate that the compounds presented special structural features and resultant properties due to presence of tellurium ions. A variety of tellurium's use in general is displayed to get an idea of future applications. We get to know that majority of tellurium's use is as an additive in alloying, in chemicals, as catalyst chiefly for the oxidation of organic compounds and in other electrical uses such as in thermoelectric and photoelectric devices and optical devices.

Various methods of synthesis of Te containing material are displayed which are already reported in past, and which gives us an initiative to plan a synthetic methodology since synthesis step is considered very critical in deciding the overall behaviour of a material. Most of the reports are subjected to solid state synthesis, which on effect of temperature are known to get oxidised to tellurates. Literature on various tellurate compounds is put forth, starting with aluminium tellurate which are known for high frequency applications. Various properties and synthetic methods, which are mostly restricted to solid state synthesis methos are known for this particular compound. Followed by this is iron tellurate, which is known for various technological applications. Its synthesis and properties along with magnetic structures are highlighted in this chapter. Its synthesis is reported by solid state and PLD technique.

A very interesting collinear antiferrormagnet i.e. Ni_3TeO_6 is reported to exhibit various properties of magnetism, electric polarisation and very recently as a photocatalyst. This particular compound has been synthesized by flux growth, solid state, sol – gel, chemical transport methods. Its structural modifications and properties are introduced in this chapter. The most stable composition in the CuO-TeO_2 system that is, Cu_3TeO_6 is established to show interesting electrical properties and thus finds applications in the fields of electronics. Structural properties are known along with synthesis by various methods as mentioned for other tellurates. Its well known solid state properties like electrical, magnetic, optical and others are recognized in this chapter. In summary, this chapter provided us with the existing knowledge about the compounds containing tellurium and showed us the way to explore more about it.

Chapter 3

Chapter 3 dealt with the experimentation involved in producing metal tellurates. None of the reported methods of synthesis are used in producing any of the compounds, but a new method of synthesis is implemented, which is co – precipitation method which is well known to deliver compounds with advantages. This is experienced to be the efficient method of preparing a homogenous composition. Another method utilised is a well known sol – gel method.

Pristine and doped tellurates are prepared by co – precipitation method which produce, homogenised, monophasic compositions up to certain concentrations of metal ion. The resulting compounds obtained are highly stable in nature and easy in handling hence it serves as a very handy method of synthesis. Preparation of Al_2TeO_6 was slightly different from the rest of the tellurates and totally depended on the pH of the metal ion solution. Sol gel method is also utilised to obtain tellurates which involves more steps and high temperature, hence, co – precipitation method is preferred over sol – gel method. The precursors obtained before final sintering of compounds are studied for thermo gravimetric analysis to understand various processes leading to final formation of compounds. XRD and other instrumentation techniques have been described in this chapter which significantly helped in identification and characterisation of the compounds.

Chapter 4

Chapter 4 summarizes the characterization of all the prepared compounds and enables us to confirm its formation and purity. All the spectroscopic analysis along with the identification techniques and their observations cum results are discussed in this chapter.

The thermo gravimetric analysis (TG) with simultaneous differential thermal analysis (DTA) serves as very useful techniques in analysing behaviours of the precursors with temperature. It provides information about various thermally generated processes which

significantly help in understanding the compound formation. The precursors of all the compounds obtained via co-precipitation method show similar thermal processes. That is, initial weight loss up to 250 °C in TG is observed due to loss of water from the precursor, which is accompanied by an endothermic peak in DTA. With further rise in temperature, there appears a sharp exothermic peak around 550 °C (for copper tellurate and its doped compositions), due to the conversion from amorphous to crystalline phase which produces a small kink in the TG plot. This point of transformation of amorphous to crystalline phase differs slightly for other pristine tellurates indicating their temperature dependent phase formation nature. The precursor of nickel tellurate shows this point of conversion at around 700 °C, whereas, precursors of iron tellurate and aluminium tellurate shows at around 550 °C and around 650 °C respectively.

The precursors via sol-gel method show loss in weight up to 190 °C due to water loss from the hydrated gel accompanied with a light endotherm in DTA , signifying this loss of water. On further heating the gel up to ~ 350 °C, the organic components from the compound are decomposed presentation a sudden drop in weight in TG which is indicated by exothermic peaks in DTA curve. Beyond 350 °C, there is gain in weight observed in TG with corresponding sharp exothermic peak in DTA. This is expected due to the oxidation of Cu and Te to form the oxide.

The XRD of all prepared compounds revealed their identification thereby revealing the purity of compounds as all samples showed monophasic formation of compounds. Copper tellurate and its doped compositions showed to crystallize in cubic phase with no other impurity phase matching the reported JCPDS data. Crystallite size obtained using Scherrer's formula show reduction in crystallite size on doping in case of cobalt doped copper tellurate by co-precipitation method. This could probably be due to the distortion caused by radius difference between the dopant and the replaced ion. The ionic radii of Cu (II) is found to be

87 pm and that of Co (II) to be 79 pm, hence replacement of copper with cobalt may lead to shrinking or contraction of the crystal structure on doping. The peaks obtained from diffraction pattern of Ni_3TeO_6 and its doped compositions were indexed to rhombohedral structure corresponding to the reported JCPDS data. Whereas, the diffraction patterns of pristine and doped iron tellurates and aluminium tellurate showed tetragonal phase formation, with no extra peak for impurity and matched well with the reported JCPDS data.

The infrared spectra for the hydroxide precursor, gel precursor and the final oxide provided information about their structural environment. The hydroxide precursor shows presence of water molecules and the gel precursor shows presence of organic moieties. All these features of precursors are found to disappear for final oxides which show appearance of peaks in the region from 400 - 800 cm^{-1} corresponding to metal-oxygen revealing their purity at the same time.

The band gap values for prepared compounds are calculated from Taucs plot which are generated from the absorbance plot in the UV DRS studies. The obtained band gap values are found to lie in the semiconductor region. In some cases, the absorption spectra shows an extra band in the visible region, which could be accounted for the possible d-d transition occurring in coloured compounds.

The SEM analyses accompanied with EDS and the TEM analysis on tellurate compounds revealed the morphology of particles. Copper tellurate and its doped compositions show appearance of cube shaped particles in SEM and TEM with developed grain boundaries and particles appear to lie adhered to each other. In case of cobalt doped copper tellurates, the particles are observed to be smaller in size than the pristine copper tellurate, presenting the effect of dopant on the morphological features. Nickel tellurate present a different view of particle morphology with somewhat spherically shaped particles.

Aluminium tellurate showed spiky appearance of particles. EDS analysis confirmed the presence of expected elements in prepared compounds.

The XPS study helped in identifying the oxidation states of the metal ions present in the compound. All the compounds possessed metal ions in their expected valencies.

Chapter 5

This chapter dealt with the study of various properties exhibited by metal tellurates, like, electrical resistivity, dielectric properties, magnetic properties, PL properties, thermoelectric studies etc.

The plot for electrical resistivity is represented to show two types of conduction mechanisms for doped as well as pristine copper tellurate and nickel tellurate. At low temperature, it presents insulator type behaviour since there is no change in resistivity up to certain temperature. After attaining certain temperature, the resistivity appears to decrease with increase in temperature, resembling semiconductor phenomena. Iron tellurate presented semiconductor behaviour wherein, resistivity was found to decrease with increase in temperature.

Magnetic studies carried out on several tellurates presented properties of magnetism in these compounds. The magnetisation v/s magnetic field studies were carried out both at room temperature and 50 K which presented a diagonal nature of plot suggesting their ground state likely to be anti-ferromagnetic at low temperature. It was also observed here that, the magnetization increased on doping, with no saturation magnetization up to 30000 Oe. Magnetization v/s temperature plot for several tellurates was obtained at 250 Oe magnetic field with varying temperature from 50 to 120 K and was encountered to show antiferromagnetic spins below T_N.

TEP studies were carried out on some tellurates in order to measure the conduction phenomena exhibited by them which displayed a sudden change Seebeck coefficient with temperature signifying their conduction mechanism / phase change.

Dielectric studies with respect to frequency and temperature was studied which depicted insulating properties of tellurates. Frequencies and temperature have tremendous impact on the dielectric constant and dielectric loss of compounds. With increase in frequency, the dielectric constant is found to decrease for all the studied samples since, at very high frequency, the dipoles are not able to align with the field which means that the polarization decreases with increase in frequency and reaches a constant value as, beyond a certain frequency of external field, the electron exchange cannot follow the alternating field. The same trend is followed by dielectric loss. Amongst the doped compositions and pristine, doped compounds are found to possess higher values of dielectric properties. Dielectric properties with respect to temperature at various frequencies show stability up to certain temperature and then start increasing at high temperature as polarization is expected to rise due to increase in charge carrier with temperature.

Tellurates are found to possess good PL properties which protrude their excellect optical properties. Excitation in the ultra violet region produces emission in the visible region. PL of undoped copper tellurate is dominated by a strong / intense band. The luminescence intensity was observed to drop down drastically on cobalt doping, which could be as a result of decrease in grain sizes on doping, as in dicated from TEM images.

Photo-degradation of an organic dye i.e. methylene blue was carried out using Ni_3TeO_6 which showed complete degradation of the dye in 2 hours in presence of sunlight. Other pristine and doped copper tellurates were studied which did not give any results.

Some tellurates were also studied for partial oxidation of propylene to acrolein. Mo doped copper tellurate presented comparatively better results than the rest.

In addition to these two studies, antibacterial activity was carried out on Gram-negative *Escherichia coli* and Gram-positive *Staphylococcus aureus* using agar well diffusion method. It was observed that Ag doped Cu tellurate demonstrated excellent antimicrobial activity followed Zn and Ni doped Cu tellurate compounds.

6.2 Conclusions

A series of pristine and doped transition metals tellurates were successfully synthesized by simple eco friendly, co-precipitation and a versatile sol gel methods. X-ray powder diffraction patterns confirmed the formation of all doped and undoped tellurates. Thermal analysis revealed phase transformation from amorphous to crystalline phase and also the stability of compounds over a temperature range. Infra red spectra confirmed the purity of final compounds. The stoichiometry of the prepared samples was justified using SEM-EDS analysis. Morphology and sizes of the prepared compounds were studied by TEM-SEM, which suggested that particles hold cubic morphology with smaller particle size in doped than in pristine in the case of doped copper tellurate. UV-DRS study on all the compounds showed the band gaps in the semiconductor range. The valencies of all the elements present in doped and pristine were investigated from XPS analysis. Resistivity on all the compounds showed a typical semiconductor behavior, except for the doped copper tellurates. VSM studies showed presence of anti-ferromagnetic spins below 64 K for pristine copper tellurate. The dielectric constant with respect to frequency displayed increase in the value of dielectric permittivity at room temperature on doping. Tellurates display photoluminescence property giving blue green emission at lower excitation. Mo doped copper tellurate shows comparatively better activity for partial propylene oxidation. Ag doped copper tellurate displayed enhanced antibacterial activity.

References:

[1] S. Skiadopoulou, F. Borodavka, C. Kadlec, F. Kadlec, M. Retuerto, Z. Deng, M. Greenblatt, S. Kamba, Phys. Rev. B. 95 (2017) 1–6.

[2] M. Fiebig, J. Phys. D Appl. Phys. 38 (2005) R123–R152.

[3] S.A. Ivanov, P. Nordblad, R. Mathieu, R. Tellgren, C. Ritter, Dalt. Trans. 39 (2010) 11136–11148.

[4] W. Eerenstein, N.D. Mathur, J.F. Scott, Nat. Rev. 442 (2006) 759–765.

[5] W. Prellier, M.P. Singh, P. Murugavel, J. Phys. Condens. Matter. 17 (2005) R803–R832.

[6] T. Aoyama, K. Yamauchi, A. Iyama, S. Picozzi, K. Shimizu, T. Kimura, Nat. Commun. 5 (2014) 1–7.

[7] S.H. Chun, Y.S. Chai, Y.S. Oh, D. Jaiswal-nagar, S.Y. Haam, I. Kim, B. Lee, D.H. Nam, K. Ko, J. Park, J. Chung, K.H. Kim, Phys. Rev. Lett. 104 (2010) 1–4.

[8] N. Lee, C. Vecchini, Y.J. Choi, L.C. Chapon, A. Bombardi, P.G. Radaelli, S. Cheong, Phys. Rev. Lett. 110 (2013) 137203.

[9] Y.S. Oh, S. Artyukhin, J.J. Yang, V. Zapf, J.W. Kim, D. Vanderbilt, S. Cheong, Nat. Commun. 5 (2014) 1–7.

[10] J. Kreisel, M. Kenzelmann, Multiferroics. (2009) 17–20.

[11] C.N.R. Rao, C. Rayan, J. Mater. Chem. 17 (2007) 4931–4938.

[12] H. Schmid, J. Phys. Condens. Matter. 20 (2008) 1–24.

[13] M. Hudl, R. Mathieu, S.A. Ivanov, M. Weil, V. Carolus, T. Lottermoser, M. Fiebig, Y. Tokunaga, Y. Taguchi, Y. Tokura, P. Nordblad, Phys. Rev. B - Condens. Matter Mater. Phys. 84 (2011) 8–11.

[14] M. Lü, H. Jo, S.J. Oh, S. Lee, K.Y. Choi, Y. Yu, K.M. Ok, Inorg. Chem. 56 (2017) 5873–5879.

[15] A. La Rosa-toro, R. Berenguer, C. Quijada, F. Montilla, E. Morallo, J.L. Va, J. Phys. Chem. B. 110 (2006) 24021–24029.

[16] G.R. Li, F.L. Zheng, Y.X. Tong, Cryst. Growth Des. 8 (2008) 1226–1232.

[17] R. Kumar, O. Al-Dossary, G. Kumar, A. Umar, Nano-Micro Lett. 7 (2014) 1–24.

[18] X. Liu, S. Cheng, H. Liu, S. Hu, D. Zhang, H. Ning, Sensors. 12 (2012) 9635–9665.

[19] S.M. Kanan, O.M. El-kadri, I.A. Abu-yousef, M.C. Kanan, Sensors. 9 (2009) 8158–8196.

[20] P. Ivanov, E. Llobet, X. Vilanova, J. Brezmes, J. Hubalek, X. Correig, Sensors Actuators B. 99 (2004) 201–206.

[21] Q. Qi, T. Zhang, S. Wang, X. Zheng, Sensors Actuators B. 137 (2009) 649–655.

[22] Y. Xie, Y. He, P.L. Irwin, T. Jin, X. Shi, Appl. Environ. Microbiol. 77 (2011) 2325–2331.

[23] M.D.S. Hackenberg, M.D.A. Scherzed, A. Technau, M.D.K. Froelich, M.D.R. Hagen, M.D.N. Kleinsasser, J. Biomed. Nanotechnol. 9 (2013) 86–95.

[24] U. Hoppe, E. Yousef, C. Rüssel, J. Neuefeind, A.C. Hannon, J. Phys. Condens. Matter. 16 (2004) 1645–1663.

[25] L. Xu, C. Qin, H. Xie, Y. Huang, L. Qin, H.J. Seo, Mater. Lett. 184 (2016) 1–4.

[26] I. Živković, K. Prša, O. Zaharko, H. Berger, J. Phys. Condens. Matter. 22 (2010) 056002.

[27] B. Zare, M. Nami, A. Shahverdi, J. Pathol Bacteriol. 35 (1932) 831–842.

[28] L.A. Ba, M. Döring, V. Jamier, C. Jacob, Org. Biomol. Chem. 8 (2010) 4203–4216.

[29] C. Graf, A. Assoud, O. Mayasree, H. Kleinke, Molecules. 14 (2009) 3115–3131.

[30] M. Herak, H. Berger, M. Prester, M. Miljak, I. Živković, O. Milat, D. Drobac, S. Popović, O. Zaharko, J. Phys. Condens. Matter. 17 (2005) 7667–7679.

[31] R. Sankar, G.J. Shu, B. Karunakara Moorthy, R. Jayavel, F.C. Chou, Dalt. Trans. 42 (2013) 10439–10443.

[32] A. Dasadia, Crystal growth and characterizations of multiferroic, 2014.

[33] A. Dias, G. Subodh, M.T. Sebastian, M.M. Lage, R.L. Moreira, Chem. Mater. 20 (2008) 4347–4355.

[34] G.M. Kaleva, E.D. Politova, S.A. Ivanov, A. V. Mosunov, S.Y. Stefanovich, N. V. Sadovskaya, R. Mathieu, P. Nordblad, Inorg. Mater. 47 (2011) 1132–1140.

[35] X. Su, A. Wu, P.M. Vilarinho, Scr. Mater. 67 (2012) 927–930.

[36] X. Zhu, Z. Wang, X. Su, P.M. Vilarinho, ACS Appl. Mater. Interfaces. 6 (2014) 11326–11332.

[37] M. Udovic, M. Valant, D. Suvorov, J. Eur. Ceram. Soc. 24 (2004) 953–958.

[38] N. V Golubko, V.Y. Proidakova, G.M. Kaleva, S.A. Ivanov, A. V Mosunov, S.Y. Stefanovich, N. V Sadovskaya, E.D. Politova, P. Nordblad, Bull. Russ. Acad. Sci. Phys. 74 (2010) 724–726.

[39] M. a. Evstigneeva, V.B. Nalbandyan, A. a. Petrenko, B.S. Medvedev, A. a. Kataev, Chem. Mater. 23 (2011) 1174–1181.

[40] S.W. Kim, Z. Deng, M.R. Li, A. Sen Gupta, H. Akamatsu, V. Gopalan, M. Greenblatt, Inorg. Chem. 55 (2016) 1333–1338.

[41] H. Singh, H. Ghosh, T. V. Chandrasekhar Rao, A.K. Sinha, P. Rajput, J. Appl. Phys. 116 (2014).

[42] H. Singh, A.K. Sinha, H. Ghosh, M.N. Singh, P. Rajput, C.L. Prajapat, M.R. Singh, G. Ravikumar, J. Appl. Phys. 116 (2014) 074904.

[43] H. Singh, A.K. Sinha, S.M. Gupta, M.N. Singh, H. Ghosh, Condens. Matter Mater. Sci. 6 (2015) 1–14.

[44] B. Wedel, I. Kimio, K. Sugiyama, Zeitschrift Fur Krist. - New Cryst. Struct. 216 (2001) 345–346.

[45] G. Caimi, L. Degiorgi, H. Berger, Europhys. Lett. 75 (2006) 496–502.

[46] Z. He, M. Itoh, J. Magn. Magn. Mater. 354 (2014) 146–150.

[47] S.A. Ivanov, R. Mathieu, P. Nordblad, C. Ritter, R. Tellgren, N. Golubko, A. Mosunov, E.D. Politova, M. Weil, Mater. Res. Bull. 50 (2014) 42–56.

[48] K.Y. Choi, P. Lemmens, E.S. Choi, H. Berger, J. Phys. Condens. Matter. 20 (2008) 505214.

[49] M. Månsson, K. Prša, J. Sugiyama, D. Andreica, H. Luetkens, H. Berger, Phys. Procedia. 30 (2012) 142–145.

[50] N. Petragnani, Tretrahedron. 61 (2005) 1613–1679.

[51] H. Li, C. Ren, S. Xu, L. Wang, Q. Yue, R. Li, Y. Zhang, Q. Xue, J. Liu, J. Mater. Chem. A. 3 (2015) 5850–5858.

[52] C.H. Fisher, A. Eisner, J. Org. Chem. 6 (1941) 169–174.

[53] Y. Shyr, G. Price, Ind. Eng. Chem. Prod. Res. Dev. 23 (1984) 536–541.

[54] C.L. Zhong, B.Y. Qin, X.Y. Xie, Y. Bai, J. Nano Res. 25 (2013) 8–15.

[55] Y. Chen, W.H. Tse, L. Chen, J. Zhang, Nanoscale Res. Lett. 10:106 (2015) 1–8.

[56] K.T. Rustembekov, A.T. Dyusekeeva, Russ. J. Gen. Chem. 82 (2012) 1357–1360.

[57] N. Dewan, K. Sreenivas, V.G. Ã, J. Cryst. Growth. 305 (2007) 237–241.

[58] M. Pal, Y. Tsujigami, A. Yoshikado, H. Sakata, Phys. Stat. Sol. 727 (2012) 727–736.

[59] J. Xu, A. Assoud, N. Soheilnia, S. Derakhshan, H.L. Cuthbert, J.E. Greedan, M.H. Whangbo, H. Kleinke, V. Uni, C. Ls, N. Carolina, S.U. V, N. Carolina, Inorg. Chem. 44 (2005) 291–295.

[60] L. Viciu, Q. Huang, E. Morosan, H.W. Zandbergen, N.I. Greenbaum, J. Solid State Chem. 180 (2007) 1060–1067.

[61] J. Kim, J. Baek, P.S. Halasyamani, Chem. Mater. 5637 (2007) 5637–5641.

[62] I. Alvarez, M.L. Veiga, C. Pico, J. Mater. Chem. 5 (1995) 1049–1051.

[63] M.S. Augsburger, M.C. Viola, J.C. Pedregosa, A. Mun, J.A. Alonso, R.E. Carbonio, J. Mater. Chem. 15 (2005) 993–1001.

[64] L.O. Martın, J.P. Chapman, Z. Anorg. Allg. Chem. 631 (2005) 2127–2130.

[65] D. Iwanaga, Y. Inaguma, M. Itoh, J. Solid State Chem. 295 (1999) 291–295.

[66] M.P.O. Callaghan, A.S. Powell, J.J. Titman, G.Z. Chen, E.J. Cussen, Chem. Mater. 15 (2008) 2360–2369.

[67] Y. Laligant, J. Solid State Chem. 408 (2001) 401–408.

[68] D. Hamani, M. Colas, O. Masson, M. Smirnov, P. Thomas, J. Solid State Chem. 184 (2011) 637–643.

[69] J. Yeon, S. Kim, M.A. Hayward, P.S. Halasyamani, Inorg. Chem. 7 (2011) 8663–8670.

[70] Y.J. Shan, K. Sasaki, K. Sudo, Jpn.J.Appl.Phys. 41 (2002) 4–7.

[71] W. Luan, Y. Jin, M. Itoh, H. Imoto, Ceram. Int. 31 (2005) 129–133.

[72] M. Udovic, M. Valant, D. Suvorov, Key Eng. Mater. 206–213 (2002) 1409–1412.

[73] M. Udovic, M. Valant, D. Suvorov, J. Eur. Ceram. Soc. 21 (2001) 1735–1738.

[74] N.N. Greenwood, A. Earnshaw, Chemistry of the Elements, second, Elsevier, 2002.

[75] J.M. Sandoval, P. Leve, Biometals. 23 (2010) 623–32.

[76] G. Bayer, J. Less-Common Met. 16 (1968) 215–222.

[77] W.A. Dutton, W.C. Cooper, W.C. Cooper, Chem. Rev. 66 (1966) 657–675.

[78] K. Tezuka, S. Kawakami, Y.J. Shan, H. Imoto, J. Ceram. Soc. Japan. 116 (2008) 610–613.

[79] Y.J. Shan, Y. Yoshioka, M. Wakeshima, K. Tezuka, H. Imoto, J. Solid State Chem. 211 (2014) 63–68.

[80] J.D. Jorgenson, Selenium and tellurium, U.S. Geological survey minerals, 2002.

[81] K. Jung, H. Kim, H. Yun, J. Do, Z. Anorg. Allg. Chem. 632 (2006) 1582–1585.

[82] R.M. Mohamed, Mater. Sci. Eng. B. 98 (2003) 193–203.

[83] H. Jiang, J. Mao, Z. Anorg. Allg. Chem. 632 (2006) 2053–2057.

[84] F.. Mathers, G.. Bradbury, J. Am. Chem. Soc. 51 (1929) 3229–3232.

[85] G. Bayer, Zeitschrift Für Krist. 135 (1967) 131–135.

[86] Y. Dimitriev, E. Gatev, Y. Ivanova, J. Mater. Sci. Lett. 8 (1989) 230–231.

[87] I. Kagomiya, Y. Kodama, Y. Shimizu, K.I. Kakimoto, H. Ohsato, Y. Miyauchi, J. Alloys Compd. 640 (2015) 383–387.

[88] C. Neamţu, A. Darabont, E. Surducan, J. Optoelectron. Adv. Mater. 2 (2000) 487–492.

[89] M. Udovic, M. Valant, D. Suvorov, J. Eur. Ceram. Soc. 21 (2001) 1735–1738.

[90] M. Udovic, M. Valant, D. Suvorov, J. Am. Ceram. Soc. 97 (2004) 591–597.

[91] D.-K. Kwon, M.T. Lanagan, T.R. Shrout, J. Am. Ceram. Soc. 88 (2005) 3419–3422.

[92] X. Zhu, Z. Wang, X. Su, P.M. Vilarinho, ACS Appl. Mater. Interfaces. 6 (2014) 11326–11332.

[93] E.. Lambson, G.. Saunders, J. Non. Cryst. Solids. 69 (1984) 117–133.

[94] K. Aida, Y. Benino, V. Dimitrov, T. Komatsu, J. Am. Ceram. Soc. 83 (2000) 1192–1198.

[95] S.J. Perm, N.M. Alford, A. Templeton, X. Wang, M. Xu, M. Reece, K. Schrapelt, J. Am. Ceram. Soc. 80 (1997) 4–7.

[96] F. James, E.J.F. Shackelford, W. Alexander, Materials Science Engineering, CRC Press LLC, 2001.

[97] I. Kagomiya, Y. Matsuda, K. Kakimoto, H. Ohsato, Ferroelectrics. 387 (2009) 1–6.

[98] Y. Miyauchi, Y. Ohishi, S. Miyake, H. Ohsato, J. Eur. Ceram. Soc. 26 (2006) 2093–2096.

[99] Y. Miyauchi, I. Kagomiya, Y. Ohishi, Ferroelectrics. 387 (2009) 46–53.

[100] G. Blasse, R. June, J. Solid State Chem. 27 (1979) 303–305.

[101] P. Pal, S.R. Mohapatra, S.D. Kaushik, A.K. Singh, AIP Conf. Proc. 1832 (2016) 140026.

[102] S. Mu, K.D. Belashchenko, J. Phys. Condens. Matter. 27 (2015) 22203.

[103] J. Wang, J.A.C. Santana, N. Wu, C. Karunakaran, J. Wang, P.A. Dowben, C. Binek, J. Phys. Condens. Matter. 26 (2014) 055012.

[104] H. Singh, A.K. Yadav, AIP Conf. Proc. 1731 (2016) 060019.

[105] K. Krishnan, K.D.S. Mudher, G.A.R. Rao, V. Venugopal, J. Alloys Compd. 316 (2001) 264–268.

[106] G. Behera, Structural , Magnetic and Dielectric Investigation of Iron Tellurate Fe 2 TeO 6, National Institute of Technology Rourkela, 2016.

[107] P. Pal, M.F. Abdullah, S.R. Mohapatra, S.D. Kaushik, A.K. Singh, AIP Conf. Proc. 1942 (2018) 130039.

[108] S.D. Kaushik, B. Sahu, S.R. Mohapatra, A.K. Singh, AIP Conf. Proc. 1731 (2016) 1–4.

[109] F.J. Berry, C.D. Gibbs, Hyperfine Interact. 67 (1991) 513–516.

[110] K.D.S. Mudher, K. Krishnan, I.K. Gopalakrishnan, D.C. Kundaliya, S.K. Malik, ChemInform. 36 (2005) 1–16.

[111] W. Kunnmann, S. La Placa, L.M. Corliss, J.M. Hastings, E. Banks, J. Phys. Chem. Solids. 29 (1968) 1359–1364.

[112] S. Buksphan, Solid State Commun. 10 (1972) 657–662.

[113] T. Birchall, J. Solid State Chem. 27 (1979) 293–298.

[114] F.J. Berry, T. Birchall, C.D. Gibbs, C. Frampton, C. Hallett, Hyperfine Interact. 41 (1988) 459–462.

[115] M. Sahu, D. Rawat, B.G. Vats, M.K. Saxena, S. Dash, Thermochim. Acta. 585 (2014) 50–62.

[116] R. Dawar, A. Jain, R. Babu, K. Ananthasivan, S. Anthonysamy, J. Therm. Anal. Calorim. 122 (2015) 885–891.

[117] M. Yamaguchi, M. Ishikawa, J. Phys. Soc. Japan. 63 (1994) 1666–1669.

[118] R. Mathieu, S.A. Ivanov, P. Nordblad, M. Weil, Eur. Phys. J. B. 86 (2013) 3–6.

[119] M.A. Basu, R. Mishra, A.S. Kerkar, S.R. Bharadwaj, D. Das, J. Nucl. Mater. 301 (2002) 183–186.

[120] R.E. Newnham, E.P. Meagher, Mater. Res. Bull. 2 (1967) 549–554.

[121] K. Krishnan, G.A.R. Rao, K.D.S. Mudher, V. Venugopal, J. Alloys Compd. 288 (1999) 96–101.

[122] C. Mallika, O.M. Sreedharan, Thermochim. Acta. 190 (1991) 217–224.

[123] W. Hordijk, J. Solid State Chem. 5 (1972) 395–397.

[124] L. Zhao, C. Du, A.C. Komarek, Phys. Status Solidi RRL 11,. 1700073 (2017) 4–8.

[125] J. Zupan, D. Kolar, V. Urbanc, Mat. Res. Bull. 6 (1971) 1353–1359.

[126] S.A. Ivanov, P. Nordblad, R. Mathieu, R. Tellgren, C. Ritter, N. V Golubko, E.D. Politova, M. Weil, Mater. Res. Bull. 46 (2011) 1–16.

[127] R. Becker, H. Berger, Acta Crystallogr. Sect. E. 62 (2006) 222–223.

[128] M.O. Yokosuk, S. Artyukhin, X. Wang, J. Yang, Z. Li, S. Cheong, D. Vanderbilt, J.L. Musfeldt, Phys. Rev. B. B 92 (2015) 144305.

[129] X. Wang, F. Huang, J. Yang, Y.S. Oh, S. Cheong, APL Mater. 3 (2015) 076105.

[130] Y.S. Oh, S. Artyukhin, J.J. Yang, V. Zapf, J.W. Kim, D. Vanderbilt, S. Cheong, Nat. Commun. 5 (2014) 1–7.

[131] M. Udovic, D. Suvorov, J. Am. Ceram. Soc. 2408 (2007) 2404–2408.

[132] M. Herak, H. Berger, M. Prester, M. Miljak, I. Zivkovic, O. Milat, D. Drobac, S. Popovic, O. Zaharko, J.Phys.:Condens.Matter. 17 (2005) 7667–7679.

[133] M. Herak, Solid State Commun. 151 (2011) 1588–1592.

[134] B.Y.L. Falck, O. Lindqvist, L.D.C.M. C, P.E. Bataillon, Acta Cryst. B34 (1978) 896–897.

[135] M.A. Hassan, C.A. Hogarth, J. Mater. Sci. 23 (1988) 2500–2504.

[136] N. V Golubko, V.Y. Proidakova, G.M. Kaleva, S.A. Ivanov, A. V Mosunov, S.Y. Stefanovich, N. V Sadovskaya, E.D. Politova, P. Nordblad, Bull. Russ. Acad. Sci. Phys. 74 (2010) 724–726.

[137] H. Singh, H. Ghosh, T.V.C. Rao, A.K. Sinha, Condens. Matter Mater. Sci. (2014) 21.

[138] C.W. Wang, C.H. Lee, C.Y. Li, C.M. Wu, W.H. Li, C.C. Chou, H.D. Yang, J.W. Lynn, Q. Huang, A.B. Harris, H. Berger, Phys. Rev. B. 88 (2013) 184427.

[139] H.T. Sun, Y. Sakka, J. Mater. Chem. 4 (2012) 24792–24797.

[140] R.L.O.R. Cunha, I.E. Gouvea, L. Juliano, An. Acad. Bras. Cienc. 81 (2009) 393–407.

[141] D.E. Taylor, Trends Microbiol. 7 (1999) 111–115.

[142] Z. Lin, C. Lee, H. Chang, H. Chang, Chem. Asian J. 7 (2012) 930–934.

[143] D. Zannoni, F. Borsetti, J.J. Harrison, R.J. Turner, D. Zannoni, E.T. Al, Adv. Microb. Physiol. 53 (2008) 1–72.

[144] A.D. Frazer, M.B. Edin, Lancet. 216 (1930) 133–134.

[145] A. Flemming, M.Y. Young, Bac Coli. 4 (1940) 29.

[146] A. Fleming, FRCS, J. Pathol. Bacteriol. 35 (1932) 831–842.

[147] B. Zare, M. Nami, A.R. Shahverdi, Biol. Trace Elem. Res. 180 (2017) 171–181.

[148] A. Summers, G.A. Jacoby, J. Bacteriol. 129 (1977) 276–281.

[149] B.K. Kinkle, M.J. Sadowsky, K. Johnstone, W.C. Koskinen, Appl. Environ. Microbiol. 60 (1994) 1674–1677.

[150] R.C. Molina-quiroz, C.M. Munoz-villagran, PLoS One. 7 (2012) e35452.

[151] S.D. Mardolkar, A. V. Salker, New J. Chem. 41 (2017) 13974–13982.

[152] M.D. Daivajna, A. Rao, G.S. Okram, J. Magn. Magn. Mater. 388 (2015) 90–95.

[153] G. Ding, G. Gao, K. Yao, Sci. Rep. 5 (2015).

[154] S. Roychowdhury, U.S. Shenoy, U. V. Waghmare, K. Biswas, J. Mater. Chem. C. 5 (2017) 5737–5748.

[155] M.G. Patil, V.C. Mahajan, B. V. Bhise, A.K. Ghatage, S.D. Lotke, S.A. Patil, Bull. Mater. Sci. 17 (1994) 399–403.

[156] D. Ravinder, G. Ravi Kumar, Y.C. Venudhar, J. Alloys Compd. 363 (2004) 6–9.

[157] S.N. Mustafaeva, M.M. Asadov, A.I. Jabbarov, E.M. Kerimova, Inorg. Mater. 51 (2015) 220–224.

[158] D.O. Northwood, X.C. Sun, J. Hochreiter, J.H. Sokolowski, D.E. Penrod, AIP Conf. Proc. 316 (1994) 180–183.

[159] P. Sathya, S. Radhakrishna, J. Mater. Sci. 23 (1988) 4492–4502.

[160] A.I. Eatah, Phys. Stat. Sol. 104 (1987) 793–797.

[161] A.M. Badr, H.A. Elshaikh, I.M. Ashraf, J. Mod. Phys. 02 (2011) 12–25.

[162] A.C. Roberts, T.S. Ercit, R.S. Williams, M.C. Jensen, Mineral. Mag. 58 (1994) 417–424.

[163] S.K. Ahmmad, M.A. Samee, S.M. Taqiullah, S. Rahman, J. Taibah Univ. Sci. 10 (2016) 329–339.

[164] S.J. Naik, A. V. Salker, Solid State Sci. 12 (2010) 2065–2072.

[165] E. Drexler, Engines of Creation: The coming Era of Nanotechnology, Anchor Books, Doubleday, 1986.

[166] R.K. Gupta, Z. Serbetc, F. Yakuphanoglu, J. Alloys Compd. 515 (2012) 96–100.

[167] F. Bayansal, Metall. Mater. Trans. A. 45A (2014) 3670–3674.

[168] B.B. Straumal, S.G. Protasova, A.A. Mazilkin, E. Goering, G. Schütz, P.B. Straumal, B. Baretzky, Beilstein J. Nanotechnol. 7 (2016) 1936–1947.

[169] B. Straumal, A. Mazilkin, P. Straumal, Rev. Adv. Mater. Sci. 41 (2015) 61–71.

[170] S. Rahimnejad, J.H. He, W. Chen, K. Wu, G.Q. Xu, RSC Adv. 4 (2014) 62423–62429.

[171] S.R. Naik, A. V. Salker, S.M. Yusuf, S.S. Meena, J. Alloys Compd. 566 (2013) 54–61.

[172] W.E. Sartz, K.J. Wynne, D.M. Hercules, Anal. Chem. 43 (1971) 1884–1887.

[173] M.K. Bahl, R.L. Watson, K.J. Irgolic, J. Chem. Phys. 66 (1977) 5526–5535.

[174] A. Pronschinske, P. Pedevilla, B. Coughlin, C.J. Murphy, F.R. Lucci, M.A. Payne, A.J. Gellman, A. Michaelides, E.C.H. Sykes, ACS Nano. 10 (2016) 2152–2158.

[175] A.C. Catto, L.F.D. Silva, M.I.B. Bernardi, S. Bernardini, K. Aguir, E. Longo, V.R. Mastelaro, ACS Appl. Mater. Interfaces. 8 (2016) 26066–26072.

[176] S. Wang, P. Li, H. Liu, J. Li, Y. Wei, J. Alloys Compd. 505 (2010) 362–366.

[177] N. Weidler, J. Schuch, F. Knaus, P. Stenner, S. Hoch, A. Maljusch, R. Scha, B. Kaiser, W. Jaegermann, J. Phys. Chem. C. 121 (2017) 6455–6463.

[178] R.S. Ganesh, E. Durgadevi, M. Navaneethan, V.L. Patil, S. Ponnusamy, C. Muthamizhchelvan, S. Kawasaki, P.S. Patil, Y. Hayakawa, Chem. Phys. Lett. 689 (2017) 92–99.

[179] V. Castro, G. Polzonetti, J. Electron Spectros. Relat. Phenomena. 48 (1989) 117–123.

[180] W. Wang, H. Wang, Y. Yu, Z. Wu, M. Asif, H. Liu, Catal. Sci. Technol. 8 (2018) 480–485.

[181] J. Wang, J. Wang, H. Liu, H. Liu, Z. Fu, D. Nan, Chem. Eng. J. 328 (2017) 591–598.

[182] H. Nesbitt, D. Banerjee, Am. Mineral. 83 (1998) 305–315.

[183] Z. Huang, W. Zhou, C. Ouyang, J. Wu, F. Zhang, J. Huang, Nat. Publ. Gr. 5 (2015) 1–9.

[184] N. Gogurla, A.K. Sinha, S. Santra, S. Manna, S.K. Ray, Sci. Rep. 4 (2014) 6483(1-9).

[185] D. Correa, J.C.O. Pazinato, L.S. Dorneles, C. Radtke, I.T.S. Garcia, J. Brazilian Chem. Soc. 25 (2014) 822–830.

[186] M. Lv, W. Xie, Catal. Sci. Technol. 5 (2015) 2925–2934.

[187] P. Tao, Y. Xu, Y. Zhou, C. Song, Y. Qiu, W. Dong, M. Zhang, M. Shao, Mater. Res. 20 (2017) 786–790.

[188] Y. Zheng, C. Chen, Y. Zhan, X. Lin, Q. Zheng, K. Wei, J. Zhu, J. Phys. Chem. C. 112 (2008) 10773–10777.

[189] M. Hossein, H. Reza, J Sol-Gel Sci Technol. 54 (2010) 195–202.

[190] T. Yamashita, P. Hayes, Appl. Surf. Sci. 254 (2008) 2441–2449.

[191] V.K. Mittal, P. Chandramohan, S. Bera, M.P. Srinivasan, S. Velmurugan, S. V Narasimhan, Solid State Commun. 137 (2006) 6–10.

[192] J. Gan, X. Lu, J. Wu, S. Xie, T. Zhai, M. Yu, Z. Zhang, Y. Mao, S. Chi, I. Wang, Y. Shen, Y. Tong, Sci. Rep. 3 (2013) 1–7.

[193] J. Feng, D. Fan, Q. Wang, L. Ma, W. Wei, J. Xie, J. Zhu, Colloids Surfaces A Physicochem. Eng. Asp. 520 (2017) 743–756.

[194] M. Nesa, M. Sharmin, K.S. Hossain, J. Mater. Sci. Mater. Electron. 28 (2017) 12523–12534.

[195] A. Sundaresan, R. Bhargavi, N. Rangarajan, U. Siddesh, C.N.R. Rao, Phys. Rev. B. 74 (2006) 161306(1-4).

[196] P. Thakur, A. Kool, B. Bagchi, N.A. Hoque, S. Das, P. Nandy, RSC Adv. 5 (2015) 28487–28496.

[197] S. El-SAyed, T.A. Abdel-baset, A. Hassen, AIP Adv. 3 (2017) 037114.

[198] B.P. Mandal, P. Anithakumari, S. Nigam, C. Majumder, M. Mohapatra, A.K. Tyagi, New J. Chem. 40 (2016) 9526–9536.

[199] A.K. Singh, T.C. Goel, R.G. Mendiratta, O.P. Thakur, C. Prakash, J. Appl. Phys. 91 (2002) 6626–6629.

[200] M. George, S.S. Nair, A.M. John, P.A. Joy, M.R. Anantharaman, J. Phys. D. Appl. Phys. 39 (2006) 900–910.

[201] K.N. Shinde, S.J. Dhoble, H.C. Swart, K. Park, Phosphate Phosphors for Solid-State Lighting, Springer, 2013.

[202] D. Beydoun, R. Amal, G. Low, S. Mcevoy, J. Nanoparticle Res. 1 (1999) 439–458.

[203] B. Khoshnevisan, M. Bagher, Chinese Phys. Lett. 35 (2018) 27501.

[204] G. Longo, A. Pertegás, L. Martínez-Sarti, M. Sessolo, H.J. Bolink, J. Mater. Chem. C. 3 (2015) 11286–11289.

[205] N.G. Heatley, Biochem. J. 38 (1943) 61–65.

APPENDIX I

Publications:

- **S. D. Mardolkar** and **A.V. Salker**, *New Journal of Chemistry*, **41** (2017) 13974.

"Efficiently synthesized Co doped Cu_3TeO_6 accounted for its anomalous behaviour in electronic properties".

- **S. D. Mardolkar and A.V. Salker**

  "Effect of Co doping on the opto-electronic properties of doped copper tellurate".

  (Communicated)

- **S. D. Mardolkar and A.V. Salker**

  "Magnetic, electrical and optical properties exhibited by Nickel doped copper tellurates".

  (Communicated)

APPENDIX II

Presentations at Conference/Symposium:

- ✓ "International Conference on Green Chemistry: Catalysis, Energy and Environment", (ICGC-2015), Department of Chemistry, Goa University, Goa, January 22-24, 2015.

- ✓ **S. D. Mardolkar, A. V. Salker**
  "Synthesis, characterization and solid state studies on Te-containing compounds", MCM-16, Goa University, August 18, 2016.

- ✓ **S. D. Mardolkar, A. V. Salker**
  "Preparation and solid state properties of metal Tellurates".
  RSC (UK) West India Chapter Symposium on Recent Advancements in chemical sciences and research scholars meet – 2016, BITS Pilani Goa, November 13 2016.

- ✓ **S. D. Mardolkar & A.V.Salker**
  " Synthesis, thermal and electrical properties of metal tellurite".
  THERMANS – 2018, Goa University, January 18-20, 2018.

- ✓ **S. D. Mardolkar & A.V.Salker**
  "Studies and distinction in the properties of copper tellurate on cobalt substitution". Frontiers in chemical sciences (FICS – 2018), IIT Guwahati, Guwahati Assam, December 06-08, 2018.